MULTI-SCALE SIMULATION OF SURFACE SEGREGATION AND OXYGEN REDUCTION REACTION ON PLATINUM ALLOY SURFACE: DENSITY FUNCTIONAL THEORY, MONTE CARLO SIMULATION, AND KINETIC ANALYSIS

by

Zhiyao Duan

Submitted to the Graduate Faculty of

the Swanson School of Engineering in partial fulfillment

of the requirements for the degree of

Doctor of Philosophy

University of Pittsburgh

2013

UNIVERSITY OF PITTSBURGH

SWANSON SCHOOL OF ENGINEERING

This dissertation was presented

by

Zhiyao Duan

It was defended on

May 1 2013

and approved by

Guofeng Wang, Ph.D., Assistant Professor, Department of Mechanical Engineering and Materials Science

John A. Barnard, Ph.D., Professor, Department of Mechanical Engineering and Materials Science

Brian Gleeson, Ph.D., Harry S. Tack Chair in Materials Science, Department of Mechanical Engineering and Materials Science

Albert To, Ph.D., Assistant Professor, Department of Mechanical Engineering and Materials Science

Lei Li, Ph.D., Assistant Professor, Department of Chemical and Petroleum Engineering

Dissertation Director: **Guofeng Wang**, Ph.D., Assistant Professor, Department of Mechanical Engineering and Materials Science

MULTI-SCALE SIMULATION OF SURFACE SEGREGATION AND OXYGEN REDUCTION REACTION ON PLATINUM ALLOY SURFACE: DENSITY FUNCTIONAL THEORY, MONTE CARLO SIMULATION, AND KINETIC ANALYSIS

Zhiyao Duan, PhD

University of Pittsburgh, 2013

Proton-exchange membrane fuel cell (PEMFC) is an electrochemical device for directly converting chemical energy stored in hydrogen fuel to electricity at low temperature. In order to improve the efficiency and reduce the cost of PEMFC, numerous research efforts have been devoted to developing cheaper yet more efficient electrocatalysts by alloying Pt with 3d transition metals. A number of Pt-based alloys were identified to have better activity for catalyzing ORR than pure Pt catalysts. Although Pt-based catalysts have better ORR activity, the underlying reasons for the improvement are unclear and controversial. Atomistic simulation can provide molecular-level information of physical and chemical processes in materials. In my research works, the state-of-art simulation methods were employed to elucidate the surface structures of Pt-based alloys, reaction mechanism of ORR on Pt and Pt-based surfaces, and degradation of Pt and Pt-based nanoparticle catalysts. Based on the research topics, my research is primarily composed of four parts as followed.

Firstly, surface segregation phenomena in Pt_3Ti, Pt-Pd, and Pt_3Fe alloys were investigated with density functional theory (DFT) and Monte Carlo (MC) simulations. Through the computational study, the driving forces and mechanisms of surface segregation were clarified, and the surface composition profiles were quantitatively predicted. For example, the DFT simulation suggested that off-stoichiometric effect accounted for the experimentally observed Pt segregation to the outermost layer of the Pt_3Ti (111). Our MC simulations

predicted in a Pt_3Ti (111) sample with a Pt concentration slightly above 75 at. %, Pt atoms would segregate to the surface to form a pure Pt outermost layer, while the ordered Pt_3Ti crystal structure would be maintained in the second layer and below. The knowledge of surface structures of Pt-based alloys was acquired through the surface segregation study, which set the ground for further studies on catalytic properties of the surfaces of the alloys.

Secondly, first-principles DFT calculations was employed to elucidate the reaction mechanism of ORR on Pt and Pt/M (111) and (100) surfaces (M=Ni, Co, Fe). The binding strengths of chemical intermediates involved in ORR are less strongly on Pt/M surfaces compared to the pure Pt couterparts due to the modified electronic structure of the Pt overlayer by the subsurface transition metals. ORR mechanism is also shifted on modified Pt overlayers. It was found that ORR proceeds through OOH dissociation mechanism on Pt (111) surface, while on Pt/M (111) surfaces ORR proceeds through HOOH dissociation mechanism. The significance of the changed ORR mechanism is that ORR activity measured by the barrier of rate-determining step is greatly enhanced on Pt/M (111) surfaces. For example, on Pt/Ni (111) surface, O_2 hydrogenation is the rate-determining step with a barrier of 0.15 eV compared to O hydrogenation with 0.79 eV on Pt (111) surface. We also determined ORR mechanism on Pt (100) and Pt/Ni (100) surface to be O_2 dissociation mechanism. There is no mechanism change between Pt (100) and Pt/Ni (100) surfaces since the subsurface Ni has much less effect on (100) surface than that on (111) surface. The results from our calculations give an explanation of experimentally observed enhancement of ORR activity on Pt/M (111) surface and relative ORR activity between Pt (111) and Pt (100) surfaces.

In the third part, kinetic Monte Carlo (KMC) algorithm is implemented to study the kinetics of ORR based on the mechanistic information obtained in the second study. The information of the elementary reactions involved in ORR such as the adsorption sites of the reactants and products, activation energies, etc. is input into the KMC code. The KMC simulation can simulate the dynamics of ORR and output the current density (joules/cm^2/s) generated from the reactions. Then, the simulated current density which is a measure of ORR activity can be directly compared to experimental measurement. In the study, kinetics of ORR on Pt (111) and Pt (100) surfaces were simulated. The simulated current density

of ORR on Pt (111) and Pt (100) at electrode potential 0.8 V is in the same magnitude with experimental measurement, although the actual value is about 2 times lower. The reasonable agreement with experiments also in turn indicates that the previous mechanistic study is reliable.

Expect for the activity issue, Pt nanoparticle catalyst also faces degradation problem due to the highly oxidizing environment in the cathode of PEMFC. In the final part, the degradation of Pt nanoparticle catalyst through Pt dissolution is studied employing grand-canonical Monte Carlo (GCMC) simulation. Pt dissolution process was found to be initialized through the dissolution of under-coordinated Pt atoms sitting on the corners and edges of the nanoparticle. After the initial dissolution of Pt atoms on corners and edges, more under-coordinated Pt atoms are generated and the dissolution process is accelerating. The smaller Pt nanoparticle is more vulnerable to the Pt dissolution process than the larger nanoparticle. A Pt nanoparticle with about 5 nm diameter is stable in the environment. It was also found that Au atoms segregated to the under-coordinated sites would stabilize the nanoparticle because Au atoms will not dissolute and the dissolution process will not be initialized. The simulation explains the stabilizing effect of Au observed in the experiments.

Keywords: PEM fuel cell, oxygen reduction reaction, surface segregation, MEAM, Monte Carlo simulation, kinetic Monte Carlo simulation, density functional theory, transition state calculation, reaction mechanism, electrochemical degradation, platinum, platinum-based alloy.

TABLE OF CONTENTS

LIST OF TABLES

LIST OF FIGURES

ACKNOWLEDGMENTS

I am grateful to all the people that helped me during my study, without their support this work would not have been possible. I am extremely grateful to my doctoral advior, Professor Guofeng Wang, who has been a constant support, guider and friend. He made it possible for me to attend the graduate school here in the University of Pittsburgh and opened the door for me to the research career that I am passionated about. I will never repay him for what he has been done for me.

I am grateful to my doctoral committee, Dr. John Barnard, Dr. Brian Gleeson, Dr. Albert To, and Dr. Lei Li, for their advisement in this work and their kind endurance of my terrible presentation.

I owe much appreciation to my friends and colleagues in the research group of Professor Guofeng Wang, especially Chan Xiao, Yinkai Lei, Dr. Shyam Kattal, Kexi Liu, Zhenyu Liu, and Corinne Gray, for their help in this work and the joy times we spent together.

I am grateful to my parents, Mr. Shiyun Duan and Mrs. Hua Su, for giving me the most generous and selfless love to me.

I reserve a special thanks for my lovely wife, Mrs. Rongrong Zeng. She has been an ever-constant love, support, comforter, and closest friend and ally.

This research was funded by Chemical Sciences Research Programs, Office of Basic Energy Sciences, U.S. Department of Energy (Grant no. DE-FG02-09ER16093). The computations were performed on the computer facility at Center for Simulation and Modeling of the University of Pittsburgh.

1.0 INTRODUCTION

1.1 BACKGROUND

Nowadays, the major energy resources utilized by human such as petroleum and coal are non-renewable. The ever increased demand on the energy due to developing economy and exploding population have already made a energy crisis emerged. The Energy Information Administration (U. S. Department of Energy (DOE)) projects the world marketed-energy consumption to increase by 53 percent from 2008 to 2035.[1] Moreover, the burning of fossil fuels produce emissions which are responsible for air pollution. The world carbon dioxide emissions are projected to continue increasing from 30.2 billion metric tons in 2008 to 35.2 billion metric tons in 2020 and 43.2 billion metric tons in 2035. This represents an increase of 43 percent over 2008-2035.[1] In order to turn the trend, the development of clean and renewable energy is required. Hydrogen is a promising candidate since it can be obtained renewably by splitting water using wind or solar energy and the burning of it only produces water. In order to utilize hydrogen fuel, conversion devices such like fuel cells are needed. Particularly, fuel cells for hydrogen-powered automotive attracts a lot of people's attention due to the fact that of all the end uses of oil in the U.S. roughly 70% is used for transportation. At present, the fuel cell technology most prominently being developed for automobiles is called the Polymer Electrolyte Membrane fuel cell (PEMFC).

1.2 INTRODUCTION TO PEMFC

Fuel cells are galvanic cells in which the Gibbs free energy of a chemical reaction is converted into work via an electrical current. Specifically for PEMFCs, hydrogen atoms dissociate into protons (H^+) and electrons (e^-) at the anode. The electrons pass through an external circuit/load producing electricity while the H^+ ions move across the proton-conducting membrane. On reaching the cathode, these electrons and protons react with the supplied oxygen to form water, which is the product of the fuel cell. This process is illustrated in Figure 1.1. Half cell reactions and the overall reaction in PEMFC are given as

$$\text{anode reaction:} \quad \mathrm{H_2} \longrightarrow 2\,\mathrm{H^+} + 2\,\mathrm{e^-}, \tag{1.1}$$

$$\text{cathode reaction:} \quad \tfrac{1}{2}\mathrm{O_2} + 2\,\mathrm{H^+} + 2\,\mathrm{e^-} \longrightarrow \mathrm{H_2O}, \tag{1.2}$$

$$\text{overall reaction:} \quad \mathrm{H_2} + \tfrac{1}{2}\mathrm{O_2} \longrightarrow \mathrm{H_2O}. \tag{1.3}$$

The reaction occurs at the anode is also called hydrogen oxidation reaction (HOR). The cathode reaction is also termed as oxygen reduction reaction (ORR). The Gibbs free energy change between the reactants and products in the overall reaction is converted to electric power. At standard ambient condition, the ideal open-circuit voltage of a PEMFC with respect to the standard hydrogen electrode (SHE) is 1.23 V. In practice, neither the hydrogen fuel stream contains pure hydrogen nor does the oxygen stream contain pure oxygen. This kind of a dilute supply of the reactants to the cell leads to a decrease in their chemical potentials. The actual open-circuit voltage is represented by the Nersnt equation,

$$U = U^0 + \frac{RT}{2F} \ln \left[\frac{p_{\mathrm{H_2}} p_{\mathrm{O_2}}}{p_{\mathrm{H_2O}}} \right] \tag{1.4}$$

where U_0 is the open-circuit voltage under standard ambient condition, T is the temperature, R and F are gas constant and Faraday constant, respectively, and $p_{\mathrm{H_2}}$, $p_{\mathrm{O_2}}$, and $p_{\mathrm{H_2O}}$ are partial pressures of hydrogen, oxygen, and steam, respectively.

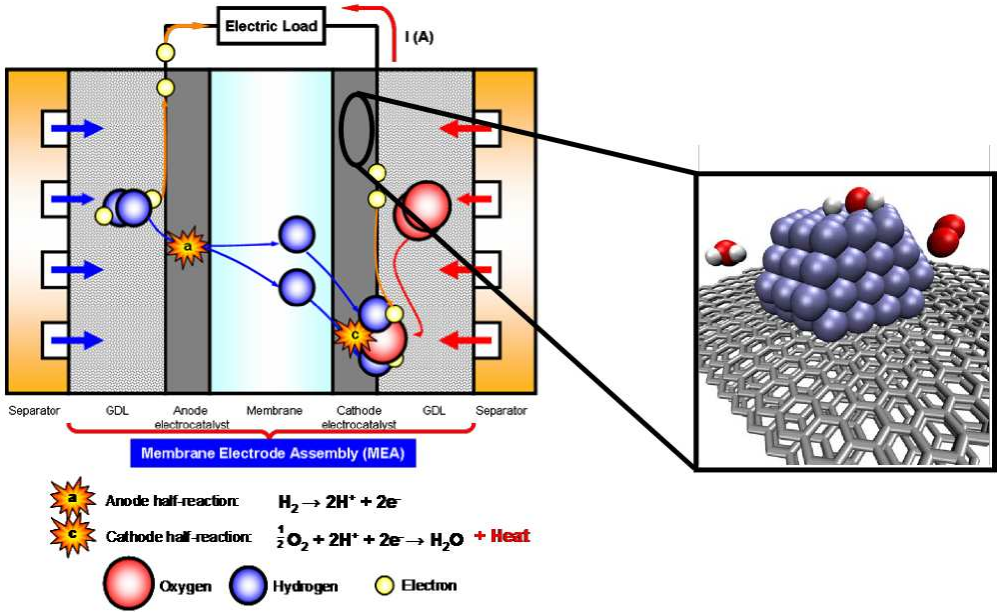

Figure 1.1: Illustration of the basic processes and components in a PEMFC.

Figure 1.1 also gives the typical components of a PEMFC stack unit. The outermost layer is bipolar plates for cell interconnection. It also serves as a means for feeding oxygen to the cathode and hydrogen fuel to the anode. The second layer from the outside is the gas diffusion layer which is made of porous materials. The hydrophobic Teflon often added to the porous gas diffusion layer helps in removing this excess water. The next layers inside are cathode and anode electrodes. Both electrodes are usually Pt or Pt alloy nanoparticles supported on graphite (see the right figure in Figure 1.1). The middle layer is the electrolyte layer called proton exchange membrane (PEM), after which the PEMFC is named. The PEM is a good conductor of protons, which are generated at the anode of a PEMFC. At the mean time, PEM must be an insulator of electrons so the electrons generated at the anode can flow to the outer circuit to do work. Thus, the role of the membrane is central to the proper working and performance of a PEMFC. The assembly of all the layers except the bipolar plates is called the membrane electrode assembly (MEA).

The performance of fuel cells is usually described by a polarization curve (voltage-current curve). A typical polarization curve for a PEMFC is shown in Figure 1.2. The mechanisms

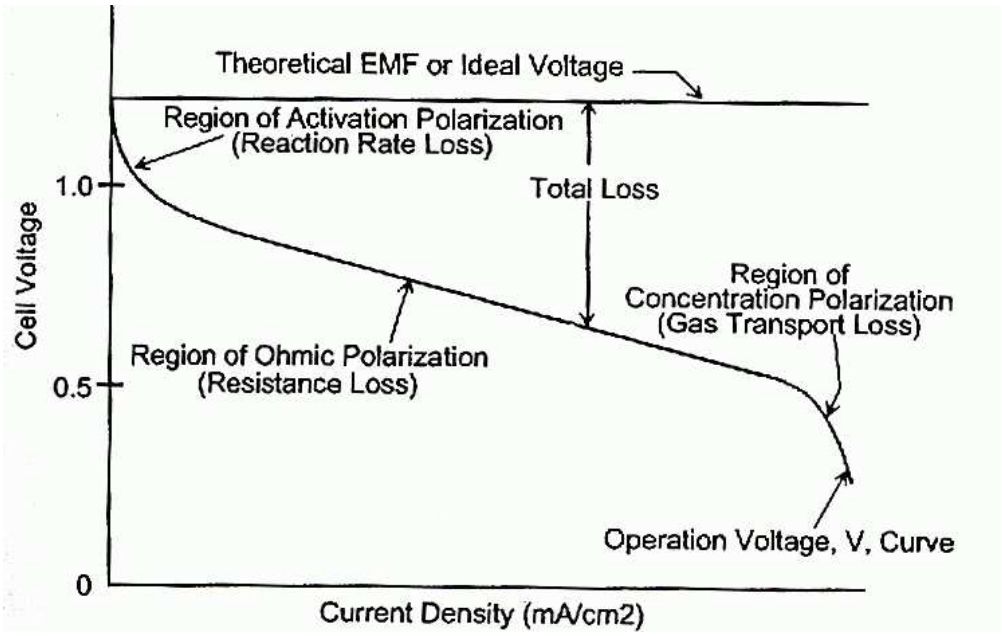

Figure 1.2: Polarization curve and loss mechanisms in a typical PEMFC.

for the losses are shown in the same figure. Reaction rate losses or overpotential losses are caused by the slow reaction kinetics at the electrodes. In hydrogen-fueled PEMFCs, these losses occur most significantly at the cathode, where the oxygen reduction reaction (ORR) takes place. Even on the best catalysts like Pt, activation losses due to slow rate of the ORR lead to an efficiency loss of around 20 %. Resistance losses or Ohmic losses are due to the flow of current through the finite resistances associated with the membrane, the cell interconnects, and the bipolar plates. Mass-transport losses occur at high current densities where consumption of the fuel and oxygen results in a drop in their partial pressure in the supply streams. This is more pronounced at high current densities when the pressure drop is further aggravated by the mass transport limitations of the supply channels, which may get clogged due to excessive production of liquid water. This can dramatically reduce the operating voltage. The loss due to the sluggish reaction kinetics of ORR on Pt catalyst is the main concern in this study.

	1. Oxygen dissociation	2. Peroxyl dissociation	3. Hydrogen peroxide dissociation
(a)	$O_2 + * \longrightarrow O_2^*$	$O_2 + * \longrightarrow O_2^*$	$O_2 + * \longrightarrow O_2^*$
(b)	$O_2^* + * \longrightarrow O^* + O^*$	$O_2^* + H^+ + e^- \longrightarrow OOH^*$	$O_2^* + H^+ + e^- \longrightarrow OOH^*$
(c)	$O^* + H^+ + e^- \longrightarrow OH^*$	$OOH^* \longrightarrow O^* + OH^*$	$OOH^* + H^+ + e^- \longrightarrow H_2O_2^*$
(d)	$OH^* + H^+ + e^- \longrightarrow H_2O$	$O^* + H^+ + e^- \longrightarrow OH^*$	$H_2O_2^* \longrightarrow OH^* + OH^*$
(e)		$OH^* + H^+ + e^- \longrightarrow H_2O$	$OH^* + H^+ + e^- \longrightarrow H_2O$

Figure 1.3: Three possible mechanisms for oxygen reduction reaction.

The oxygen reduction reaction includes a series of elementary steps which constitute the overall mechanism. Although the overall reaction for the ORR is given by Equation 1.3, different reaction pathways, each with a different rate-determining step, have been proposed for the ORR.[2] The three main pathways for ORR are the oxygen dissociation (O_2), peroxyl (OOH) dissociation, and hydrogen peroxide (H_2O_2) dissociation. In Figure 1.3, we displayed the detailed elementary steps for these three possible mechanisms of ORR. In common, each mechanism consists of one O–O bond scission step and a series of hydrogenation steps. The main difference among these three mechanisms lies in how the O–O bond scission occurs: in oxygen dissociation mechanism, the O–O bond scission step happens through O_2 dissociation immediately following O_2 adsorption on the surface; in peroxyl dissociation mechanism, the O–O bond scission step happens through a dissociation of OOH into O and OH species following a preceding O_2 protonation step; and in hydrogen peroxide dissociation mechanism, OOH is further protonated to form H_2O_2 and then the O–O bond scission is accomplished by H_2O_2 dissociating into two OH molecules.

As mentioned previously, the kinetics of ORR is much slower than that of HOR, and becomes a major reason for the loss of efficiency in PEMFC even on Pt catalyst which is the best among pure metal catalysts. Consequently, much research effort has been devoted to finding low-cost, high-performance, and long-durability electro-catalysts as the cathode of PEMFC.[3–7] In particular, alloying precious Pt with other transition metals has been

used as an effective approach to tailoring the electronic structure and activity for ORR of Pt-based catalysts.[8,9] For example, Adzic et al.[10,11] deposited monolayer Pt on the surface of various transition metal surfaces and found that the Pt monolayer on Pd (111) substrate led to significantly improved catalytic activity for ORR. Using annealing technique, Stamenkovic et al.[12,13] investigated the catalytic activities of surface segregated Pt alloys for ORR and found that the annealed Pt_3Ni and Pt_3Co alloys with Pt enriched outermost layer had much higher catalytic activity than poly-crystalline Pt. It has been justified by experiments and Monte Carlo simulations that the annealed Pt_3Ni and Pt_3Co alloys surfaces and subsurfaces are enriched and depleted with Pt due to the Pt surface segregation. The enhanced ORR activity on the Pt-segregated alloy surfaces are closely related to this specific surface compositional profile.

Theoretical works have been dedicated to explaining the effects of alloying on the chemical properties of surfaces of catalysts. First-principle density functional theory (DFT) calculations have been widely employed to establish the correlation between surface (most relevantly, the outermost layer and sub-surface layer) composition and catalytic activities of Pt alloys. It has been elaborated by Hammer and Nørskov that the calculated d-band center of transition metal surfaces is a useful indicator to measure the chemical reactivity of metallic catalysts.[14] Specifically, the difference in energy of the d-band center with respect to the Fermi level of metallic surfaces was found to well correlate to the O adsorption energy on these surfaces.[14] For ORR, some downshift of the d-band center with respect to that of pure Pt would lead to slightly weaker oxygen adsorption on the surface and was believed to enhance the reaction activity on such metallic catalysts.[8,9] Varying the type of subsurface transition metals has been shown to fine-tune the position of the d-band center of the outermost monolayer Pt and thus becomes a possible approach to designing Pt alloy catalysts for ORR.[15,16] Furthermore, the optimized structure and energy of reactant, intermediate, and product species (such as, O_2, O, OH, and H_2O) adsorbed on the pure Pt and Pt alloy surfaces could be reliably computed using the DFT method.[17–24] It was found that there was a strong linear correlation between the adsorption energies of O and OH[25], which are important factors governing the rate of ORR on metallic catalyst surfaces. It is widely believed that an optimal catalyst for ORR should bind the reactant intermediates

neither too weakly nor too strongly.[26] If the catalyst binds O too weakly on its surface, the possibility for ORR to occur will be limited. On the other hand, if the catalyst binds OH too strongly on its surface, the availability of active sites on the catalyst surface will be reduced. As a result, a volcano plot is normally observed when plotting the catalytical activity for ORR as a function of the calculated O adsorption energy (or the position of d-band center). An ideal catalyst for ORR must keep an optimal balance between retaining O on the surface and removing OH from the surface. These studies proposed that the Pt surfaces modified by subsurface transition metals (such as, Ni, Co, or Fe) would exhibit better catalyst performance for ORR than pure Pt because the weaker adsorption of OH on these surfaces could improve the availability of the active sites of the catalysts.[8,9] This theoretical argument supports well the systematic experimental measurements for various Pt alloy catalysts. [10,12] However, previous DFT calculations focused primarily on the heat of reactions for various elementary reactions of ORR. In this work, we calculated not only the heat of reactions but also the activation energy of all possible ORR elementary reactions on the surface of catalysts. In this way, we were able to gain further insights into the mechanism of ORR on the catalyst surfaces.

First-principle DFT calculation with climbing image nudged elastic band (CI-NEB) method could be used to find the transition state of chemical reactions.[27,28] This computational approach has already been employed to determine the activation barriers of some elementary steps (such as, O_2 dissociation, O hydrogenation, O_2 hydrogenation, and OH hydrogenation) of ORR catalyzed by pure Pt.[29–32] For instance, it was predicted that the activation energy for direct O_2 dissociation to be about 0.27 eV on a $2\sqrt{3} \times 4$ surface cell (representing a low O coverage) but about 0.52 eV on a $\sqrt{3} \times 2$ surface cell (representing a high O coverage) of Pt (111) in vacuum condition, indicating a strong dependence of the direct O_2 dissociation process on oxygen coverage.[29] In addition, the activation energy for direct O_2 dissociation reaction had been shown to be affected by the existence of acid electrolyte,[30] co-adsorbed sodium and water,[31] or electrode potential.[32] Yielding kinetic information of ORR on catalyst surface, first-principle transition state calculations have also been successfully used to evaluate the catalytic activity of core-shell particles with a series of core metals[33] and elucidate the mechanism of ORR on the surface of different transition

metals.[34] By utilizing the DFT and CI-NEB methods, the activation energies of various elementary steps of the three proposed ORR pathways can be calculated. Thus, the rate-determining steps of ORR on pure Pt (111) surface and Pt alloy surfaces can be identified, which could in principle reveals the reason of activity enhancement of ORR on Pt alloy surfaces in terms of ORR kinetics.

2.0 COMPUTATIONAL METHODS

2.1 DENSITY FUNCTIONAL THEORY

Density functional theory (DFT) is a first principle method directly based on quantum mechanics. It does not require any other input quantities but the atomic species and their coordinates as input to conduct the calculation. DFT methods have quickly become the most widely-spread first principle methods due to their high computational efficiency and very good accuracy. They have been used in evaluating a variety of problems in chemistry, physics, materials science, and many branches of engineering[35,36]. For example, DFT calculations have been used to elucidate the catalytic synthesis of ammonia on metal nanoparticles[37], the embrittlement of copper by traces of bismuth impurities[38], and probing material properties of magnesium silicate, a mineral important in planet formation, under extreme conditions[39]. DFT calculations enable researchers to study at the atomic level, but researchers utilizing these methods must remain mindful of the theory behind the calculations as well as both their capabilities and limitations. A brief overview of the fundamentals of density functional theory is provided in the remainder of this section.

2.1.1 Schrödinger's Equation

At the atomic level, materials are represented by both a positively-charged nucleus and negatively-charged electrons. Since the mass of the nucleus is orders of magnitude larger than the mass of an electron – the mass of a proton or neutron is roughly 1800 times greater than an electron – the nucleus is significantly slower than electrons in responding to changes in its surroundings. As a result, the motion of the nucleus can be separated from that of the

electrons, and the respective mathematical problems can be solved separately. This ability is the basis of the Born-Oppenheimer approximation[35]. Thus, only electrons interacting in the nuclear potential and electron-electron interactions remain. This approximation is used to simplify the time-independent Schrödinger equation:

$$\hat{H}\Psi = E\Psi \tag{2.1}$$

The particular definition of the Hamiltonian, $\hat{H}$, depends on the nature of the system being studied. For simple systems like a particle in a box or a harmonic oscillator, the Hamiltonian takes a simple form, and the Schrödinger equation can be solved exactly. Where multiple electrons are interacting with multiple nuclei, such as in a typical solid-state system, the Hamiltonian takes a more complicated form, as shown in the following equation:

$$\hat{H} = -\frac{\hbar^2}{2m_e}\sum_i \bigtriangledown^2 + \sum_i V(\mathbf{r}_i) + \frac{1}{2}\sum_{i\neq j}\frac{e^2}{|\mathbf{r}_i - \mathbf{r}_j|} \tag{2.2}$$

The terms in the Hamiltonian are the electronic kinetic energy, the energy of the interaction between each electron and all nuclei, and the energy of the interaction between electrons, respectively. For this Hamiltonian, Ψ is the electronic wave function, and E is the ground-state energy.

In 1964, the modern formulation of density functional theory was born when Hohenberg and Kohn proved two fundamental theorems.[40] First, they illustrated that all properties, including the ground-state energy, of a quantum many-body system can be considered as unique functionals of the ground-state electron density. As a result, instead of requiring wave functions of 3N variables to solve the Schrödinger equation, only the electron density, a function of three spatial variables is required. Second, they showed that the electron density that minimizes the total energy is indeed the true electron density that corresponds to the solution of the Schrödinger equation. Unfortunately, the true functional form of the electron density is unknown, so approximate forms of the functional are used together with this variational principle to determine an approximate solution to the Schrödinger equation.

2.1.2 Kohn-Sham equations

Shortly after Hohenberg and Kohn published their arguments, Kohn and Sham provided a formulation of density functional theory[41] that has become the foundation for many of the current methods of tackling the full many-body electron problem. They determined a way to express the true electron density such that each equation only involves a single electron, which is shown in the following equation:

$$\left[-\frac{\hbar^2}{2m_e}\bigtriangledown^2 + V(\mathbf{r}) + V_H(\mathbf{r}) + V_{xc}(\mathbf{r})\right]\psi_i = \epsilon_i\psi_i \tag{2.3}$$

Of the three potentials that appear on the left-hand side of the equation, only the first potential, $V(\mathbf{r})$, also appeared in the full Schrödinger equation; it defines the interaction between each electron and all nuclei. The second potential, $V_H(\mathbf{r})$, is the Hartree potential, which describes the Coulomb repulsion between one electron and the total density of all electrons, including itself. The third potential, $V_{xc}(\mathbf{r})$, defines exchange and correlation contributions.

In order to solve the Kohn-Sham equations, an iterative process is necessary, which often begins by defining an initial, trial electron density, and then solving the Kohn-Sham equations using this trial density to determine the single-electron wave functions. The electron density is then calculated using these wave functions. If the two electron densities match, then the ground-state electron density has been obtained and can be used to calculate the total energy. If the two electron densities differ, then the trial density must be changed in some way, and the process is repeated. This procedure ensures a self-consistent solution to the Kohn-Sham equations.

2.1.3 Exchange-Correlation Functionals

The exact form of the exchange-correlation functional $V_{xc}(\mathbf{r})$ is still unknown, even though its existence is guaranteed by the Hohenberg-Kohn theorem. Thus, various approximations must be made in order to completely define the Kohn-Sham equations, and subsequently, obtain an approximate solution to the Schrödinger equation.

The local density approximation (LDA) assumes that the exchange-correlation potential is the known exchange-correlation potential of a homogeneous electron gas at the observed electron density.

$$V_{xc}(\mathbf{r}) = V_{xc}(n(\mathbf{r})) \tag{2.4}$$

In practice, LDA has been shown to be more suited for systems with slowly varying electron densities, such as those like a nearly-free-electron metal. LDA overestimates bond energies, and as a result, predicts shorter bond lengths than those observed experimentally, but it often agrees well with structural and vibrational experimental data.

The generalized gradient approximation (GGA) is similar in form to the LDA, but it assumes that the exchange-correlation potential also depends on the gradient of the electron density.

$$V_{xc}(\mathbf{r}) = V_{xc}(n(\mathbf{r}), \bigtriangledown n(\mathbf{r})) \tag{2.5}$$

Here, $\bigtriangledown n(\mathbf{r})$ is a gradient of the electron density and is useful in describing systems where the electron density varies more sharply, such as surfaces and small molecules. In general, GGA is more accurate than LDA, but it often underestimates bond energies, and as a result, overestimates parameters such as lattice constants. Because the gradient of the electron density can be included in different ways, many variations of the GGA functional exist. The two most common are the Perdew-Wang (PW91) functional[42] and the Perdew-Burke-Ernzerhof (PBE) functional.[43]

2.1.4 Pseudopotentials

One means of expanding the electronic wave functions is through the use of a series of plane waves. In order to represent all of the electrons associated with a particular atom, very large plane wave sets would be required. Core electrons, however, are not generally important in chemical bonding or defining material properties. Thus, the use of pseudopotentials to approximate the core electrons and reduce the number of plane waves required, while maintaining the character of valence electrons, is advantageous. The electron density of the core electrons is replaced with a smoothed density that approximates the properties of the true ionic core, such as the nuclear attraction and inner electron repulsion, and is then

fixed. Calculations using this frozen core approximation are more common than all-electron calculations. Two classes of pseudopotentials exist: ultrasoft pseudopotentials (USPP) and projector augmented wave (PAW) pseudopotenials. For many systems, these methods give very similar results; however, in systems with strong magnetic moments or large differences in electronegativity, the PAW pseudopotentials are more reliable.

2.2 MODIFIED EMBEDDED ATOM METHOD

The detailed description of the modified embeded atom method (MEAM) formalism applied to cubic and hcp metals has been documented in the literature.[44,45] Hence, we only give a brief description below.

Within the MEAM, the total energy of a system is calculated as

$$E = \sum_i \left[F(\bar{\rho}_i) + \frac{1}{2} \sum_{j(\neq i)} \Phi(R_{ij}) \right] \tag{2.6}$$

In the above equation, $\bar{\rho}_i$ is the background electron density at the center of atom i obtained by the superposition of electronic densities from its neighboring atoms. The first term is the embedding energy for atom i which is embedded into the electron density $\bar{\rho}_i$, and the second term is the core-core pair repulsion between atoms i and j separated by a distance R_{ij}.

The embedding energy is given as follows:

$$F(\bar{\rho}) = AE_c \left(\frac{\bar{\rho}}{\overline{\rho^0}} \right) \ln \left(\frac{\bar{\rho}}{\overline{\rho^0}} \right) \tag{2.7}$$

Here, A is an adjustable parameter, E_c is the cohesive energy, and $\overline{\rho^0}$ is the density scaling factor.

The electron density $\overline{\rho_i}$ is composed of the spherically symmetric partial electron density $\rho_i^{(0)}$ and the angular contributions $\rho_i^{(1)}$, $\rho_i^{(2)}$, and $\rho_i^{(3)}$. These partial electron densities have the following forms:

$$\rho_i^{(0)} = \sum_{j(\neq i)} \rho_j^{a(0)}(R_{ij}), \tag{2.8a}$$

$$(\rho_i^{(1)})^2 = \sum_{\alpha} \left[\sum_{j(\neq i)} x_{ij}^{\alpha} \rho_j^{a(1)}(R_{ij}) \right]^2, \tag{2.8b}$$

$$(\rho_i^{(2)})^2 = \sum_{\alpha,\beta} \left[\sum_{j(\neq i)} x_{ij}^{\alpha} x_{ij}^{\beta} \rho_j^{a(2)}(R_{ij}) \right]^2 - \frac{1}{3} \left[\sum_{j(\neq i)} \rho_j^{a(2)}(R_{ij}) \right]^2 \tag{2.8c}$$

$$(\rho_i^{(3)})^2 = \sum_{\alpha,\beta,\gamma} \left[\sum_{j(\neq i)} x_{ij}^{\alpha} x_{ij}^{\beta} x_{ij}^{\gamma} \rho_j^{a(3)}(R_{ij}) \right]^2 - \frac{3}{5} \sum_{\alpha} \left[\sum_{j(\neq i)} x_{ij}^{\alpha} \rho_j^{a(3)}(R_{ij}) \right]^2 \tag{2.8d}$$

Here, $x_{ij}^{\alpha} = R_{ij}^{\alpha}/R_{ij}$, and R_{ij}^{α} is the α component ($\alpha = x,\ y,$ or z) of the distance vector between atoms i and j. $\rho_j^{a(h)}(R_{ij}) = e^{-\beta^h(R_{ij}/r_e - 1)}$ ($h = 0,\ 1,\ 2,$ and 3) represents the atomic electron densities contributed from atom j to atom i, $\beta^{(h)}$ are adjustable parameters, and r_e is the nearest-neighbor distance in the equilibrium reference structure. Note that Equation (2.8d) is different from that in earlier work(for example, Refs. 44 and 45). This new modification makes the partial electron densities orthogonal.[46] In the study, we use the following scheme (see other schemes in Ref. 47) to combine the partial electron densities and compute the background electron density:

$$\overline{\rho_i} = \rho_i^{(0)} \sqrt{1 + \Gamma_i}, \tag{2.9a}$$

$$\Gamma_i = \sum_{h=1}^{3} t^{(h)} \left[\rho_i^{(h)} / \rho_i^{(0)} \right]^2, \tag{2.9b}$$

where $t^{(h)}$ are adjustable parameters.

The pair potential between two atoms seperated by a distance R is given by

$$\Phi(R) = \frac{2}{Z} \left\{ E^u(R) - F[\rho^0(R)] \right\}, \tag{2.10}$$

where Z is the number of nearest neighbors in the bulk reference structure. $E^u(R)$ is the energy per atom of the reference structure as a function of nearest-neighbor distance R and is determined using the following universal equation of state of Rose *et al.*:[48]

$$E^u(R) = -E_c(1 + a^*)e^{-a^*}, \tag{2.11a}$$

$$a^* = \alpha(R/r_e - 1), \tag{2.11b}$$

$$\alpha = \sqrt{\frac{9\Omega B}{E_c}}. \tag{2.11c}$$

Here, E_c, r_e, Ω, and B are the cohesive energy, nearest-neighbor distance, atomic volume, and bulk modulus for the equilibrium reference structure, respectively.

$\overline{\rho^0}(R)$ in Equation 2.10 is the background electron density for the reference structure. For fcc metals,

$$\text{fcc metal:} \quad \overline{\rho^0}(R) = Z\rho^{a(0)}(R). \tag{2.12a}$$

$$\text{hcp metal:} \quad \overline{\rho^0}(R) = Z\rho^{a(0)}(R)\sqrt{1 + \frac{t^{(3)}}{3Z^2}\left(\frac{\rho^{a(3)}}{\rho^{a(0)}}\right)^2}. \tag{2.12b}$$

The current version of the MEAM considers only nearest-neighbor interactions; therefore, we must provide a screening procedure to define which are the nearest neighbors of an atom. We use the many-body screening function proposed by Baskes[47] using the elliptical construction.

The screening function S_{ijk} between atoms i and k depends on all the other atoms between them; thus

$$S_{ik} = \prod_{j \neq i,k} S_{ijk}, \tag{2.13a}$$

$$S_{ijk} = f_c\left(\frac{C - C_{\min}}{C_{\max} - C_{\min}}\right), \tag{2.13b}$$

where $f_c(x)$ is a function of the material dependent parameters $C_{\max}$ and $C_{\min}$. The parameter C is determined using the following equation:

$$C = \frac{2(X_{ij} + X_{jk}) - (X_{ij} - X_{jk})^2 - 1}{1 - (X_{ij} - X_{jk})^2}, \tag{2.14}$$

where $X_{ij} = (r_{ij}/r_{ik})^2$ and $X_{jk} = (r_{jk}/r_{ik})^2$. The r_{ij}, r_{jk}, and r_{ik} are the distances between the corresponding atoms.

The smooth cutoff function $fc(x)$ in Equation 2.13b assumes the following form:

$$\text{if } x \geq 1,\ f_c(x) = 1, \tag{2.15a}$$

$$\text{if } 0 < x < 1,\ f_c(x) = [1 - (1 - x)^2]^2, \tag{2.15b}$$

$$\text{if } x \leq 0,\ f_c(x) = 0. \tag{2.15c}$$

We multiply the atomic electron density and the pair potentials by the screening function S_{ik}; here $S_{ik} = 1$ represents unscreened interaction while $S_{ik} = 0$ represents a completely screened interaction.

3.0 MODELING SURFACE SEGREGATION PHENOMENA IN THE (111) SURFACE OF ORDERED PLATINUM [SUB 3] TITANIUM CRYSTAL

3.1 ABSTRACT

We investigated the surface segregation phenomena in the (111) surface of ordered Pt_3Ti crystal using density functional theory (DFT) calculation with no configuration sampling and Monte Carlo (MC) simulation method employing modified embedded atom method potentials and with extensive configuration sampling. Our DFT study suggested that the off-stoichiometric effect (specifically, a Pt concentration higher than 75 at. %) accounted for the experimentally observed Pt segregation to the outermost layer of the Pt_3Ti (111) . Our MC simulations predicted that in a Pt_3Ti (111) sample with a Pt concentration slightly above 75 at. %, Pt atoms would segregate to the surface to form a pure Pt outermost layer, while the ordered Pt_3Ti crystal structure would be maintained in the second layer and below. Moreover, our DFT calculations revealed that the d-band center of the Pt-segregated Pt_3Ti (111) surface would downshift by 0.21 eV as compared to that of a pure Pt (111) surface. As a result, O adsorption energy on the Pt-segregated Pt_3Ti (111) surface was found to be at least 0.16 eV weaker than that on the pure Pt 111 surface. Thus, we theoretically modeled the geometric and electronic structures of the Pt-segregated Pt_3Ti (111) surface and further suggested that the Pt surface segregation could lead to enhanced catalytic activity for oxygen reduction reactions on Pt_3Ti alloy catalysts.

3.2 INTRODUCTION

The surface segregation process in alloy materials normally causes their chemical composition in the surface region to differ from their bulk composition[49,50]. Thus, the surface segregation phenomenon in materials significantly influences material properties such as adsorption, wetting, oxidation,corrosion, electrical contact, friction and wear, crystal growth, and catalysis. Surface segregation can occur in both disordered and ordered alloys. For disordered binary alloys or binary solid solutions , there are three major physical mechanisms that promote surface segregation. If the heat of the solution is negative, the majority component of the alloy will enrich the surface to maximize the mixing of the two components in bulk. When the atomic sizes of the two components are dramatically different, one component will segregate to the surface to reduce strain energy in the alloys. The component in its pure element form with a lower surface energy will segregate to the alloy surface. The surface segregation process in disordered alloys is always exothermic and accompanies a decrease in system configurational entropy. On the other hand, the surface segregation process in ordered binary alloys increases system configurational entropy and, hence, can be either endothermic or exothermic.[51] Besides above, surface segregation in ordered alloys can be a result of the generation and motion of antisite defects due to the off-stoichiometric effect.[52] Theoretically predicting surface segregation in binary alloys has long been pursued.[13,53–60] In particular, microscopic theories, involving both evaluating energies with some theoretical models for examples, tight-binding theory (TBT), embedded atom method (EAM), density functional theory (DFT) and sampling distinct configurations using statistical mechanics methods, have been widely employed to attain the equilibrium compositions of alloy surfaces. Most previous work has studied the surface segregation in disordered alloy systems. In the present work, we applied the same computational approach to predicting the surface segregation in ordered Pt_3Ti (platinum-titanium) crystal.

Catalytic activities of bimetallic alloys are mainly determined by their surface structure and composition. Consequently, we can take advantage of surface segregation to design and synthesize high-activity catalysts. For instance, Pt is an efficient catalyst in many important chemical reactions, such as O_2 reduction and hydrocarbon reforming. However, Pt is a

precious metal. It is desirable to develop new catalysts with reduced Pt content yet good performance. For this reason, many researchers have focused on studying Pt-based bimetallic alloys, in which some of the Pt content was replaced with less expensive metals.[8,12,15,61–65] It was further found that due to surface segregation, some Pt binary alloys had enhanced activities for oxygen reduction reactions (ORRs).[8,12,62] For example, surface segregation leads to 100% Pt in the outermost layer, but only 50% Pt i.e., 50% Ni in the sublayer of the Pt_3Ni (111) surface. The Ni atoms beneath the Pt monolayer shift the d electron band of the Pt toward a higher catalytic activity for the ORR.[12] To rationally design Pt alloy catalysts using the surface segregation process, it is essential to establish the correlation between surface composition and catalytic activities of the alloys. To this end, more efforts have been devoted to either experimentally examining the catalytic activities or theoretically determining the d electron band structures for monolayer metals deposited on Pt. In this work, we first predicted the composition of the Pt_3Ti (111) surface by simulating the surface segregation process, and then we calculated the electronic structure and the O adsorption on the Pt-segregated Pt_3Ti (111) surface using a first-principles DFT method. This study provides us insights about how surface segregation may alter the catalytic performance of Pt_3Ti crystal.

Pt-Ti alloys have a large negative heat of solution because of the strong bonding interactions in the d-orbitals of the Pt and Ti atoms. This property leads to the superior chemical stability of Pt_3Ti crystal. Moreover, Pt_3Ti crystal has quite good catalytic performance for ORRs. It was found that carbon-supported $Pt_{75}Ti_{25}$ nanoparticles displayed a twofold improvement in catalytic activities (or a 20 mV shift to a higher potential) toward molecular oxygen electroreduction, as compared to a benchmark Pt/C catalyst.[66,67] As for the surface segregation in Pt_3Ti crystal, low energy electron diffraction (LEED) structural analysis found that in the (111) surface, one pure Pt outermost layer will be formed on top of the bulk lattice structure of the Pt_3Ti,[68] while in the (001) surface, the bulk-terminated pure Pt layer will be the outermost layer.[69] With ultraviolet photoemission spectroscopy, Mun et al. observed that the position of the d-band center of Pt_3Ti polycrystals moves away from the Fermi level after annealing in a vacuum, suggesting the formation of a pure Pt outermost surface layer.[63] The surface segregation process in ordered Pt_3Ti crystal is

quite different from other disordered Pt alloys.[57–60] Theoretical calculations showed that the surface segregation phenomena in most Pt alloys (like Pt_3Co, Pt_3Ni, and Pt_3Fe) could be explained by simply exchanging the Pt atoms in the sublayer with the second-element atoms in the outermost layer. However, the same study found out that surface segregation in Pt_3Ti could not be obtained in this way.[70] In this work, we elaborated on the surface segregation process in the (111) surface of ordered Pt_3Ti crystal using atomistic modeling techniques.

3.3 COMPUTATIONAL METHODS

3.3.1 Density functional theory calculations

In this work, a first-principles DFT method was employed to determine some bulk and surface properties of PtCTi alloys. In particular, we used the DFT method to study the possible routes for Pt segregating to the (111) surface of Pt_3Ti crystal. We used the Vienna Ab Initio Simulation Package (VASP) for these calculations.[71,72] The DFT calculations were performed with the projector augmented wave (PAW) and the pseudopotential approach.[73,74] The generalized gradient approximation with the PW91 functional by Perdew and co-workers[42] was used for evaluating the exchange-correlation energy. The plane-wave cutoff energy was set to 600 eV in all the calculations. A 16×16×16 Monkhorst- Pack k-point mesh[75] was used for Brillouin zone integration in our bulk alloy unit cell calculations, while a 4×4×1 k-point mesh was used for our surface slab calculations. The optimized atomic geometry was obtained by minimizing the HellmanCFeynman forces till the force acting on each atom was smaller than 0.05 eV/Å.

3.3.2 The Monte Carlo method

Monte Carlo (MC) simulation methods based on Metropolis algorithm[76] have been successfully used in previous surface segregation calculations for various alloys (for example, Pt-Ni[77], Ni-Cu[78], and Al-Mg[79]). These MC methods are particularly advantageous in

studying segregation phenomena in the equilibrium alloy structure, because they can circumvent slow physical dynamic processes (such as diffusion) in the system and provide an averaged composition profile over a thermodynamic equilibrium ensemble.

In our calculations, we used statistical mechanics with a canonical ensemble, where the total number of atoms of each element and the temperature are constants. In this approach, starting from some atomic configuration, the successive configurations are generated in proportion to the probabilities of a configuration occurring in the equilibrium ensemble. In each step, one of the following two configuration transformations is tried out with an equal probability:

(1) A randomly selected atom is displaced from its original position in random direction. The magnitude of the displacement is in the range of (0, $r_{\max}$]. At a given temperature, the maximum displacement rmax is tuned so that the acceptance rate of new configurations is about 0.5 during the equilibrated part of the simulations.

(2) Two randomly selected atoms with different element types are exchanged.

The operation (1) accounts for the relaxation and vibration processes, and the operation (2) accounts for the inter-diffusion process in the model system.

According to the Boltzmann distribution, the probability (P_{XY}) of the configuration transformation (from X to Y) is given by a Boltzmann factor for the change in energy ($\Delta E = E_Y - E_X$):

$$P_{XY} = \exp\left(-\frac{\Delta E}{k_B T}\right). \tag{3.1}$$

Here, k_B is the Boltzmann constant and T is the temperature. If $P_{XY} \geq 1$ (decrease in system energy), the new configuration is always retained, while if $P_{XY} < 1$ (increase in energy), the new configuration is accepted with the probability P_{XY}. After repeating the above procedures for multimillion MC steps, the physical quantities such as the composition profile are obtained by averaging over the resulting configurations.

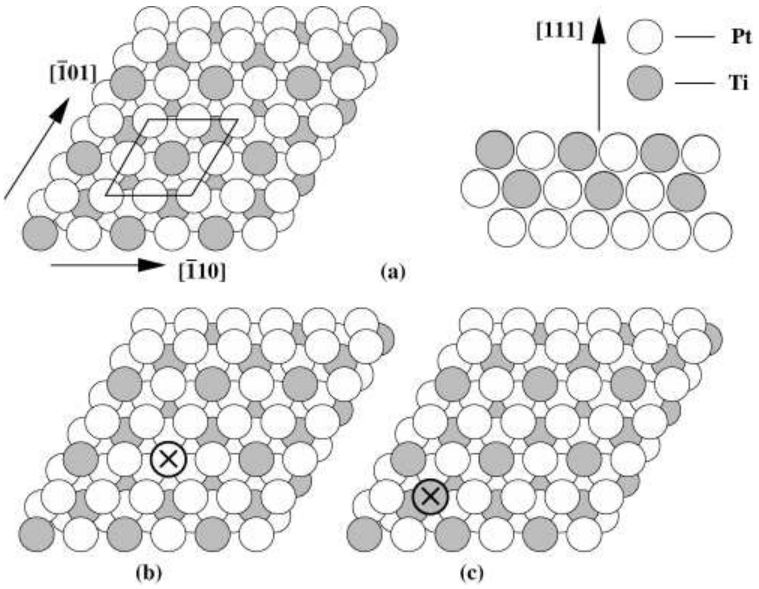

Figure 3.1: Atomic structures of the bulk-terminated Pt_3Ti (111) surface, a Pt antisite (Pt_{Ti}) defect, and a Ti antisite (Ti_{Pt}) defect.

3.4 RESULTS AND DISCUSSION

3.4.1 DFT study of surface segregation in Pt_3Ti (111)

In its equilibrium form, the Pt_3Ti alloy adopts an $L1_2$ crystal structure in which one Ti atom lies at the corner and three Pt atoms lie at the face centers of a face-centered cubic lattice. The lattice parameter of the Pt_3Ti ($L1_2$) crystal was predicted from our DFT calculations to be 3.956 Å, which is about 1.28 % larger than the experimental data of 3.906 Å.[80] We modeled the bulk-terminated (111) surface of the Pt_3Ti crystal with a surface slab (having two surfaces) in a periodic super cell, in which there were eight atomic layers and a 12 Å thick vacuum in the (111) direction normal to the surface. At each atomic layer, there were four atoms (three Pt atoms and one Ti atom) in a surface unit cell, as shown in Figure 3.1(a). Furthermore, we modeled the Pt-segregated Pt_3Ti (111) surfaces by changing the outermost layer of the bulk-terminated Pt_3Ti (111) to a pure Pt layer (*i.e.*, four Pt atoms but no Ti atoms). Then, we fully relaxed the atomic structures of all the modeled surface slabs with

the DFT method. Comparing the energies of these optimized surface models, we examined two possible routes for the Pt to segregate to the outermost layer of the Pt_3Ti (111).

Table 3.1: Calculated Pt surface segregation energy for the Pt_3Ti (111) surfacei, assuming a direct exchange route. Data are in the unit of eV.

Position of Pt atoms before exchange	DFT	MEAM
Second layer	0.68	1.40
Third layer	1.78	1.30
Fourth layer	1.97	1.28

Route I: Direct exchange. In this route, the segregation of the Pt atoms to the outermost layer of the Pt_3Ti (111) surface was accomplished by exchanging the positions of the surface Ti atoms with the interior Pt atoms. To examine this route, we computed the Pt surface segregation energy, which is the energy difference between Pt-segregated and bulk-terminated Pt_3Ti (111) surface models. The Pt-segregated surface model was constructed by exchanging the Ti atom in the outermost layer with a Pt atom at a subsurface layer of the bulk-terminated Pt_3Ti (111) model. Negative Pt surface segregation energy indicates that it was an exothermal process for the Pt atoms to segregate to the surface. Table 3.1 gives the calculated Pt surface segregation energies based on this route. Our results show that the Pt surface segregation energies were positive for exchanging the surface Ti atom with the Pt atom in the second, third, and fourth sublayers. Consequently, it was not energetically favorable for Pt atoms to segregate to the surface through this direct exchange route at low temperatures. Moreover, the calculated Pt surface segregation energy increased with the sequence number of the sublayer (where the exchanged Pt atom came from). Thus, exchanging the surface Ti atom with the second layer Pt atom led to the lowest Pt surface segregation energy, which is calculated here to be 0.68 eV and is in exact agreement with the previous DFT study.[70]

Route II: Antisite migration. In this route, the segregation of Pt atoms to the outermost layer of the Pt_3Ti (111) surface was achieved by migrating Pt antisites to the surface. An

antisite is an off-stoichiometric structural defect existing in ordered alloys.[81] In this work, a Pt antisite (denoted as Pt_{Ti}) refers to a Ti atom replaced by a Pt atom in the ordered Pt_3Ti crystal (Figure 3.1(b)), while a Ti antisite (denoted as Ti_{Pt}) refers to a Pt atom replaced by a Ti atom (Figure 3.1(c)). For this route, surface segregation energy was evaluated as the energy difference between the Pt_3Ti (111) surface slab model having an antisite defect in its surface region (at the first, second, and third atomic layers) and the one having an antisite in the bulk region (at the fourth atomic layer). We listed in Table 3.2 the calculated surface segregation energies from the DFT calculations. Our results in Table 3.2 show that it was most energetically favorable (gaining 1.25 eV) for Pt_{Ti} (i.e., excess Pt atoms) to migrate from bulk to the outermost layer of the Pt_3Ti (111) surface. In contrast, it was energetically favorable (gaining 0.37 eV) for Ti_{Pt} (i.e., excess Ti atoms) to migrate from the outermost layer to the interior layers of the Pt_3Ti (111) surface. Thus, our results infer that the off-stoichiometric effect in the Pt_3Ti crystals could have caused the Pt_{Ti} atoms to segregate to the outermost surface layer (when the Pt concentration was above 75 at. %) or the Ti_{Pt} atoms to move inside to the bulk (when the Pt concentration was below 75 at. %).

Table 3.2: Calculated Pt and Ti surface segregation energies for the Pt_3Ti (111) surface, assuming an antisite migration route. Data are in the unit of eV.

	Pt_{Ti}		Ti_{Pt}	
Position of antisite	DFT	MEAM	DFT	MEAM
First layer	−1.25	−1.12	0.37	1.27
Second layer	0.43	0.07	−0.18	−0.11
Third layer	−0.18	0.00	−0.10	−0.02

In summary, our DFT calculations above suggest that a direct exchange route requires at least 0.68 eV of energy to segregate Pt to the outermost layer of the Pt_3Ti (111) surface; hence, it is not energetically favorable. In contrast, an antisite migration route is energetically favorable to segregate Pt_{Ti} to the outermost layer of the Pt_3Ti (111) surface. Here, we would like to make some further comments on our DFT calculation study of the surface

segregation in the Pt_3Ti (111) surface. First, we have fully optimized the atomic structures and thus included strain relaxation in our DFT calculations. Without structural relaxation, the calculated Pt surface segregation energies would have been about 0.4 eV higher than those values in Table 3.1 for a direct exchange route and would have differed by about 0.1 eV from those values in Table 3.2 for an antisite migration route. However, no qualitative change (positive or negative sign change) in the Pt surface segregation energy was found. This indicates that the structural relaxation process did not alter the surface segregation process in the Pt_3Ti (111) surface. Second, it can be considered that two antisite defects are generated in a direct exchange exchange route, but only one antisite defect is generated in an antisite migration route. Consequently, the calculated Pt surface segregation energies (Table 3.1 for the direct exchange route and Table 3.2 for the antisite migration route) should not be directly compared with each other. Third, our calculated surface segregation energies in Tables 3.1 and 3.2 are the energy differences between the initial and final configurations during the Pt segregation process. Hence, our DFT calculations here indicate only the thermodynamic feasibility of a Pt segregation route, but not the exact migration paths and their corresponding energy barriers. In kinetics, both routes consist of multiple atomic diffusion processes through Pt_3Ti crystal.

3.4.2 MC study of surface segregation in Pt_3Ti (111)

DFT calculations are very accurate in predicting material system geometries and energies at 0 K. However, prohibitively high computation resources are required to reasonably sample possible configurations of the material system at high temperatures. In order to take a configurational entropy contribution into account when studying the surface segregation of Pt_3Ti (111), we employed both the MC simulation method to generate a configuration ensemble and the MEAM to evaluate the energies of various configurations.

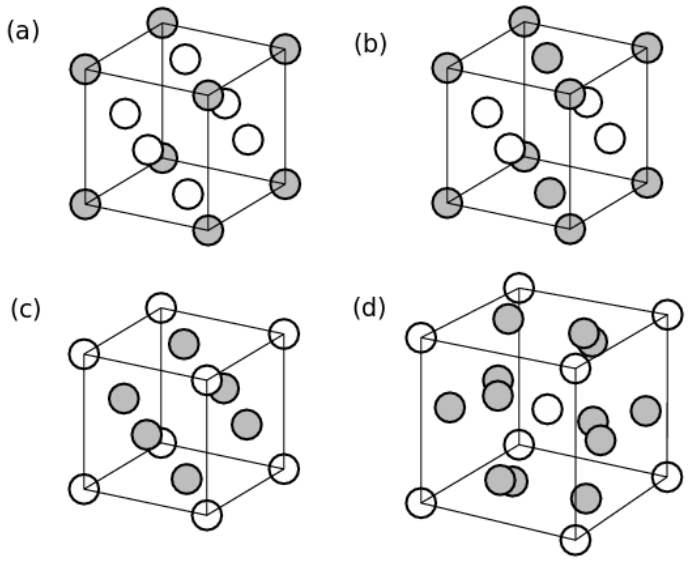

Figure 3.2: Lattice structures of Pt-Ti intermetallic crystals. (a) Pt_3Ti with an $L1_2$ structure, (b) Pt_{Ti} with an $L1_0$ structure, (c) $PtTi_3$ with an $L1_2$ structure, and (d) $PtTi_3$ with an A15 structure.

In this work, the MEAM potentials for pure Pt and Ti metals were similar to those in Refs. 44 and 45, with some renormalized scaling factors in the atomic charge densities. To develop the Pt-Ti alloy potential, the Pt_3Ti crystal ($L1_2$-type, Figure 3.2(a)) was taken as the reference phase. The same formula of the cross part describing Pt-Ti interactions was adopted in Refs. 58, 57, and 60.

Table 3.3: Parameters of the MEAM potentials for the Pt_3Ti system.

	E_c	r_e	α	A	$\beta^{(0)}$	$\beta^{(1)}$	$\beta^{(2)}$	$\beta^{(3)}$	$t^{(0)}$	$t^{(1)}$	$t^{(2)}$	$t^{(3)}$	ρ^0
Pt	5.77	2.772	6.44	1.04	4.67	2.2	6.0	2.2	1.0	4.7	−1.38	3.29	1.1
Ti	4.874	2.920	4.630	1.170	1.500	0.000	2.000	1.000	1.000	7.500	13.000	−9.00	0.775
Pt-Ti	6.385	2.771	6.106										

Table 3.4: Angular screening factors of the atomic charge density in Pt_3Ti alloy.

	Pt-Pt-Pt	Pt-Ti-Pt	Ti-Pt-Pt	Ti-Ti-Pt	Ti-Pt-Ti	Ti-Ti-Ti
$C_{\max}$	2.8	2.8	2.8	2.8	2.8	2.8
$C_{\min}$	0.8	0.8	0.8	0.8	0.8	2.0

The parameters of the developed MEAM potential for the Pt-Ti alloy are given in Table 3.3. In Table 3.4, we report the angular screening factors for this potential. The surface energy of pure component metals is an important factor in affecting surface segregation phenomena in binary alloys. Hence, Table 3.5 gives the predicted surface energies of pure Pt and Ti metals using the developed Pt-Ti MEAM potential. Our calculated surface energies for pure hcp Ti metals agree excellently with the published DFT calculation results.[82] Though lower than the DFT results, our calculated surface energies for pure fcc Pt are in quite good agreement with the earlier results from Ref. 44 by Baskes.

Further, we checked the transferability of our developed potential by comparing our MEAM and DFT calculation results for PtTi ($L1_0$, Figure 3.2(b)) and $PtTi_3$ ($L1_2$, Figure 3.2(c), and A15, Figure 3.2(d)) crystals. Table 3.6 shows our results from the MEAM potential calculations, which are in good agreement with those from the DFT calculations. Particularly, both the MEAM and the DFT results point out that $PtTi_3$ crystal would have a lower cohesive energy in an A15 than in an $L1_2$ crystal structure. This prediction is consistent with the experimental observation that A15 is the equilibrium lattice structure for the $PtTi_3$ crystal.[83] Moreover, we used our MEAM potential to calculate the surface segregation energy (in diluted limits, as defined in Ref. 56) of a Pt atom in the hcp Ti (0001) surface and a Ti atom in the fcc Pt (111) surface. We found the surface segregation energy of Pt atom in Ti to be (1.34 eV) compared with (0.72 eV from the DFT calculations[56]) and the Ti atom in Pt to be 1.23 eV (compared with 0.66 eV from the DFT calculations).[56] Despite the noticeable discrepancy in their absolute values, both the MEAM and the DFT methods predicted that Pt would segregate to the close-packed surface of the Pt-Ti alloys. We also calculated the Pt surface segregation energies specifically for Pt_3Ti (111), assuming the direct

Table 3.5: Calculated surface energies of pure Pt (fcc) and pure Ti (hcp) crystals using our developed MEAM potentials. For comparison, we also included the DFT calculation results and experimental data from the literature.

Elements	Surface	MEAM (mJ/m^2)	DFT (mJ/m^2)	Exp. (mJ/m^2)
Pt	(111)	1652	2299	
	(100)	2155	2734	2489
	(110)	1984	2819	2475
Ti	(0001)	2628	2632	1989
	$(10\bar{1}0)_A$	2551	2516	2100
	$(10\bar{1}0)_B$	2791	2754	

and antisite migration routes with the developed MEAM potential. Our MEAM results in Tables 3.1 and 3.2 are in qualitative agreement (having the same positive or negative sign) with those results from our DFT calculations, although the discrepancy in their absolute values are noticeable in some cases. It was found to be very difficult for the MEAM to faithfully reproduce all the data yielded by the DFT calculations. Therefore, our current approach was to make our MEAM potential to best reproduce the DFT energetic data in Table 3.2 for Pt_{Ti} in the first surface layer and Ti_{Pt} in the second surface layer. Both of these two data are negative values and thus related to the most favorable moves occurring in the surface in our subsequent MC simulations.

Table 3.6: Comparison of the calculated properties of Pt_3Ti ($L1_2$, PtTi $L1_0$, and $PtTi_3$ $L1_2$ and A15 bulks using the developed MEAM potential and the DFT method.

	MEAM	DFT
	Properties of Pt_3Ti ($L1_2$)	
Lattice constant a (Å)	3.918	3.956
Heats of formation (eV/atom)	−0.84	−0.835
	Properties of PtTi ($L1_0$)	
Lattice constant a (Å)	3.976	3.990
Lattice constant c (Å)	3.872	3.898
Heats of formation (eV/atom)	−1.089	−0.895
	Properties of $PtTi_3$ ($L1_2$)	
Lattice constant a (Å)	3.996	4.014
Heats of formation (eV/atom)	−0.753	−0.495
	Properties of $PtTi_3$ (A15)	
Lattice constant a (Å)	4.948	5.027
Heats of formation (eV/atom)	−0.795	−0.662

3.4.3 Simulating surface segregation of Pt_3Ti (111)

Pt_3Ti alloy crystal has a rather high order-disorder transition temperature, 1800 K according to experimental measurements.[84] In this work, we chose to study the surface segregation phenomena at 1100 K. Consequently, we needed to ensure that our developed MEAM potentials would predict an ordered phase of Pt_3Ti at 1100 K. To this end, we used the MC simulation method to determine the variation of the Bragg-Williams long-range order (LRO) parameter[85,86] of the Pt_3Ti crystal as a function of temperature. In evaluating the LRO parameter, we divided the $L1_2$ lattice of the Pt_3Ti crystal (Fig. 3.2(a)) into two sublattices: α (three face-center positions) and β (one corner position). The LRO parameter of the Pt_3Ti crystal was calculated using the expression $(P^{\alpha}_{\mathrm{Pt}} - 0.75)/0.25$ Here, P^{α}_{Pt} is the probability for

lattice sites occupied by Pt atoms. Following this definition, LRO is 1.0 for perfectly ordered Pt_3Ti crystal and 0.0 for completely disordered Pt_3Ti crystal. Starting from a perfectly ordered (LRO= 1.0) Pt_3Ti simulation cell (containing 500 atoms), we carried out 10×10^6 MC simulation steps to ensure the full convergence of system energy and we sampled the values of the LRO every 1000 steps in the last 5×10^6 MC simulation steps. In each MC simulation step, we attempted to exchange the positions of two randomly selected Pt and Ti atoms. After the simulation, we calculated the average of all the sampled LRO values.

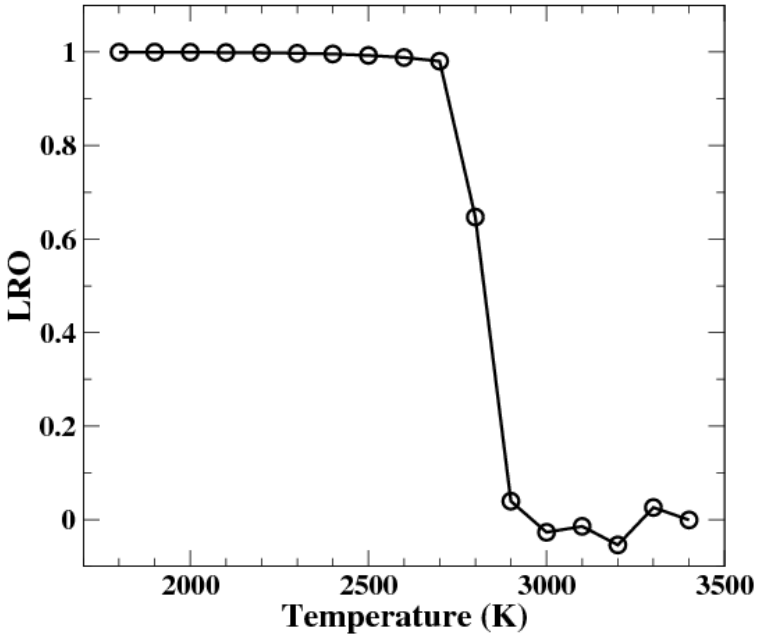

Figure 3.3: Evolution of the LRO of Pt_3Ti crystals as a function of temperature (from 1800 to 3400 K) calculated using the MC simulation and our developed MEAM potentials.

Figure 3.3 plots the results of the calculated LRO parameters for Pt_3Ti crystal in the temperature range of 1800–3400 K. The LRO values were found to be nearly 1.0 (ordered phase) below 2700 K and about 0.0 (disordered phase) above 2900 K using our developed MEAM potentials. Thus, our MC simulation predicted the critical temperature to be about 2800 K for the order-disorder transition of Pt_3Ti crystal. In the experiments, the order-disorder transition temperature of the Pt_3Ti crystal was found to be higher than 1800 K.[84] It should be pointed out that our developed MEAM potentials also significantly overestimated the melting temperature of Pt_3Ti: our theoretical prediction was 3500 K, while the

experimental value was 2224 K.[83] In this work, we were most interested in studying the surface segregation process in ordered Pt_3Ti at 1100 K. To this purpose, our MEAM potential correctly predicted an ordered Pt_3Ti phase ($L1_2$-type) at 1100 K. Hence, the shortcoming of our MEAM potentials in overestimating melting temperature and order-disorder transition temperature does not affect the validity of our results about surface segregation.

To model the surface segregation process using MC simulations, we first constructed a bulk-terminated ordered Pt_3Ti (111) surface slab whose normal direction was [111] and which contained 15 surface layers (32 atoms in each layer). In this stoichiometric surface model, each surface layer had 75 at. % Pt and 25 at. % Ti. Then, we randomly introduced Pt or Ti antisite defects into the surface model so that the overall Pt concentration ranged from 64 to 87 at. %. Starting from these initial structures, we conducted 5×10^6 steps of MC simulations at $T = 1100$ K and sampled the values of the Pt concentrations in the outermost three layers every 1000 steps in the last 3×10^6 MC simulation steps. After the simulation, we calculated the average of all the sampled Pt concentrations.

In Figure 3.4, as a function of the overall Pt concentration in the model, we plotted the calculated Pt concentrations in the first, second, and third layers of thermodynamically equilibrated Pt_3Ti (111) at $T = 1100$ K. Below the stoichiometric ratio of 75 at. % Pt, Ti_{Pt} defects existed in our Pt_3Ti surface slab. It was found for our equilibrated Pt_3Ti (111) surfaces that the outermost layer kept a Pt concentration of 75 at. %, while the Pt concentrations in the second and third layers were lower than 75 at. %. The Pt concentration in the third layer was nearly equal to the overall Pt concentration in our model, but the Pt concentration in the second layer was clearly lower than the overall Pt concentration. At the stoichiometric ratio of 75 at. % Pt, neither kind of antisite defect was present in the model. Our MC simulation found no surface segregation, namely, all the three outermost layers of the Pt_3Ti (111) surface were predicted to have the exact Pt concentration of 75 at. %. Above the stoichiometric ratio of 75 at. %, Pt_{Ti} defects existed in our surface slab model. Our simulation results show that when the overall Pt concentration was slightly over 75 at. % (from 75 to 78.3 at. %), the outermost layer of the Pt_3Ti (111) surface was Pt enriched, while the other (second and third) layers kept their Pt concentrations at 75 at. %. At a critical value of Pt concentration $C_{Pt} = 78.3$ at. % in our case, the annealed

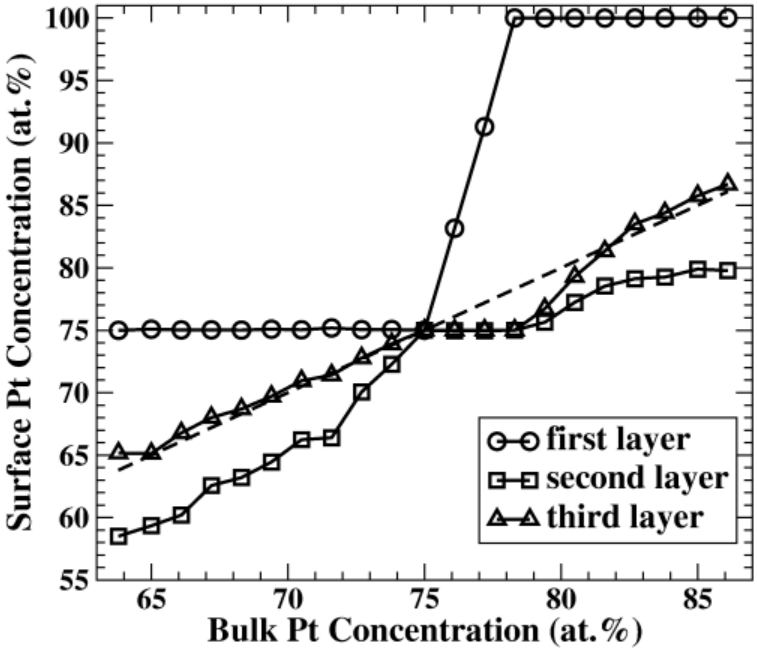

Figure 3.4: Calculated Pt concentrations in the outermost (circles), second (squares), and third layer (up-triangles) of the Pt_3Ti (111) surfaces annealed at $T = 1100$ K using the MC simulation methods and our developed MEAM potentials.

Pt_3Ti (111) surface had a special Pt-segregated structure in which pure Pt was formed in the outermost layer and ordered Pt_3Ti crystal was underneath that layer. Further above that critical concentration, the extra Pt_{Ti} enriched the second and third layers of the surface. It is noticeable in Figure 3.4 that the second surface layer always had lower Pt concentrations than the overall Pt concentrations in the model.

Moreover, our MC simulation predicted that if Pt concentration was slightly higher than 75 at. %, the annealed Pt_3Ti (111) would have a special Pt-segregated structure: pure Pt in the outermost layer and ordered Pt_3Ti crystal underneath. This prediction is in exact agreement with the LEED study.[68] Our slab model for the Pt_3Ti (111) surface has 15 atomic layers (about 32 Å thick) in the (111) direction and two outermost surface layers. Using this model, we predicted that a pure Pt outermost layer would form in Pt_3Ti (111) when the overall Pt concentration was over $C_{Pt} = 78.3$ at. %. Obviously, the value of C_{Pt} depends

on the size of the employed model. If there were 15000 atomic layers (about 3.2 μm thick in our simulation model, the corresponding value of C_{Pt} would be 75.003 at. %, assuming all $\mathrm{Pt_{Ti}}$ atoms migrated to the outermost layers. Thus, a very slight off-stoichiometric effect in the experimental sample of Pt_3Ti (111)-oriented bulk crystal (containing more Pt) could lead to the formation of a pure Pt outermost layer. This explains why the previous experimental study [68] did not link the observed Pt segregation in the Pt_3Ti (111) with the Pt off-stoichiometric effect in the Pt_3Ti crystals. To verify our theoretical predictions presented here, thin films of Pt-Ti alloys (instead of a single crystal surface) with precisely controlled thicknesses and compositions should be used in future experimental measurements.

3.4.4 Electronic structure study of Pt-segregated Pt_3Ti (111)

Our study above indicates that due to Pt antisite migration, the surface-segregated Pt3Ti 111 will have a pure Pt layer in the outermost layer and an L12 crystal structure below if the Pt concentration is slightly higher than 75 at. %. Aiming at understanding how such a surface structure alters the catalytic activity of ORRs on Pt_3Ti (111), we further performed DFT calculations to determine the geometric structure, electronic structure, and O adsorption properties of the Pt-segregated Pt_3Ti (111) surface. We first constructed a five-layer bulk-terminated (111) surface model of Pt_3Ti crystal with a 2×2 unit cell and then replaced the outermost layer with a pure Pt layer. During structure optimization, the bottom two surface layers were fixed to their positions in a perfect Pt_3Ti crystal, and the upper three surface layers were allowed to fully relax. Our DFT calculations predicted that in the relaxed Pt-segregated Pt_3Ti (111) model the separation between the outermost and second surface layer d_{12} would be about 2.30 Å, the separation between the second and third surface layer d_{23} would be about 2.28 Å, the buckling in the outermost layer one Pt atom moves out of the (111) plane formed by the other three Pt atoms would be $b_1 = 0.08$ Å, and the buckling in the subsurface layer where the Ti atom moves out of the (111) plane formed by the other three Pt atoms would be $b_2 = 0.29$ Å. Our theoretical predictions are

in excellent agreement with the experimental measurements[68] ($d_{12} = 2.23$ Å, $d_{23} = 2.21$ Å, $b_1 = 0.04$ Å), and $b_2 = 0.15$ Å. Hence, our modeled Pt-segregated Pt_3Ti (111) is reasonably close to the real experimental sample.

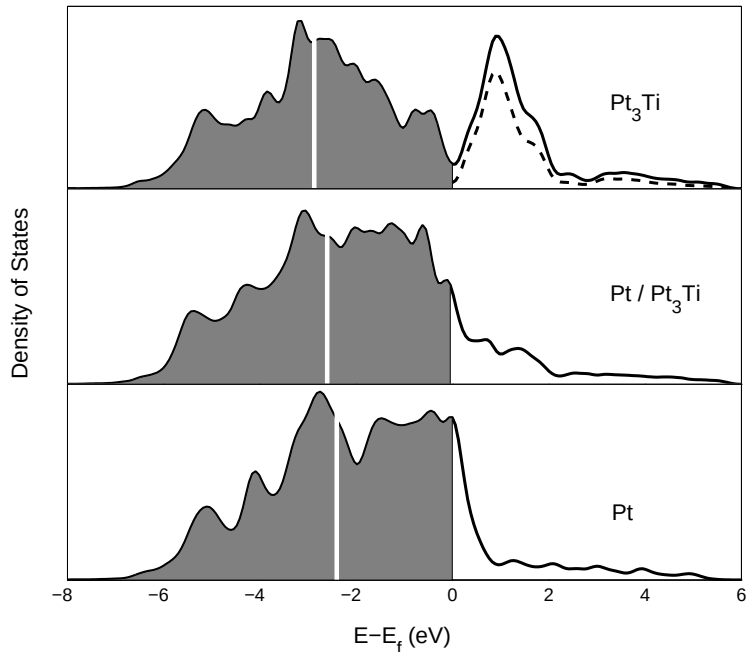

Figure 3.5: Calculated DOS of the surface d-electrons of (a) bulk-terminated Pt_3Ti (111) , (b) Pt-segregated Pt_3Ti (111) , and (c) pure Pt (111) using the DFT method.

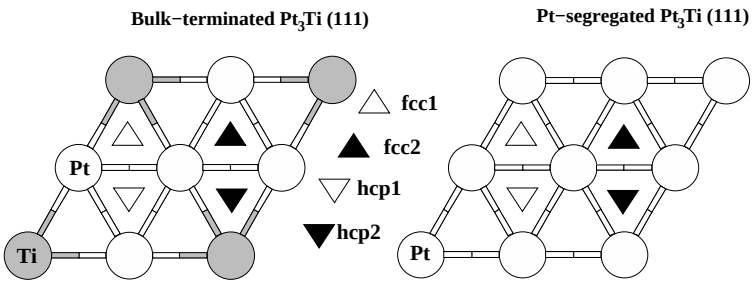

Figure 3.6: Schematics of various sites for O adsorption on the bulk-terminated and Pt-segregated Pt_3Ti (111) surfaces.

It has been established by Hammer and Nørskov that the d-band center of the surface with respect to the Fermi level is a useful indicator to measure the chemical reactivity of

Table 3.7: Calculated locations of the d-band center of the three modeled (111) surfaces and O adsorption energies E_O at various atomic sites see Fig. 3.6 on the three modeled (111) surfaces.

		E_O (eV)			
	d-band center (eV)	fcc1	fcc2	hcp1	hcp2
Pt (111)	−2.41	−4.26	–	–	–
Bulk-terminated Pt_3Ti (111)	−2.87	−5.56	−3.08	−3.31	−5.44
Pt-segregated Pt_3Ti (111)	−2.62	−4.10	−3.37	−3.57	−3.64

transition metal catalysts.54 For the cathode electrocatalysts of proton exchange membrane fuel cells, some downshift of the d-band center with respect to the one of pure Pt was theoretically predicted and later experimentally confirmed to enhance the reaction activity of the oxygen reduction reaction.[9,26] The d-band center refers to the center of the density of states DOS of d-electrons with reference to the Fermi energy in the outermost surface layer of the catalyst. This can be determined from the projected DOS of the surface atoms by calculating the first-moment of the occupied states of the d-electrons. We plotted the calculated d-electron DOS and pointed out the location of the d-band centers of bulk-terminated Pt_3Ti (111) in Fig. 3.5(a) , Pt-segregated Pt_3Ti (111) in Fig. 3.5(b) , and pure Pt (111) in Fig. 3.5(c) . The values of the d-band centers of the three surfaces are given in Table 3.7. Compared to the d-band center of pure Pt (111) , the d-band center of Pt-segregated Pt_3Ti (111) downshifts by 0.21 eV, and the d-band center of bulk-terminated Pt_3Ti (111) downshifts by 0.46 eV. With ultraviolet photoemission spectroscopy, Mun et al. had observed a downshift in the d-band center of about 0.8 eV when comparing annealed Pt_3Ti and Pt polycrystal surfaces.[63] It appears that our model calculation in this work is in qualitative agreement only with that experimental measurement.

Furthermore, we evaluated the adsorption energies of O atoms on the bulk-terminated Pt_3Ti (111) , Pt-segregated Pt_3Ti (111) , and pure Pt (111). In the pure Pt (111) surface, the fcc site above a threefold position in which there is no atom in the subsurface was the

lowest-energy location for O to adsorb on the surface. However, there were two types of fcc sites and two types of hcp sites above a threefold position in which there was an atom in the subsurface as shown in Fig. 3.6 on bulk-terminated and Pt-segregated Pt_3Ti (111) surfaces. Table 3.7 also gives our calculated O adsorption energies on the three modeled surfaces using DFT method. The adsorption energy is calculated as the energy difference between the adsorption and isolated configurations of O and the surface. The more negative the adsorption energy, the more strongly the O adsorbs on the surface. Our results for bulk-terminated Pt_3Ti (111) indicate that O will be adsorbed on the surface more strongly at fcc1 and hcp2 sites where a Ti atom is nearby than at fcc2 and hcp1 sites where only Pt atoms are nearby . Moreover, our results show that O will adsorb more weakly on Pt-segregated Pt_3Ti (111), at least by 0.16 eV, than on pure Pt (111) . Based on previous experimental data and theoretical model,[8] slightly weakened O adsorption on a Pt-segregated Pt_3Ti 111 surface is likely to be the reason for the observed catalytic activity enhancement for the ORR on carbon-supported $Pt_{75}Ti_{25}$ nanoparticles.[66,67]

3.5 CONCLUSION

In this work, we have studied surface segregation phenomena in the (111) surface of ordered Pt_3Ti crystal using accurate DFT calculations with no configuration sampling and the MEAM potential-based MC simulations with extensive configuration sampling. Our DFT results for stoichiometric ordered Pt_3Ti crystal show that it requires at least 0.68 eV to directly exchange the surface Ti atoms with the Pt atoms inside the crystal. Consequently, it is hardly possible for Pt to segregate to the outermost surface layer through this direct exchange route. In addition, we examined the influence of the off-stoichiometric effect on surface segregation in Pt_3Ti crystal using DFT calculations. In particular, we compared the generation energies of antisite defects in the surface and bulk regions of Pt_3Ti (111). Our DFT results in Table 3.2 reveal that if there is more Pt in the Pt_3Ti crystal than the stoichiometric value (75 at. %), those excessive Pt_{Ti} atoms will migrate to the outermost layer of (111) surface. In contrast, if there is more Ti in the Pt_3Ti crystal than the stoichio-

metric value (25 at. %), those excessive Ti_{Pt} atoms will migrate to the second layer of the (111) surface. Thus, our DFT study implies that the migration of Pt_{Ti} defects may cause Pt surface segregation in the outermost layer of Pt_3Ti (111).

In order to further elaborate surface segregation in Pt_3Ti (111) at the experimental annealing temperature, we simulated the surface segregation process at $T = 1100$ K using the MC simulation method and our developed MEAM potentials. Our developed MEAM potentials are capable of correctly predicting the surface energies of pure Pt and Ti crystals, the structural and energetic properties of bulk Pt_3Ti ($L1_2$), PtTi ($L1_0$), $PtTi_3$ ($L1_2$), and $PtTi_3$ (A15), and the surface segregation energies. Our MEAM potentials (in Table 3.2) also suggest that if there is more Pt in the Pt_3Ti crystal than the stoichiometric value (75 at. %), those excessive Pt_{Ti} atoms will migrate to the outermost layer of the (111) surface. Our MC simulation results in Figure 3.4 clearly show that a strong segregation of Pt to the outermost layer will occur in the Pt_3Ti (111) surfaces whose overall Pt concentration is above 75 at. %. When the bulk Pt concentration was 78.3 at. % in our surface slab model, the Pt-segregated Pt_3Ti (111) surface had such a structure: the outermost layer was pure Pt and the second and below layers were ordered Pt_3Ti (111) surface layers. This theoretical prediction agrees very well with the experimental measurement.[68]

Furthermore, we evaluated the geometric and electronic structures of the Pt-segregated Pt_3Ti (111) surface using DFT method. Our predicted structural parameters of the Pt-segregated Pt_3Ti 111 surface are very close to the corresponding data extracted from LEED measurements.[68] We also found that the d-band center of the Pt-segregated Pt_3Ti (111) surface will downshift when compared with the one of pure Pt (111). This theoretical prediction is in qualitative agreement with experimental measurements.[63] More importantly, we predicted that O adsorption is slightly weaker on the Pt-segregated Pt_3Ti (111) surface than on the pure (111). We believe this slightly weakened O adsorption could lead to the observed catalytic activity enhancement for ORRs on carbon-supported $Pt_{75}Ti_{25}$ nanoparticles.[66]

Through our theoretical investigations in this work, we have gained much insight into the surface segregation phenomena in the (111) surface of ordered Pt_3Ti crystal. The attained knowledge will be useful for designing and fabricating Pt-Ti alloys as high performance catalysts, especially for their application as electrocatalysts in fuel cells.

4.0 MONTE CARLO SIMULATION OF SURFACE SEGREGATION PHENOMENA IN EXTENDED AND NANOPARTICLE SURFACES OF PLATINUM–PALLADIUM ALLOYS

4.1 ABSTRACT

The surface segregation phenomena in the extended and nanoparticle surfaces of Pt-Pd alloys have been studied using the Monte Carlo (MC) simulation method and the modied embedded-atom method (MEAM) potentials developed for Pt-Pd alloys. The MEAM potentials were tted to reproduce the experimental values of the lattice parameters, cohesive energies and surface energies of pure Pt and Pd metals, as well as the density functional theory calculation results of the lattice parameters and heat of formation of $L1_2$ Pt_3Pd, $L1_0$ PtPd and $L1_2$ $PtPd_3$ crystal. Using the MC method and the developed MEAM potentials, we calculated the Pt concentrations in the outermost three layers of the equilibrium (111), (100) and (110) extended surfaces as well as the outermost surfaces of the equilibrium cubo-octahedral nanoparticles of Pt-Pd alloys. Our simulation results showed that the Pd atoms would segregate into the outermost layers of the extended surfaces and the Pt concentration would increase monotonically from the extended surfaces into the bulk. The equilibrium Pt-Pd nanoparticles were found to have Pd-enriched shells and Pt-enriched cores. In the shell of the Pt-Pd nanoparticles, the Pd atoms were predicted to preferably segregate to the (100) facets rather than the (111) facets.

4.2 INTRODUCTION

Surface segregation refers to the phenomenon in which the surface composition of alloy materials differs from their bulk composition at thermodynamic equilibrium conditions.[50,51] The surface segregation process could affect many important physical and chemical properties (such as adsorption, wetting, oxidation, thermionic emission, corrosion, electrical contact, friction and wear, crystal growth and catalysis) of alloy materials.[49] In particular, the surface region is the active part of alloy catalysts in promoting various chemical reactions. Consequently, we can take advantage of the surface segregation process to optimize the performance of the alloy catalysts. For example, it was predicted that, due to the surface segregation process, there would be 100% Pt in the outermost layer but only 50% Pt (50% Ni) in the sub-surface layer of the annealed (111) surface of the $Pt_{75}Ni_{25}$ alloy.[57] Density functional theory (DFT) calculations further revealed that in such a segregated surface structure the Ni atoms beneath the Pt monolayer could shift the d-electron band of the surface Pt downwards relative to that of pure Pt.[15] Experimental measurements found out that the annealed (111)-oriented $Pt_{75}Ni_{25}$ alloy with Pt segregated surfaces would have signicantly enhanced catalytic activity for oxygen reduction reactions than pure Pt, although the content of precious Pt had been reduced by 25 at.%.[12] Therefore, it is very helpful in designing novel alloy catalysts to know what chemical component would segregate to the surface layers as well as to what extent the surface segregation could be.

Bimetallic Pt-Pd nanoclusters have been extensively studied due to their catalytic applications in promoting oxygen reduction reaction[87], methanol decomposition[88] and hydrogenation of aromatics[89]. Thus, it is of great interest to gain knowledge of the structural arrangement of the Pt and Pd atoms in the surface of the Pt-Pd alloy catalysts. Both experimental measurements and Monte Carlo simulations had indicated that the Pd atoms would favor segregating to the outermost surface layer of the Pt-Pd nanoclusters[90,91]. As summarized in[60], there are three major physical mechanisms causing surface segregation phenomena in disordered binary alloys (or binary solid solutions): (1) if the heat of the solution is quite negative, the majority component of the alloy will enrich the surface to maximize the mixing of the two components in the bulk; (2) when the atomic sizes of the

two components are dramatically different, the larger component will segregate to the surface to reduce strain energy in the alloys; and (3) the component (in its pure element form) with a lower surface energy will segregate to the alloy surface. Hence, the surface segregation process in disordered alloys is always exothermic and accompanies a decrease in system congurational entropy. For Pt-Pd alloys, mechanisms (1) and (2) for surface segregation can be neglected because the heat of solution of Pt-Pd alloys is quite small as well as the Pt and Pd atoms having very similar sizes. Insomuch, surface energy difference (pure Pd has lower surface energy than Pt) is the main driving force of segregating Pd to the surfaces.

To gain knowledge on surface composition profiles, the surface segregation process in Pt-Pd alloys has been simulated at the atomistic scale using various different atomic interaction potentials such as effective medium theory[92], analytic modified embedded-atom method potential[93], Gupta potential[94], bond order simulation model[95] and Sutton-Chen potential[96]. Although these potentials yielded the predictions (segregation of Pd to the surface) qualitatively agreeing with experiments, few of them were thoroughly evaluated in order to quantitatively simulate the surface segregation extent in the different surfaces of the Pt-Pd alloys. In this work, we have developed the parameters of the modified embedded-atom method (MEAM) potentials for the Pt-Pd alloys and particularly examined the capability of the developed MEAM potentials in predicting the surface segregation composition profiles in the low-index extended surfaces [(111), (100) and (110)] and the cubo-octahedral nanoparticle surfaces of the Pt-Pd alloys.

Moreover, the development of novel catalysts has more and more focused on controlling the surface composition and geometric structures of multi-component (beyond binary) alloy nanostructures.[13,97,98] As a result, it is desired to construct a set of consistent atomic interaction potentials which have a similar formula and hence could be directly combined to simulate the surface segregation process in complex multi-component alloy nanostructures. We chose MEAM as the theoretical model for our alloy potentials in this work. This is because MEAM has included many-body effects, angular-dependent terms and even the second-nearest neighbor contribution in its formula and thus is capable of describing the atomic interaction for transition metals in many types of crystals (for example, face-centered cubic (fcc), body-centered cubic (bcc) and hexagonal close-packed (hcp) crystal

lattice)[44,45,99]. In our previous work, we have demonstrated that the MEAM potentials could be employed to accurately model the surface segregation phenomena in Pt-Re[58], Pt-Ni[57], Pt-Mo[59] and Pt-Ti[100] binary alloys. Therefore, in this work, we added a well-tested Pt-Pd atomic interaction potential into the library of the MEAM potentials particularly developed for accurate simulation of surface segregation in transition metal alloys.

Table 4.1: Parameters of the MEAM potentials for the Pt-Pd alloys.

	E_c	r_e	α	A	$\beta^{(0)}$	$\beta^{(1)}$	$\beta^{(2)}$	$\beta^{(3)}$	$t^{(0)}$	$t^{(1)}$	$t^{(2)}$	$t^{(3)}$	ρ^0
Pt	5.77	2.772	6.44	1.04	4.67	2.2	6.0	2.2	1.0	4.7	−1.38	3.29	1.1
Pd	3.910	2.751	6.432	1.010	4.975	2.200	6.000	2.200	1.000	5.023	1.383	4.484	0.99
Pt-Pd	5.332	2.764	6.800										

Table 4.2: Angular screening factors of the atomic charge density in Pt-Pd alloys.

	Pt-Pt-Pt	Pt-Pd-Pt	Pd-Pt-Pt	Pd-Pd-Pt	Pd-Pt-Pd	Pd-Pd-Pd
$C_{\max}$	2.8	2.8	2.8	2.8	2.8	2.8
$C_{\min}$	0.8	0.8	0.8	0.8	0.8	2.0

4.3 DEVELOP MEAM POTENTIALS FOR PT-PD ALLOYS

In this work, the employed MEAM potentials for pure Pt and Pd metals were similar to those published in Ref. 44, with some renormalized scaling factors in the atomic charge densities. We mainly developed the cross-potential between Pt and Pd in the alloy systems based on our density functional theory (DFT) results. We gave the parameters for the Pt-Pd MEAM potentials in Table 4.1 and the angular screening parameters[47] for the potentials in Table 4.2.

Among all the material properties, the size of the Pt and Pd atoms, the surface energies of the Pt and Pd crystal, and the heat of solution of the Pt-Pd solid solutions are most relevant to the surface segregation process in the Pt-Pd alloys[60]. In this work, the lattice parameters were exactly reproduced to be the experimental values of 3.92 Å for fcc Pt and 3.89 Å for fcc Pd by the developed MEAM potentials. In Table 4.3, we reported the calculated surface energies with the developed MEAM potentials for the three low-index surfaces [(111), (100) and (110)] of the pure Pt and Pd fcc crystals. It is noticeable that the calculated surface energies with our MEAM potentials were about 600 mJ/m^2 lower than the previous results from DFT calculations[82] for the same surfaces and from experimental measurements[101,102] for polycrystalline surfaces. It has been recognized that it is a shortcoming of most atomic potential models in predicting lower surface energies than experimental results[44,45]. However, it is also worth mentioning that the experimentally measured surface energy is the average value of various surfaces (including high-index, high-energy surfaces). This may partially explain the discrepancy in surface energy between the

Table 4.3: Calculated surface energies of pure Pt (fcc) and pure Pd (fcc) crystals using our developed MEAM potentials. For comparison, we also included the DFT calculation results and experimental data from the literature.

Elements	Surface	MEAM (mJ/m^2)	DFT (mJ/m^2)	Exp. (mJ/m^2)
Pt	(111)	1652	2299	
	(100)	2155	2734	2489
	(110)	1984	2819	2475
Pd	(111)	1383	1920	2003
	(100)	1654	2326	2050
	(110)	1614	2225	

prediction of atomic potential models and experimental data. Shown in Table 4.3, both DFT and MEAM predicted that single-crystal Pd would have a lower surface energy in all the three low-index surfaces than single-crystal Pt. Therefore, the two theoretical approaches agree on the point that the difference in surface energy between the Pt and Pd crystals could drive the Pd atoms to segregate to the surface of the Pt-Pd alloys.

Furthermore, we fitted the MEAM cross-potentials between Pt and Pd with the first-principles DFT calculation results about the lattice parameter and heat of formation of Pt_3Pd crystal (with an $L1_2$ crystal structure), PtPd crystal (with an $L1_0$ crystal structure) and $PtPd_3$ crystal (with an $L1_2$ crystal structure). The heat of formation (in units of eV/atom) of the Pt-Pd crystals was computed as the energy of the intermetallic crystals relative to those of the equilibrium fcc Pt and fcc Pd. Table 4.4 compares the properties of the three Pt-Pd intermetallic crystals calculated with our MEAM potentials and DFT methods, showing that the developed MEAM potentials closely reproduce the DFT results. Moreover, our MEAM potentials as well as DFT calculations predicted the negative but fairly small heats of formation for all three Pt-Pd crystals. This implies that the Pt and Pd atoms would not have a pronounced mixing tendency in their solid solutions.

Table 4.4: Comparison of the calculated properties of bulk Pd_3Pd ($L1_2$), PtPd ($L1_0$) and $PtPd_3$ ($L1_2$) crystals using the MEAM potentials and the DFT methods.

	MEAM	GGA-DFT
	Properties of Pt_3Pd ($L1_2$)	
Lattice constant a (Å)	3.909	3.975
Heats of formation (eV/atom)	−0.027	−0.022
	Properties of PtPd ($L1_0$)	
Lattice constant a (Å)	3.900	3.964
Lattice constant c (Å)	3.903	3.966
Heats of formation (eV/atom)	−0.034	−0.027
	Properties of $PtPd_3$ ($L1_2$)	
Lattice constant a (Å)	3.895	3.963
Heats of formation (eV/atom)	−0.025	−0.019

Table 4.5: Calculated surface segregation energies (in eV) for a Pt (or Pd) impurity in the three low-index Pd (or Pt) extended surfaces. For comparison, we also include the previous calculation results from effective medium theory (EMT) and first-principles linear-muffin-tin-orbital (LMTO) methods.

	Surfaces	MEAM	EMT	LMTO	LMTO
Pt impurity in	Pd (111)	0.13	0.07	0.24	0.19
	Pd (100)	0.25	0.10	0.36	
	Pd (110)	0.32	0.14	0.42	
Pd impurity in	Pt (111)	0.00	−0.03	0.08	0.00
	Pt (100)	−0.14	−0.06	−0.12	
	Pt (110)	−0.12	−0.09	−0.06	

As discussed above, our developed MEAM potentials for the Pt-Pd alloy are capable of accurately describing the atomic size effect, surface energy effect and heat of solution effect which are the major factors in determining the surface segregation process in the alloy. Besides these quantities, we can estimate the segregating tendency of the Pt and Pd atoms to the alloy surfaces by calculating their surface segregation energy in the dilute limit. As suggested in Ref.[56], the surface segregation energy in extended surfaces is defined as the energy difference between the total energy of the systems with a substitutional impurity atom in the outermost surface layer and in the bulk. In Table 4.5, we gave the calculated surface segregation energies for a Pt atom in the (111), (110) and (100) surfaces of Pd crystals and a Pd atom in the (111), (110) and (100) surfaces of Pt crystals using the MEAM potentials. As shown in Table 4.5, the predicted surface segregation energies with our MEAM potentials are in very good quantitative agreement with the previous LMTO-DFT calculation results. Both the LMTO-DFT and MEAM methods agree in that the Pt atoms would not prefer segregating to the surfaces of the Pd single crystal while the Pd atoms would segregate to the surfaces of the Pt single crystals. It should also be noted that both the LMTO-DFT and our MEAM methods predicted that the surface segregation energies of the Pd impurity in the Pt surfaces will decrease following the order of (111), (110) and (100).

Using the developed MEAM potentials and the MC simulation method, we simulated the surface segregation process in the three low-index surfaces of the Pt-Pd alloys. In this work, we set the MC simulation temperature at 1200 K to be consistent with the annealing temperature in experimental measurements[103,104]. First, we performed the MC simulations for the three-dimensional periodic cubic simulation cells containing in total 500 randomly distributed Pt and Pd atoms at 1200 K to find the lattice constants for the Pr-Pd bulk alloys. The whole MC simulation took 2×10^6 MC steps. We only averaged the pressure of the simulation cells in the last 1×10^6 MC steps to eliminate the influence from the original structure. Thus, the lattice constant of the Pt-Pd alloys with a given bulk Pt concentration was determined from the dimensions of the simulation cell that led to zero average pressure from the MC simulations. Figure 4.1 plots the calculated equilibrium lattice constants at

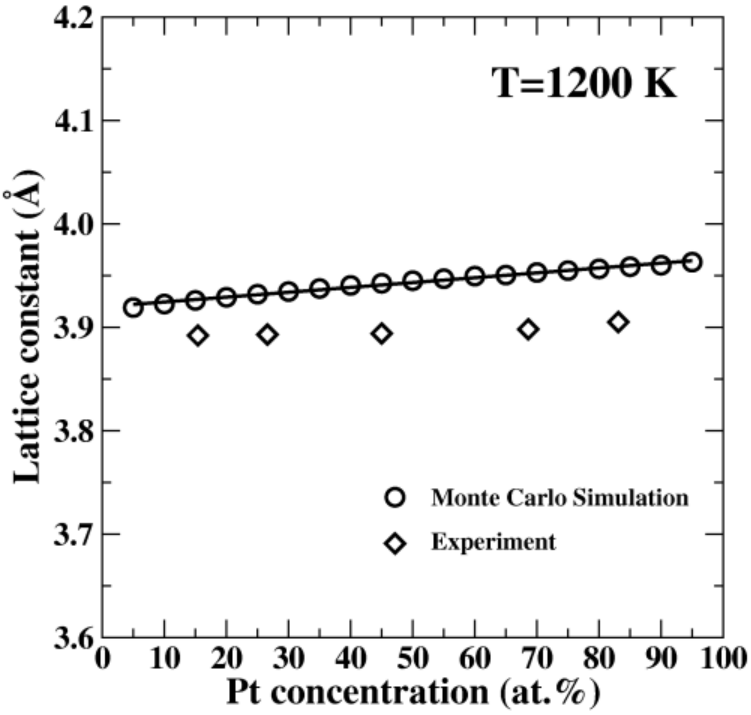

Figure 4.1: Calculated lattice constants of disordered Pt-Pd bulk alloys using the developed MEAM potentials and the MC simulation method at a temperature of 1200 K.

1200 K, displaying a linear relation between the lattice constant and the Pt concentration of the Pt-Pd alloys. Our theoretical predictions of the lattice constants of the Pt-Pd alloys were found to be within 1.5 % deviation from the experimental data.[105]

Furthermore, we carried out the MC simulations to quantitatively predict the Pt concentrations in the outermost three surface layers of the (111), (100) and (110) surface of the Pt-Pd alloys. We modeled these three low-index extended surfaces using surface slab cells, which have periodic boundaries in the two directions parallel to the surface and a free boundary in the direction normal to the surface. Hence, there are two surfaces in each slab simulation cell. The dimensions of these surface slab cells were determined from the lattice constants (in Figure 4.1) of the bulk Pt-Pd alloy with the same composition. For the (111) surface, the simulation cells have 15 surface layers and 48 atoms in each layer; for the (100) surface, the simulation cells have 17 surface layers and 50 atoms in each layer; and for the

(110) surface, the simulation cells have 23 surface layers and 48 atoms at each layer. Thus, the modeled surface slabs were about 30 Å thick for all three low-index extended surfaces of the Pt-Pd alloys.

Starting from the initial surface structures with randomly distributed Pt and Pd atoms, the MC simulations could generate the thermodynamically equilibrium surface structures at $T = 1200$ K after millions of MC steps. In the MC simulations, we included both the compositional relaxation and structural relaxation of the extended surfaces, conducted 10×10^6 MC steps in total, and sampled the composition profile every 1000 steps in the last 5×10^6 MC steps. Due to surface segregation and the finite size of our simulation cells, the composition at the center of the simulation cell will deviate from the assumed bulk composition at the equilibrium stage of our MC simulations. To rectify this error, we have done a series of MC simulations for each extended surface with various overall compositions to re-establish the bulk composition at the center of the simulation cells.

We plotted the variation of the calculated Pt concentrations at the outermost three surface layers as a function of the Pt bulk concentration in Figure 4.2 for the (111), (100) and (110) surfaces of the Pt_xPd_{100-x} alloys. Here, x varies from 5 to 95 with a separation of 5. Our results from the MC simulations revealed that Pd would enrich the outermost layer of all three low-index surfaces for all compositions of the Pt-Pd alloys. This result is consistent with the simple thermodynamic model prediction[60], previous atomistic modeling results[92–96] and experimental observations.[103,104] Further analysis on the equilibrium structures from the MC simulations revealed that the (110) surface would tend to reconstruct at the high Pt concentration regime of the Pt-Pd alloys if the atoms were allowed to relax to the lowest-energy configurations. The surface reconstruction phenomena in the (110) surface of the $Pt_{94}Pd_6$ alloys had been observed in experiments.[104] Hence, our MC simulations suggested that the surface reconstruction might cause Pt to slightly enrich the second sub-surface layer of the (110) surface of the Pt-Pd alloys.

Moreover, our results in Figure 4.2 pointed out that the surface Pt concentrations would be the lowest at the outermost layer and gradually increase deep into the bulk region. At the third sub-layer of the surfaces, the surface Pt concentrations are nearly equal to the bulk Pt concentrations of the Pt_xPd_{100-x} alloys. Such a monotonically increasing segregation profile

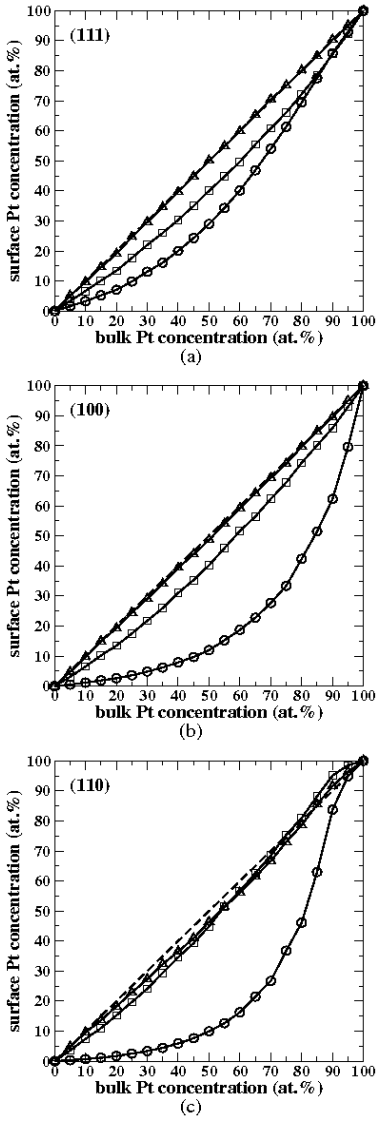

Figure 4.2: Predicted equilibrium surface Pt concentrations in the outermost three layers of the (a) (111), (b) (100) and (c) (110) surfaces of disordered Pt-Pd alloys using the developed MEAM potentials and the MC simulation method at temperature of 1200 K.

of the surface Pt concentrations had also been found in previous simulation work using the adapted EMT potentials for the Pt-Pd alloy[92]. Furthermore, our MC simulation results in Figure 4.2 showed that the extent of the Pd segregation to the outermost layer of the extended surfaces generally followed the sequence of (110), (100) and (111): the strongest segregation to the (110) surface and the weakest segregation to the (111) surface. For example, the Pt surface concentrations in the outermost layer of the $Pt_{50}Pd_{50}$ alloy were found to be 9.9 at. % in the (110) surface, 11.8 at. % in the (100) surface and 29.0 at. % in the (111) surface from our MC simulations. Our theoretical result about the sequence of segregation extent in different extended surfaces agrees with that from experimental measurements.[103,104]

The Pt surface concentrations were measured in Ref. 90 to be about 50 at. % and 5 at. % in the $Pt_{80}Pd_{20}$ and $Pt_{20}Pd_{80}$ polycrystalline surfaces annealed at 800 $^{\circ}C$ under ultrahigh vacuum, respectively. In comparison, our calculated Pt surface concentrations in this work were 69.4 at. % in the (111) surface (Figure 4.2(a)), 41.7 at. % in the (100) surface (Figure 4.2(b)) and 46.1 at. % in the (110) surface (Figure 4.2(c)) of the $Pt_{80}Pd_{20}$ alloy; and 7.1 at. % in the (111) surface (Figure 4.2(a)), 2.5 at. % in the (100) surface (Figure 4.2(b)) and 1.7 at. % in the (110) surface (Figure 4.2(c)) of the $Pt_{20}Pd_{80}$ alloy. Simply averaging the values in the three surfaces, we obtained the Pt surface concentration of 52.4 at. % and 3.8 at. % in the outermost surface layer of the $Pt_{80}Pd_{20}$ and $Pt_{20}Pd_{80}$ polycrystalline surfaces annealed at 1200 K, respectively. Thus, our theoretical predictions based on the MC simulations with the developed MEAM potentials are in excellent agreement with the data obtained from the low-energy ion scattering technique.[90]

4.4 SIMULATE SURFACE SEGREGATION IN THE NANOPARTICLE SURFACES OF PT-PD ALLOYS

Surface segregation phenomena in nanoparticle surfaces could be quite different from those in extended surfaces. In the extended surface, there are sufficient segregated species in the system so that the composition of the interior regions would not be altered by the surface segregation process. However, the number of atoms in a nanoparticle is normally

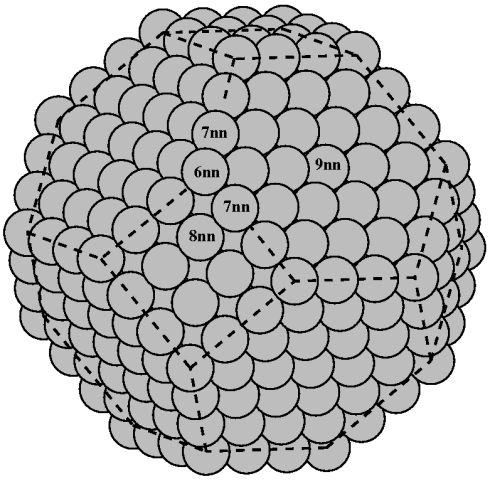

Figure 4.3: An fcc cubo-octahedral nanoparticle.

limited. Consequently, the segregation of some species to the nanoparticle surface would appreciably change the chemical compositions both in the surface and in the interior region of the nanoparticle. Moreover, all the surface atoms in the three extended low-index surfaces [(111), (100) and (110)] are equivalent. In contrast, the surface atoms in the nanoparticle surface have different numbers of nearest neighbors as shown in Figure 4.3 for an fcc cubo-octahedral nanoparticle. This inhomogeneity could cause preferable segregation phenomena (segregated species would be more likely ro occupy some sites than others) in the outermost surface of the nanoparticles.

Studying the surface segregation phenomena in the nanoparticle surfaces of Pt-Pd alloys, we have performed the MC simulations to obtain the equilibrium Pt concentrations in the surface of cubo-octahedral $Pt_{25}Pd_{75}$, $Pt_{50}Pd_{50}$ and $Pt_{75}Pd_{25}$ nanoparticles. Figure 4.3 shows the atomistic structure of a cubo-octahedral nanoparticle constructed from fcc bulk crystals. In this work, we modeled four different sized cubo-octahedral nanoparticles which contain 586, 1289, 2406 and 4033 atoms and correspondingly have a diameter of 2.6 nm, 3.5 nm, 4.4 nm and 5.3 nm, respectively. We distributed randomly the Pt and Pd atoms in the initial structure of the nanoparticles and then drove these nanoparticles to their thermodynamic equilibrium configurations by carrying out 20×10^6 steps of MC simulations at temperatures

of $T = 600$ K. It notes that 600 K is close to the employed reduction temperature in the alloy particle fabrication process.[88] Hence, our simulation results at $T = 600$ K would generate the representative structures of the equilibrium Pt-Pd nanoparticles comparable to experimental samples. For the equilibrium nanoparticles, we sampled the Pt concentrations in the surface, core and different surface sites every 1000 steps in the last 10×10^6 MC steps.

In Figure 4.4, we showed snapshots of the equilibrium Pt-Pd nanoparticles attained from our MC simulations. It can be seen in these figures that the equilibrium nanoparticles have rounded up around their vertices and have more Pd atoms in their outermost surface than their overall composition. In addition, the Pt atoms (gray circles) mostly appear at the (111) facets in the equilibrium nanoparticle surfaces. Quantifying these observations, we plotted in Figure 4.5 the variation of the calculated average Pt concentrations at the shell (outermost surface layer), core (interior region beneath the shell), (111) facets and (100) facets of the equilibrium Pt-Pd nanoparticles as a function of the diameter of the nanoparticles.

Our results in Figures 4.5(a), (c) and (e) indicated that, as compared to the overall composition of the nanoparticles, the Pt concentrations in the shell were about 15–20 at. % lower while the Pt concentration in the core region were about 10–30 at. % higher. Hence, we predicted that the equilibrium Pt-Pd nanoparticle would have a Pd-enriched shell and a Pt-enriched core. Our results in Figures 4.5(b), (d) and (f) showed that the Pt concentrations were not equal at the (111) and (100) facets of the equilibrium Pt-Pd nanoparticle surface. For all the simulated Pt-Pd nanoparticles, the Pt concentrations at the (111) facets were found to be much higher than those at the (100) facets. It was inferred that the Pd atoms would prefer segregating to the (100) facets than the (111) facets in the shell of the Pt-Pd nanoparticles. This is consistent with the results in Table 4.5 and Figure 4.2 that the extent of Pd segregation to the (100) extended surface would be much stronger than that to the (111) extended surface.

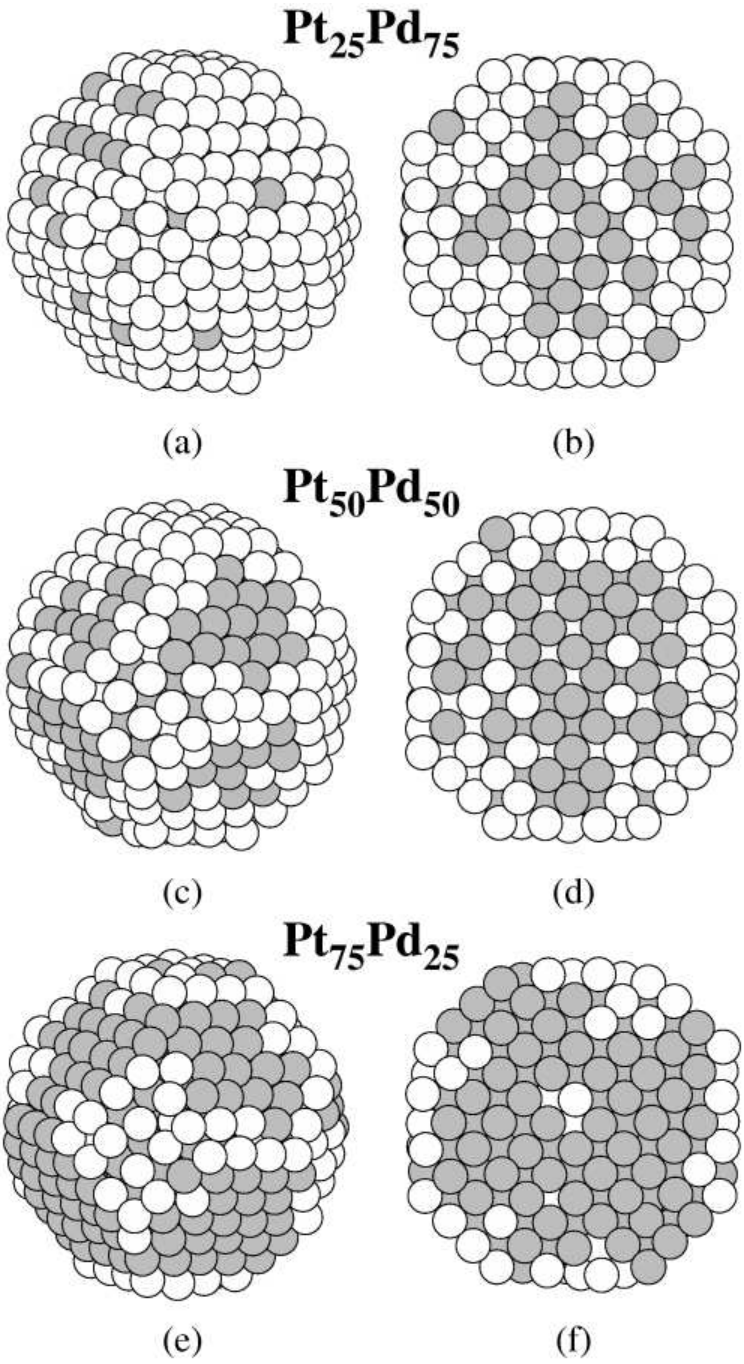

Figure 4.4: Snapshots of equilibrium cubo-octahedral nanoparticles (containing 586 atoms) of Pt-Pd alloys from the MC simulations at $T = 600$ K.

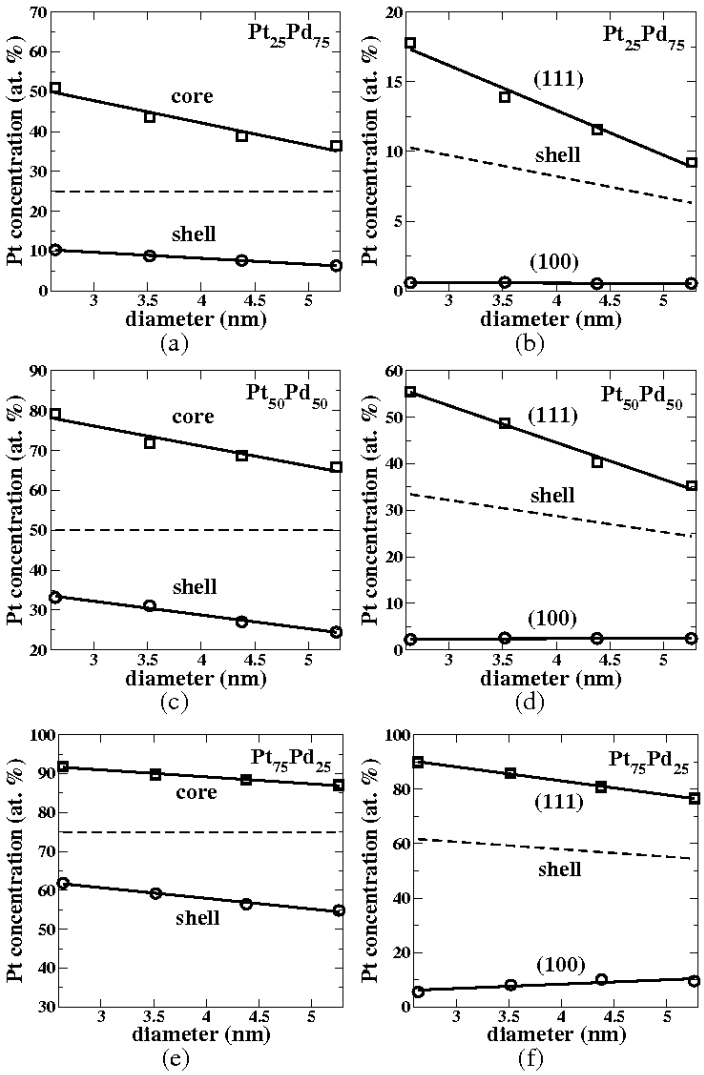

Figure 4.5: Predicted equilibrium surface Pt concentrations in the cubo-octahedral nanoparticles of (a)-(b) $Pt_{25}Pd_{75}$, (c)-(d) $Pt_{50}Pd_{50}$ and (e)-(f) $Pt_{75}Pd_{25}$ alloys using the developed MEAM potentials and the MC simulation method at temperature of 600 K.

Our results in Figure 4.5 also revealed that the size of nanoparticles affected the surface segregation phenomena in the Pt-Pd nanoparticles. It was noticed in Figures 4.5(a), (c) and (e) that the extent of Pd segregation to the nanoparticle surface increased with the increase of nanoparticle diameter (in the range from 2 to 6 nm), implying that the Pd surface segregation was suppressed in the small Pt-Pd nanoparticles. Moreover, we observed in Figures 4.5(b), (d) and (f) that the Pt concentration at the (100) facets was very low and did not vary much with the nanoparticle size. In contrast, the Pt concentration at the (111) facets of the nanoparticles would change dramatically with nanoparticle size. More interestingly, our MC simulations predicted that the Pt concentrations at the (111) facets were higher than the overall Pt concentration in the $Pt_{50}Pd_{50}$ nanoparticle containing 586 atoms and the four $Pt_{75}Pd_{25}$ nanoparticles in this study although the Pt concentrations at the shell were lower than the overall Pt concentration of these nanoparticles. Pt has better catalytic activity than Pd for many applications. Therefore the Pt-enriched (111) facets in the Pt-Pd nanoparticles are desired in catalyst design.

4.5 CONCLUSION

In this work, we have first developed a set of parameters within the MEAM framework for Pt-Pd alloys based on experiment data and first-principles calculation results. Furthermore, we used our developed MEAM potentials and the MC simulation method to investigate the surface segregation phenomena in the extended and nanoparticle surfaces of Pt-Pd alloys. Our MC simulation results (in Figure 4.2) indicated that the Pd atoms would always segregate to, and hence enrich, the outermost layer of the extended surfaces for all the compositions of the Pt_xPd_{100-x} alloys. In addition, it was found that, among the three low-index extended surfaces, the extent of the Pd surface segregation was strongest in the open (110) surface and weakest in the closely packed (111) surface. Moreover, we predicted from our MC simulations that the equilibrium Pt-Pd nanoparticle would have a Pd-enriched shell and

a Pt-enriched core. In the Pd-enriched shell of the cubo-octahedral Pt-Pd nanoparticles, the Pd atoms would primarily occupy the (100) facet surface sites while the Pt atoms would mainly sit on the (111) facet surface sites.

Therefore, we have developed the MEAM potentials that could accurately describe the surface segregation process in the extended and nanoparticle surfaces of Pt-Pd alloys. This work enables us to quantitatively predict the surface composition of various Pt-Pd bimetallic nanostructures, and reliably simulate the surface segregation phenomena in the multi-component alloy systems containing Pt and Pd components in future studies.

5.0 MONTE CARLO SIMULATIONS OF SURFACE SEGREGATION AND SUBSURFACE ORDERING IN EXTENDED SURFACES AND NANOPARTICLES OF PLATINUM [SUB 3] IRON

5.1 ABSTRACT

We investigated the surface segregation phenomena in Pt_3Fe (111) surface, Pt_3Fe (100) surface, and surfaces of Pt3Fe cubo-octahedral nanoparticles by employing density functional theory (DFT) and Monte Carlo (MC) simulations based on modified embedded-atom method (MEAM). From our MC simulations, we predicted oscillatory composition profiles with Pt-enriched the first and the third layers for Pt_3Fe (111), (100), and nanoparticle surfaces. We also found that the subsurface composition and ordering can change dramatically with different bulk or overall compositions. The change in surface segregation mode from direct exchange to antisite segregation is responsible for the subsurface composition and ordering change.

5.2 INTRODUCTION

Surface segregation phenomenon in alloy materials normally results in different surface chemical composition from the bulk composition,[106] which plays an essential role in tailoring the reactivity of heterogeneous catalysts. Platinum-based bimetallic alloys were demonstrated to have superior catalytic activity compared to pure Pt catalyst in catalyzing oxygen reduction reaction (ORR), whose slow kinetics is one of the key problems affecting the performance of proton-exchange membrane fuel cells (PEMFCs).[12,13,107–109] The improvement in the cat-

alytic activity of ORR has been proved to be ultimately determined by the surface structures of those Pt-based catalysts that formed through the surface segregation process during the annealing treatment. For example, Pt_3Ni (111) surface displayed 10-fold higher activity than pure Pt catalyst because surface segregation leads to 100% Pt in the outermost layer and 50% Pt-50% Ni in the subsurface layer.[12] Additional to surface composition profile, atomic arrangement or atomic ordering in the surface region is also very important in catalytic applications and is termed as ensemble effect. Pd monomers isolated by Au atoms on AuPd (100) surface were identified to be the active site for promoting vinyl acetate synthesis.[110] The surface atomic ordering comes from the interdependence of surface segregation and short-range order (SRO) or long-range order (LRO).[51,111] Therefore, in order to accurately understand the surface chemistry processes occurring on the bimetallic catalyst surfaces and to fine-tune the surface structures in order to gain better performance, the equilibrium surface structures (surface composition profile and atomic ordering) must be understood properly.

In the present work, we will focus on elucidating the equilibrium surface structures of extended surfaces and nanoparticles of ordered Pt_3Fe alloy. Pt_3Fe was found to have more than 2 times higher activity for catalyzing ORR compared to pure Pt catalyst.[13] It is also widely used in other catalytic reactions and also used in magnetic applications. Pt_3Fe is an ordered alloy with $L1_2$ ordering up to 1500 K,[112] so it keeps ordered structure at normal experimental annealing temperature. A low-energy electron diffraction (LEED) study performed by Beccat et al. found $Pt_{80}Fe_{20}$ (111) surface equilibrated at 1200 K had a monotonically decreasing concentration profile: the outermost layer is almost pure Pt ($C_1 = 96 \pm 4$ at. %); the second layer and the third layer are also Pt-enriched ($C_2 = 84 \pm 7$ at. % and $C_3 = 85 \pm 15$ at. %). The experiment also revealed that the second surface layer is ordered with Pt_3Fe $L1_2$ structure although it contains less Fe atoms (about 15% against 25% in Pt_3Fe). Experimental works regarding surface segregation in Pt_3Fe (110) surface and surfaces of Pt_3Fe nanoparticle have also been done.[113,114] Theoretical calculations showed that surface segregation in ideal Pt_3Fe (111) could be achieved simply by exchanging the Pt atoms in the subsurface layer with the Fe atoms in the outermost layer.[23] Moreover, in ordered alloy, bulk composition could have strong influence on surface segregation due to the off-stoichiometric effect.[81,115] In our previous work, we have demonstrated that an

infinitesimal increase in bulk Pt composition off the stoichiometry of Pt_3Ti alloy would cause the strong segregation of Pt antisites to the outermost surface and form a pure Pt skin.[100] Hence, in Pt_3Fe ordered alloy, surface segregation through exchange or antisites migration is anticipated to coexist and the competition between the two surface segregation modes are expected to affect the surface composition profile and atomic ordering.

Theoretical prediction of surface segregation and surface ordering in binary alloys has long been pursued.[53–56,78,116–120] In our previous work, we have demonstrated that Monte Carlo (MC) simulations coupled with modified embedded-atom method (MEAM) empirical interatomic potentials can be successfully applied to predict surface segregation and surface ordering in various Pt-based bimetallic alloys.[2,57–60,100] In this work, we applied the same computational approach to predict the surface segregation and surface ordering in ordered Pt_3Fe alloy. We first developed Pt-Fe MEAM potential based on first-principles density functional theory (DFT) calculations. With the developed potential, MC simulations were performed for extended (111) and (100) surfaces of Pt_3Fe alloy. Then, surface segregation in cubo-octahedral Pt_3Fe nanoparticles was studied. The surface composition profile and surface ordering as a function of bulk composition were discussed.

5.3 COMPUTATIONAL METHODS

In this study, we use both first-principles DFT and MEAM interatomic potential to evaluate the total energy of Pt-Fe system. Accurate but slow DFT calculations are conducted mainly for building a database of physical properties of Pt-Fe system such as lattice constants, heats of formation of Pt-Fe phases, and surface segregation energies. The values of properties in the database were thereafter served as targeted values for fitting empirical parameters in Pt-Fe MEAM potentials. Due to the efficiency of MEAM potential, it could be coupled with Monte Carlo (MC) simulations to determine equilibrium physical properties at finite temperature, where configurational and vibrational effects are needed to be considered. In the following, the setups for DFT calculations and atomistic models used in this study are described. The detailed formulation of MEAM potentials and the implementation of the MC simulation were described in detail in the original MEAM paper[47] and our previous works.[57,58]

Spin-polarized first-principles DFT calculations were conducted by using Vienna Ab Initio Simulation Package (VASP).[71,72] In all the DFT calculations, valence electrons were treated explicitly in the Kohn-Sham equations and core electrons were described by pseudopotential approach with projector augmented-wave (PAW) method.[121] The generalized gradient approximation (GGA) with the PW91 functional was used for evaluating the exchange-correlation energy.[42] A plane-wave basis set with a 600 eV kinetic energy cutoff was used in all calculations. Monkhorst-Pack k-point mesh was used for Brillouin zone integration.[75] The equilibrium atomic geometry was obtained by minimizing the Hellman-Feynman forces till the forces acting on each atom were smaller than 0.01 eV/Å.

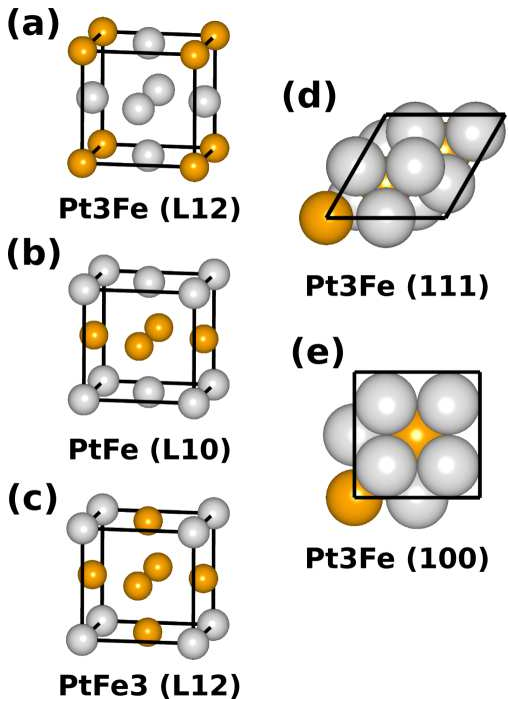

Figure 5.1: The structures of unit cells of Pt-Fe ordered phases and surfaces (a) Pt_3Fe $L1_2$ phase (b) PtFe $L1_0$ phase (c) $PtFe_3$ $L1_2$ phase (d) Pt_3Fe (111) surface (e) Pt_3Fe (100) surface. Pt atoms are represented by grey balls. Fe atoms are represented by orange balls.

Three Pt-Fe ordered phases exist in the Pt-Fe phase diagram, which are Pt_3Fe, PtFe, and $PtFe_3$ phases that have $L1_2$, $L1_0$, and $L1_2$ structures, respectively.[112] The unit cells of the three ordered phases are shown in Fig. 5.1(a)-(c). Lattice constants and heats of formation of the three ordered phases were determined by using DFT. In these bulk-phase calculations, a $16 \times 16 \times 16$ Monkhorst-Pack k-point mesh was used for Brillouin zone integration. Surface slab models were constructed in order to compute surface segregation energies for Pt_3Fe (111) and Pt_3Fe (100) surfaces. For Pt_3Fe (111) surface, p(2×2) unit cell (4 atoms in each layer) was used and it contains eight surface layers in the slab. For Pt_3Fe (100) surface, c(2×2) unit cell (4 atoms in each layer) was used and the model also has eight layers. A 12 Åvacuum gap was added over the slab for creating surfaces. The surface structures for bulk-truncated Pt_3Fe (111) and 100 surfaces are shown in Fig. 5.1(d) and Fig. 5.1(e), respectively. Bulk-

terminated Pt_3Fe (111) surface has a (2×2) superlattice and the composition is the same as bulk composition which is 75 at.% Pt-25 at.% Fe. There are two possible terminations for bulk-terminated Pt_3Fe {100} surfaces. Pt_3Fe (100) surface has a (2×2) superlatticce and contains 50 at. % Pt, while Pt_3Fe (200) surface is a pure Pt layer. Based on the bulk-truncated Pt_3Fe (111) and (100) surface models, various surface-segregated models were also constructed by exchanging Pt and Fe atoms or introducing Pt antisite or Fe antisite into the model in order to calculate surface segregation energies. The structures of these surface-segregated models will be elaborated later. In surface calculations, a $5\times5\times1$ Monkhorst-Pack k-point mesh was used for Brillouin zone integration.

Table 5.1: Comparison of the calculated properties of Pt_3Fe ($L1_2$), PtFe ($L1_0$), and $PtFe_3$ ($L1_2$) bulks using the developed MEAM potential and the DFT method.

	MEAM	MEAM-L	GGA-DFT	Exp.
		Properties of Pt_3Fe ($L1_2$)		
Lattice constant a (Å)	3.884	3.83	3.922	3.88
Heats of formation (eV/atom)	−0.54	−0.46	−0.16	−0.25
		Properties of PtFe ($L1_0$)		
Lattice constant a (Å)	3.850	3.81	3.864	3.838
Lattice constant c (Å)	3.697	3.71	3.769	3.715
Heats of formation (eV/atom)	−0.86		−0.19	−0.28
		Properties of $PtFe_3$ ($L1_2$)		
Lattice constant a (Å)	3.754	3.70	3.733	3.75
Heats of formation (eV/atom)	−0.61		−0.02	−0.10

5.4 RESULTS AND DISCUSSION

5.4.1 Developing Pt-Fe MEAM potential

We determined MEAM parameters for the Pt-Fe interatomic interaction by fitting MEAM-calculated properties to corresponding DFT-calculated values. The values of the parameters are shown in the supplemental information. The properties involved in the fitting process are lattice constants and heat of formations of the three ordered phases of Pt-Fe alloy ($PtFe_3$, PtFe, and Pt_3Fe). Besides bulk information, surface properties, such as surface segregation energies, were also fitted to reproduce the values calculated by employing DFT method. The bulk information calculated by our developed MEAM potential of the three ordered Pt-Fe phases are listed in Tab. 5.1. In the same table, for comparison, values obtained by DFT calculations, experiments,[122] and previously developed Pt-Fe MEAM potential[123] are also tabulated. As can be read from Tab. 5.1, the lattice constants obtained by using our MEAM potential are comparable to other methods, especially very closed to DFT values and experimental values. However, heats of formation predicted are much lower than experimental values. The much more negative heats of formation was developed on purpose in order to predict comparable order-disorder transition temperature with experiment for ordered Pt_3Fe phase.

Surface segregation energies for Pt_3Fe (111) surfaces both calculated from our developed MEAM potential and DFT method (in parentheses) are listed in Fig. 5.2. Similarly, the surface segregation energies for Pt_3Fe (100) surfaces are listed in Fig. 5.3. Along with the surface segregation energy values, the pre-segregation and post-segregation surface structures associated the surface segregation energies are also shown in Fig. 5.2 and Fig. 5.3. For most of the surface segregation energies, first-principle DFT values could be quantitatively reproduced by our MEAM potential. For all the surface segregation events involved in our fitting process, the tendencies of segregation or non-segregation predicted by MEAM potential are in well agreement with DFT calculations. We will discuss the physical indications of these surface segregation energies in detail when we discuss surface segregation in Pt_3Fe (111) and Pt_3Fe (100) extended surfaces.

As mentioned above, we deliberately decrease the heats of formation of Pt-Fe phases to enable our MEAM potential to predict correct order-disorder transition temperature for Pt_3Fe given that ordering is an essential factor affecting surface segregation phenomenon. We used MC simulations to estimate the critical order-disorder transition temperature. In our simulation, the long-range order (LRO) parameter was used as a measurement of ordering in the Pt_3Fe crystal. The LRO is defined as $(P^{\alpha}_{\mathrm{Pt}} - 0.75)/0.25$, where P^{α}_{Pt} is the probability of Pt atoms locating at Pt sublattices. With this definition, the LRO equals to unity if Pt_3Fe crystal is perfectly ordered and equals to null if the alloy is completely disordered. Starting from a perfectly ordered Pt_3Fe bulk containing 500 atoms, we carried out 1×10^7 MC simulation steps to ensure full convergence of the system energy. We sampled the LRO of the system every 1000 steps for the last 5×10^6 steps. In each MC step, we attempted to exchange the positions of two randomly selected Pt atom and Fe atom. After the simulation, we calculated the average of all the sampled LRO values. Fig. 5.4 plots the obtained LRO curve within the temperature range of 1000-1900 K. The Pt_3Fe crystal is found to be nearly ordered below 1400 K. LRO starts to decrease quickly to zero from $T = 1500$ K. Hence, the order-disorder transition temperature predicted by our Pt-Fe MEAM potential (between 1400K and 1500K) is satisfactory compared to the experimental value (about 1500K).[112]

5.4.2 Surface segregation in Pt_3Fe (111) surface

5.4.2.1 Surface segregation energies in Pt_3Fe (111) surface Surface segregation energies were calculated by computing the energy differences between the surface-segregated surface models and the bulk-terminated surface models. Three kinds of surface models were involved in surface segregation energy calculations, they are Pt_3Fe (111) surface with ideal stoichiometry, Pt-deficient Pt_3Fe (111) surface, and Pt-enriched Pt_3Fe (111) surface. For Pt_3Fe (111) surface with ideal stoichiometry, three Pt-segregated surface models were constructed by exchanging the Fe atom in the outermost layer with a Pt atom in the second, the third, or the fourth layer. The surface models and corresponding surface segregation energies both calculated by using MEAM and DFT methods are shown in Fig. 5.2(a). The convention adopted here is that a negative value of surface segregation energy means that

the Pt atom prefers surface segregation, and vice versa. For the three surface segregation processes through exchanging, corresponding Pt surface segregation energies are calculated by DFT to be −0.39 eV, −0.13 eV, and −0.01 eV, respectively. Our calculated surface segregation energy is in good agreement with values calculated from other group.[23] Negative Pt surface segregation energies indicate that Pt surface segregation will occur in the surface region through exchanging instead of keeping bulk-terminated surface. The $L1_2$ ordering of Pt_3Fe crystal would be retained in the bulk region since the influence of the surface is diminishing in the fourth layer.

The off-stoichiometric effect on the surface segregation of Pt_3Fe (111) surface is investigated by calculating surface segregation energies of Fe antisite and Pt antisite defects in the Pt-deficient model and Pt-enriched model, respectively. For studying the surface segregation of Pt or Fe antisite, Pt or Fe antisite was introduced into the first, the second, the third, and the fourth layer of ideal-stoichiometric Pt_3Fe (111) surface model. The surface segregation energy of a Pt or Fe antisite is defined as the energy difference between antisite-segregated models (antisite in the first, the second, and the third layer) and the model with antisite in the bulk (antisite in the fourth layer). Pt and Fe antisite surface segregation models and energies both calculated with DFT and developed MEAM potentials are shown in Fig. 5.2(b) and Fig. 5.2(c), respectively.

From the calculated surface segregation energies shown in Fig. 5.2(b), it can be seen that Pt antisites strongly prefer to segregate to the outermost layer with energy decrease of 0.75 eV. In contrast, Pt antisites do not segregate to the second layer since the process would increase the system energy by 0.19 eV. Therefore, our calculations suggest that, in Pt-enriched Pt_3Fe (111) surface, Pt surface segregation would occur due to the segregation of Pt antisites. Fe antisites prefer to segregate to the subsurface layer with energy decrease of 0.20 eV (Fig. 5.2(c)). The surface segregation to the outermost layer is inhibited with energy penalty of 0.48 eV. Consequently, in the Pt-deficient Pt_3Fe (111) surface, Fe antisites would segregated to the second layer.

5.4.2.2 Surface segregation in Pt_3Fe (111) surface studied by MC simulation

Quantitative predictions of surface composition profiles cannot be accomplished solely by DFT calculations due to its high computational costs. In order to give quantitative predictions of equilibrium surface composition profile, we combine MC simulations with our developed Pt-Fe MEAM potential. To simulate the surface segregation of Pt_3Fe (111) surface by using MC simulations, we constructed a bulk-truncated Pt_3Fe (111) surface slab model containing 15 layers with 48 atoms in each layer. Based on the bulk-truncated surface model that contains 75 at. % Pt, we introduced Pt or Fe antisites into the model to vary the overall Pt concentration and constructed five Pt_3Fe (111) surface models with Pt composition ranging from 70 to 80 at. %. Starting from these initial structures, we conducted 1×10^7 MC steps at $T = 1200$ K and sampled the Pt concentrations in each layer every 1000 steps in the last 5×10^6 steps. In each MC step, we attempted to exchange the positions of two randomly selected Pt and Fe atoms or displace a randomly selected atom in the [111] direction. Surface composition profiles were calculated by averaging the sampled surface Pt concentrations. Due to the finiteness of the slab model used in the simulation, the Pt composition in the bulk region (the five layers in the middle of the slab model) could be varied due to the surface segregation. In order to simulate an extended surface with infinite bulk region, initial overall Pt compositions of the slab models were shifted from the desired bulk compositions so that we could have the desired bulk compositions in the bulk region after simulations.

In Fig. 5.5(a), the equilibrium Pt compositions in first three layers as a function of the Pt bulk composition are plotted. Over the bulk composition we examined in the simulations, oscillatory surface composition profiles were observed, in which the first and the third layer are Pt-enriched while the second layer is Pt-depleted. The oscillatory composition profile is due to the exchange of surface Fe atoms with subsurface Pt atoms and Fe antisites segregation to the subsurface layer. Between Pt bulk composition 72.5 at. % and 75 at. %, there is a leap in the surface compositions of the outermost layer, because staring from 75 at. %, Pt antisites segregation becomes active and enhances the Pt surface segregation. When Pt

antisite segregation becomes active, the Pt composition also increases quickly in the third layer, because Pt antisite segregation suppress Pt surface segregation though exchange. As a result, Fe atoms initially in the outermost surface could also migrate to the bulk region instead of residing in the subsurface layer.

The surface atomic ordering is also altered because of the surface segregation. As a result of surface segregation, the outermost layer is covered almost by pure Pt atoms. In the second layer, ordering is significantly affected by surface segregation. At the bulk composition of 70 at. % Pt, as shown in Fig. 5.5 (b), the subsurface has about 1/2 ML Pt coverage with the ordering of bulk-truncated PtFe $L1_0$ (111) surface. With the increasing bulk Pt composition, the Pt concentration also increases in the second layer. As a consequence, subsurface ordering starts to transit from PtFe $L1_0$ (111) ordering to Pt_3Fe $L1_2$ (111) ordering. At the bulk composition of 75 and 80 at. % Pt, the subsurface layer has mainly Pt_3Fe $L1_2$ (111) ordering yet with about 5 at. % Fe antisite defects due to the Pt depletion in the subsurface layer.

Experimentally, a monotonously decreasing Pt composition profile of the first three layers ($96 \pm 4, 88 \pm 7, and 85 \pm 15$ at. % Pt) was found for $Pt_{80}Fe_{20}$ (111) surface.[124] Compared to our calculated values (99.7, 70.7, and 85.6 at. % Pt), our computations instead, predict an oscillatory surface composition profile. Pt compositions of the first and the third layer are well agreed. However, the discrepancy in the composition of the second layer makes the qualitative disagreement between the experimental data and our simulation values. Our prediction of the Pt_3Fe (111) surface composition profile from MC simulation is consistent with the surface segregation trend indicated by the first-principles DFT methods since none of the calculated surface segregation energies suggests the enrichment of Pt in the subsurface layer. Moreover, our theoretical prediction is consistent with another simulation work, which also predicted the oscillatory composition profile.[125] Our simulation predict a Pt_3Fe $L1_2$ (111) surface ordering in the subsurface for segregated $Pt_{80}Fe_{20}$ (111) surface, which is in good agreement with experimental findings.[124]

5.4.3 The surface segregation of Pt_3Fe (100) surface

5.4.3.1 Surface segregation energies in Pt_3Fe (100) surface Bulk-terminated Pt_3Fe (100) surface has two possible terminations: pure Pt surface and 50% Pt surface (see Fig. 5.1(e)). To examine the surface segregation through Pt and Fe exchange, we constructed an eight-layer slab model that has both two kinds of surfaces (see Fig. 5.3(a)). Based on the model, we calculated the surface segregation energies of the subsurface Pt atoms segregating to the surface by exchanging positions with Fe atoms in the 50 % Pt surface termination (see Fig. 5.3(a)). The surface segregation of one subsurface Pt lowers the system energy by 0.36 eV. If the other subsurface Pt atom also segregates to the surface, the system energy will be further lowered by 0.56 eV. Therefore, pure Pt termination is more energetically favorable for ideal-stoichiometric Pt_3Fe (100) surface.

As shown in Fig. 5.3(b) and 5.3(c), the surface segregation energies of Pt and Fe antisite are also calculated. Similar to Pt_3Fe (111) surface, Pt antisite tends to segregate to the outermost surface with energy decrease of 0.64 eV and does not tend to segregate to the subsurface layer with system energy increase of 0.26 eV. Fe antisites, on the other hand, prefer to migrate to the subsurface layer with energy decrease of 0.40 eV. Moreover, it is energetically unfavorable for Fe antisites to segregate to the surface with energy penalty of 0.29 eV.

5.4.3.2 Surface segregation in Pt_3Fe (100) surface studied by MC simulations Monte Carlo simulations were performed to investigate the surface segregation of Pt_3Fe (100) surfaces at annealing temperature $T = 1200$ K. The bulk-truncated slab model of Pt_3Fe (100) surface has 16 layers and there are 32 atoms in each layer. Because the surface slab model has even number of layers, it has both pure Pt surface termination and 50 % Pt surface termination. The examined bulk compositions are also from 70 to 80 at. % Pt. The setups used in the MC simulations are the same to those used in MC simulations of Pt_3Fe (111) surfaces.

The equilibrium Pt compositions in the first three layers as a function of the Pt bulk composition are plotted in Fig. 5.6(a). During the simulation, the outermost layer termi-

nated with pure Pt stays nearly untouched, while the other surface layer initially covered with 50 at. % Pt quickly turns into pure Pt layer through Pt segregation (shown in Fig. 5.7). The equilibrium surface has a pure Pt outermost surface and third layer over the whole bulk composition range simulated. Below 75 at. % Pt bulk composition, Pt composition in the second layer is lower than 50 at. % due to the segregation of Fe antisites and Pt surface segregation through exchange. Pt composition in the second layer keeps around 50 at. % when the bulk Pt composition is above 75 at. %. The resulted surface composition profiles from MC simulations are consistent with the suggestions of calculated surface segregation energies.

The atomic ordering in the subsurface layer also evolves with variations in bulk composition. At the Pt bulk composition of 70 at. %, the Pt coverage is about 1/4 ML in the subsurface layer and an ordered structure is formed that Pt atoms are surrounded all by Fe atoms as shown in Fig. 5.6(b). At 75 at. % Pt bulk composition, the subsurface forms bulk-terminated Pt_3Fe $L1_2$ (100) structure with 1/2 ML Pt coverage. At 80 at. % Pt bulk composition, the subsurface Pt concentration is slightly Pt enriched compared to 1/2 ML Pt converage. The ordering of the subsurface layer is basically bulk-terminated Pt_3Fe $L1_2$ (100) structure with a few Pt antisite defects.

5.4.4 The surface segregation of Pt_3Fe nanoparticles

Working catalysts are normally produced as nanoparticle to utilize their high surface-volume ratio. So, it is essential to understand surface segregations in nanoparticles in order to understand surface structures of working catalysts. Surface segregation in nanoparticles is more complex compared to extended surfaces, because factors that are lacked in extended surfaces would be involved, e.g. the limited size of nanoparticles, the presence of under-coordinated atoms in edges or corners, and the co-existence of differently oriented surfaces.

Monte Carlo simulations were performed to investigate the surface segregation in Pt_3Fe nanoparticles. In this work, we modeled cubo-octahedral nanoparticles, which are enclosed by (111) and (100) surfaces, with diameters of 2.6 nm (586 atoms) and 5.2 nm (4033 atoms). The atomic structure of the bulk-terminated Pt_3Fe nanoparticle is shown in Fig. 5.8. We first constructed bulk-terminated nanoparticles and then tune the overall Pt composition to be in the range of 70 to 85 at. %. The equilibrium configuration of the system is then achieved by running the MC simulation 2×10^6 steps at temperature $T = 600$ K. In each MC step, only the exchange of Pt and Fe positions is attempted.

Fig. 5.9 shows the equilibrium Pt composition in the first three layers as a function of the overall Pt composition in the nanoparticles. For both sizes of nanoparticles, over the composition range tested, Pt atoms are enriched in the outermost surfaces and the amount of enrichment is greater in larger nanoparticles (5.2 nm). Meanwhile, Pt atoms are depleted from the second layer. The atomic surface structures of annealed 2.6 nm and 5.2 nm nanoparticles with various Pt compositions are shown in Fig. 5.10. As can be seen in the figure, at the Pt composition of 70 at. % , (100) surfaces are covered almost by pure Pt, while (111) surface still have a considerable amount of Fe atoms in the surface. For 2.6 nm nanoparticle, the surface segregation barely occurs on (111) surfaces, so the surfaces still keep the bulk-terminated ordering at this bulk composition. This observation indicates that Pt surface segregation to (100) surface sites and lower-coordinated sites (corners and edges) is preferential. With increasing Pt composition, the surfaces of nanoparticles are covered by more and more Pt atoms. For 2.6 nm nanoparticle, pure Pt outermost surface forms at the Pt bulk composition between 80 and 85 at. % in contrast with the Pt composition between

75 and 80 at. % for 5.2 nm nanoparticle. Larger nanoparticle can form pure Pt shell with lower bulk Pt composition because more Pt antisites are available for surface segregation in the core.

Fig. 5.11 shows the atomic structures of subsurface layer of surface-segregated nanoparticles at various bulk compositions. For 2.6 nm nanoparticles, the area of facets in the subsurface layer are very small, it is difficult to make conclusive description about the ordering pattern. Basically, for 2.6 nm nanoparticles, (100) facets of subsurface layer is almost covered by pure Fe atoms at Pt bulk composition of 70 at. %. Some (111) facets at the composition shows bulk-terminated PtFe $L1_0$ (111) ordering, while other (111) facets have Pt coverage less than 1/2 ML. With increasing overall Pt composition, the Pt composition in the subsurface layer starts to increase. At 85 at. % bulk Pt composition, the Pt coverage of (100) facets drops to 1/2 ML and have the ordering of bulk-terminated Pt_3Fe (100) surface. For (111) facets, the ordering becomes bulk-terminated Pt_3Fe $L1_2$ (111) ordering. Ordering pattern in the subsurface layer can be seen more clearly in the 5.2 nm nanoparticles. At 70 and 75 at. % bulk Pt compositions, (100) facets have the ordering of bulk-terminated Pt_3Fe (100) surface with about 50 at. % Pt. (111) facets also have 1/2 ML Pt coverage and the ordering of bulk-terminated PtFe $L1_0$ (111) surface. With increasing Pt bulk composition, the Pt concentration and ordering in the subsurface layer of (100) facets show little change. At bulk Pt composition of 80 at. %, the ordering of (111) facets in the subsurface layer is a mixture of $L1_2$ and $L1_0$ ordering. When the Pt composition reaches 85 at. %, the ordering is mainly bulk-terminated Pt_3Fe $L1_2$ ordering.

In order to investigate the influence of surface segregation on the ordering of the cores region of nanoparticles, we monitored the sublattice occupation by Fe atoms during the simulation. The unit cell of Pt_3Fe $L1_2$ crystal is divided into four sublattices (shown in Fig. 5.12(a)), the occupation fractions of the four sublattices by Fe atoms averaged over the last million steps are shown in Tab. 5.2. If the Pt_3Fe crytal has the perfect $L1_2$ ordering, the sublattice occupation by Fe atoms should be (1,0,0,0), which means one of the sublattices is completely occupied by Fe atoms (shown in Fig. 5.12 (b)). If Pt_3Fe alloy is completely disordered, the occupation should be (0.25 0.25 0.25 0.25), which means the occupation fraction is equal to the composition of Fe (shown in Fig. 5.12(c)). In off-stoichiometric Pt_3Fe

alloy, long-range order of Pt_3Fe $L1_2$ phase is disturbed by Fe or Pt antisites. In Pt-deficient ordered Pt_3Fe, Fe antisites would partially occupied another sublattice besides the fully Fe-occupied sublattice, while in Pt-enriched case, Pt antisites would reduce the occupation of Fe in the Fe-occupied sublattice(shown in Fig. 5.12(d)). At overall Pt composition of 70 at. %, for 2.6 nm nanoparticle, sublattice 2 is fully occupied by Fe atoms and sublattice 3 is nearly half occupied by Fe atoms. The ordering is in between Pt_3Fe $L1_2$ ordering and PtFe $L1_0$ ordering because of the existing Fe antisites in the core region. With increasing overall Pt concentration, the occupation of Fe atoms in sublattice 3 is reduced. At overall Pt composition of 80 and 85 at. %, the ordering of core region is essentially Pt_3Fe $L1_2$ ordering. For larger nanoparticles (5.2 nm), the similar trend of evolution of ordering in the core region with over Pt composition is found, as compared to 2.6 nm nanoparticle. At overall Pt composition of 85 at. % for the 5.2 nm nanoparticle, excess Pt antisites stay in the core region after the saturation of Pt atoms in the outermost layer, which causes shortage of Fe atoms and degradation of $L1_2$ ordering in the core region.

5.5 CONCLUSION

In this work, we have performed the DFT calculations and MEAM potential-based MC simulations to study the surface segregation phenomenon in Pt_3Fe (111) surface, Pt_3Fe (100) surface, and surfaces of Pt_3Fe cubo-octahedral nanoparticles.

Our DFT results for stoichiometric Pt_3Fe (111) surface show that surface segregation of Pt atoms can occur through the exchange of surface Fe atoms with subsurface Pt atoms. For off-stoichiometric Pt_3Fe (111) surfaces, we calculated the surface segregation energies of Fe antisites in Pt-deficient surface and Pt antisites in Pt-enriched surface. The results show that Pt antisites have a strong tendency to segregate to the outermost surface but would not prefer to migrate to the subsurface layer. In contrast, Fe antisites would not segregate to the outermost layer but prefer segregation to the subsurface layer. For stoichiometric Pt_3Fe (100) surface, Pt surface segregation can also be achieved by exchanging surface Fe atoms with subsurface Pt atoms. The surface segregation energies also suggest that pure Pt

termination for Pt_3Fe (100) surface is preferred. In off-stoichiometric Pt_3Fe (100) surface, it is also found that Pt antisites segregate to the outermost layer and Fe antisites segregate to the subsurface layer.

With our developed Pt-Fe MEAM potential, we performed MC simulations to investigate the equilibrium surface composition profile and surface atomic ordering in extended surfaces and surfaces of cubo-octahedral nanoparticle at annealing temperature $T = 1200$ K. Our Pt-Fe MEAM potential is carefully validated to be capable of reproducing various bulk properties, order-disorder transition temperature of Pt_3Fe, and various surface segregation energies, as compared to experimental data and DFT-calculated values.

The MC simulations suggest that surface segregation in Pt_3Fe (111) surface would result in an oscillatory composition profile, in which the outermost surface and the third layer are enriched in Pt and the second layer is Pt-depleted. The subsurface layer has the ordering of bulk-terminated PtFe $L1_0$ (111) surface at the bulk Pt composition of 70 at. %. With the increasing bulk Pt composition, at 80. at. %, the subsurface ordering becomes the ordering of bulk-terminated Pt_3Fe $L1_2$ (111) surface. The transition of the subsurface atomic ordering is a result of change of mode of Pt surface segregation from direct exchange in Pt-deficient surfaces to Pt antisites segregation in Pt-enriched surfaces. In Pt_3Fe (100) surface, the outermost layer and the third layers are completely occupied by Pt atoms, while the second layer has more than 50 at. % Fe atom in Pt-deficient surfaces and about 50 at. % Fe in Pt-enriched surfaces. The ordering in the subsurface layer evolves from ordered pattern with 3/4 ML coverage Fe at bulk composition of 70 at. % Pt to bulk-terminated Pt_3Fe (100) surface with 1/2 ML coverage of Fe at 80 at. % Pt bulk composition. Surface segregation in cubo-octahedral nanoparticles of Pt3Fe also results in oscillatory composition profile for both 2.6 nm and 5.2 nm nanoparticles. The surface segregation tendency in 5.2 nm nanoparticle is stronger than the smaller nanoparticle. Pt surface segregation to (100) surface is preferential than to (111) surfaces. The subsurface ordering also evolves with bulk compositions similarly to extended surfaces.

Above all, through the atomistic simulation, this work provides details and insights into the surface segregation phenomenon in Pt_3Fe surfaces and nanoparticles. The understanding gained in this study would provide useful instructions for designing and fabricating Pt_3Fe alloys as high performance catalysts.

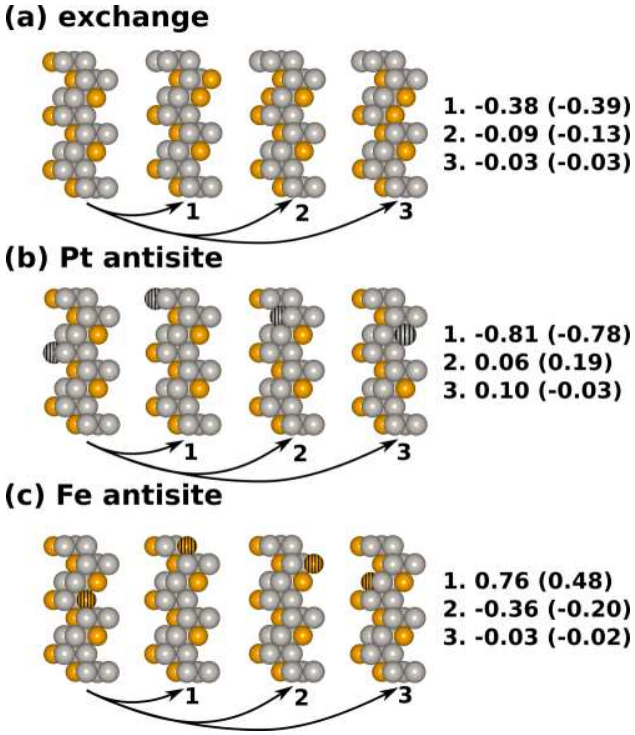

Figure 5.2: Various Pt_3Fe (111) surface models used to calculate the surface segregation energies.

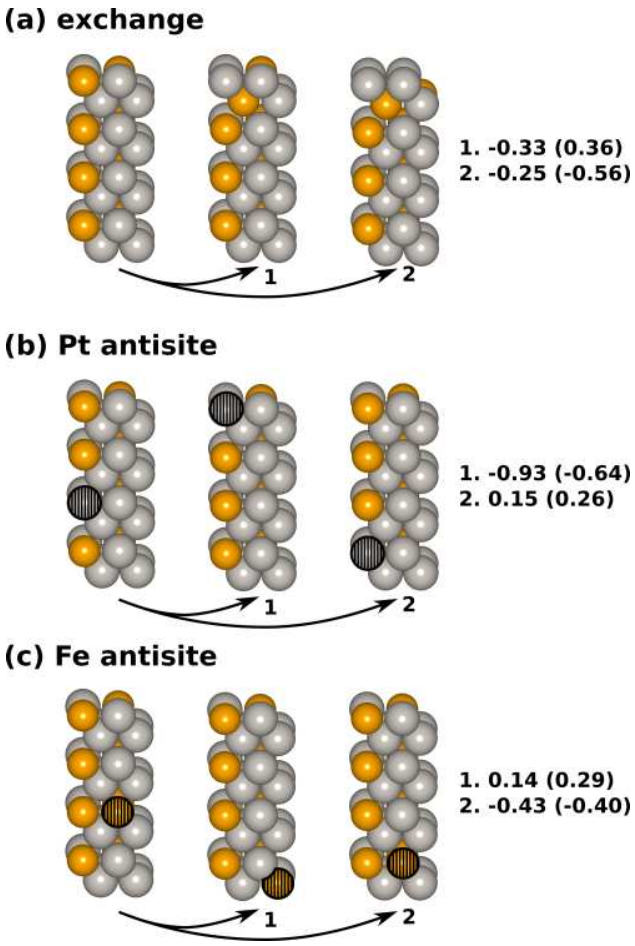

Figure 5.3: Various Pt_3Fe (100) surface models used to calculate the surface segregation energies.

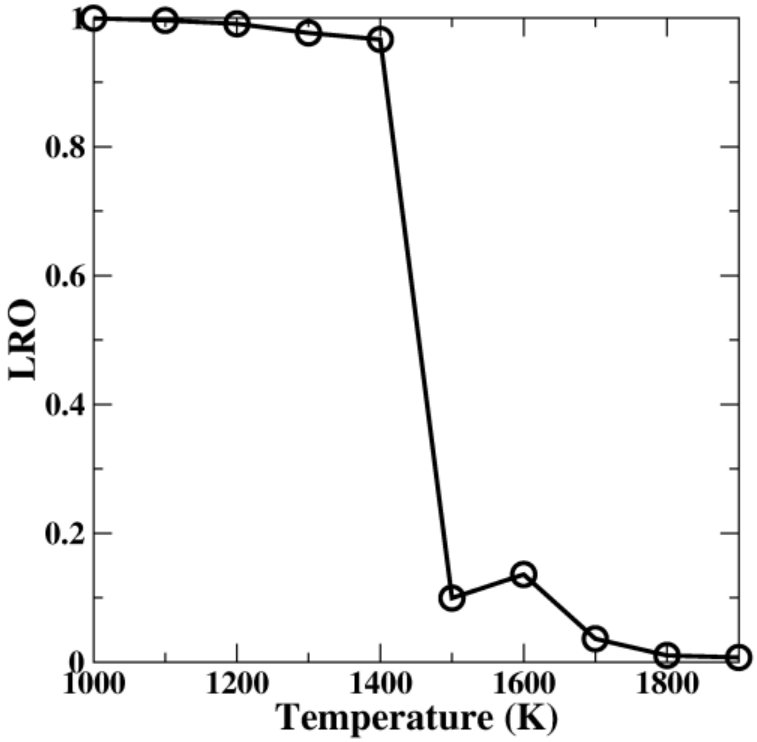

Figure 5.4: Evolution of the LRO of Pt_3Fe crystal as a function of temperature (from 1000K to 1900K) calculated by using the MC simulation based on our developed Pt-Fe MEAM potential.

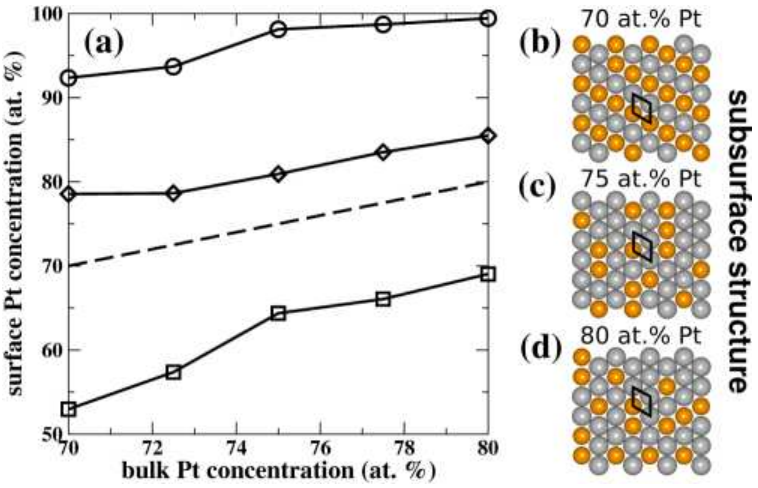

Figure 5.5: Calculated Pt concentrations in the outermost (circles), the second (squares), and the third layer (up-triangles) of the Pt_3Fe (111) surfaces annealed at $T = 1200$ K using the MC simulation methods based on our developed Pt-Fe MEAM potentials.

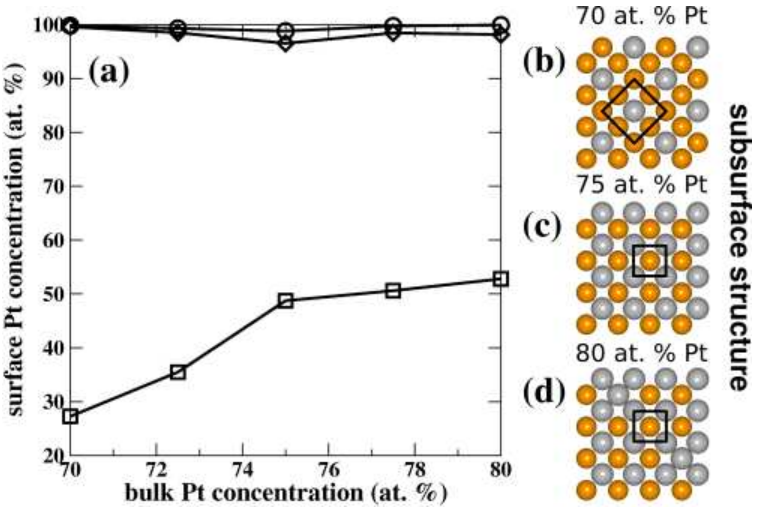

Figure 5.6: Calculated Pt concentrations in the outermost (circles), second (squares) of the Pt_3Fe (100) surfaces annealed at $T = 1200$ K using the MC simulation methods based on our developed Pt-Fe MEAM potential.

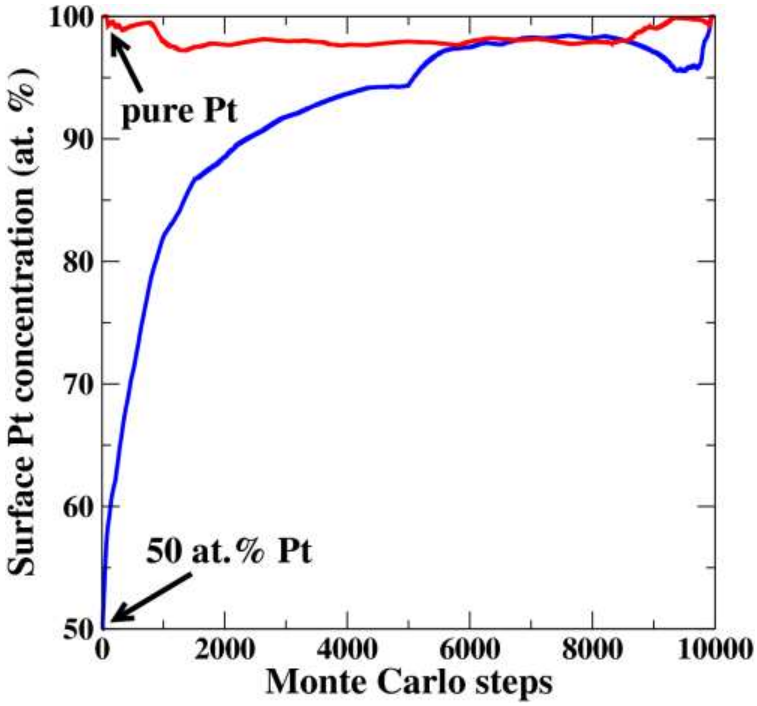

Figure 5.7: The evolution of the surface concentrations of the two outermost layers in the first 10000 steps of the MC simulation.

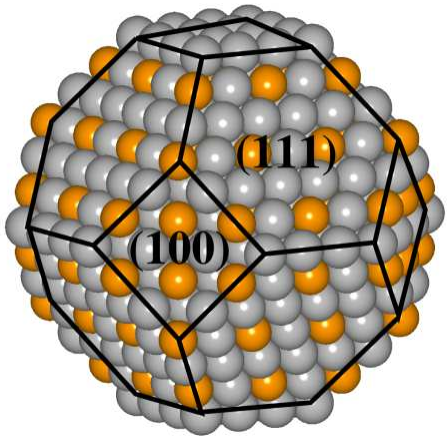

Figure 5.8: A bulk-terminated Pt_3Fe cubo-octahedral nanoparticle. The nanoparticle is enclosed by Pt_3Fe {111} and {100} surfaces.

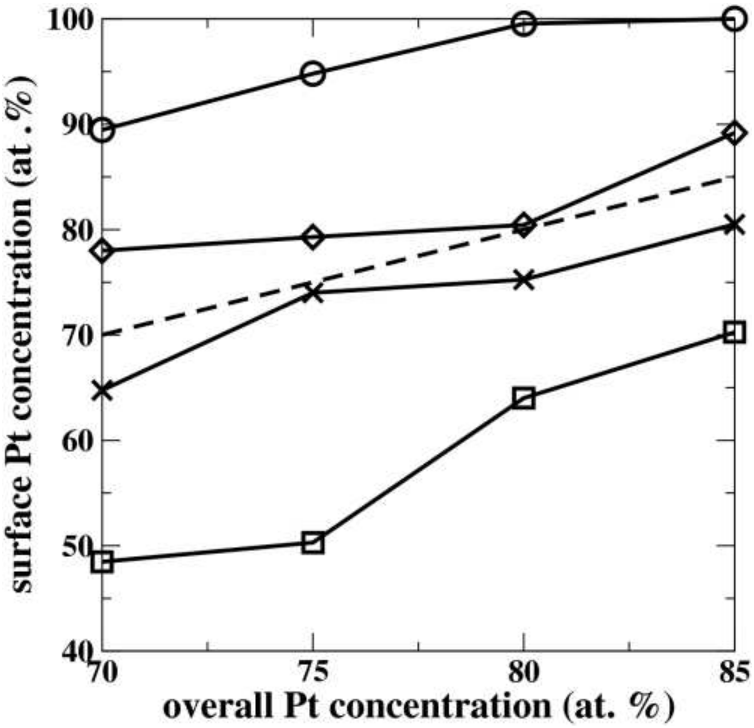

Figure 5.9: Calculated Pt concentrations in the outermost (circles), second (squares), the third layer (up-triangles), and the core region (crosses) of the 5.2 nm Pt_3Fe cubo-octahedral nanoparticles annealed at $T = 600$ K using the MC simulation methods and our developed MEAM potentials.

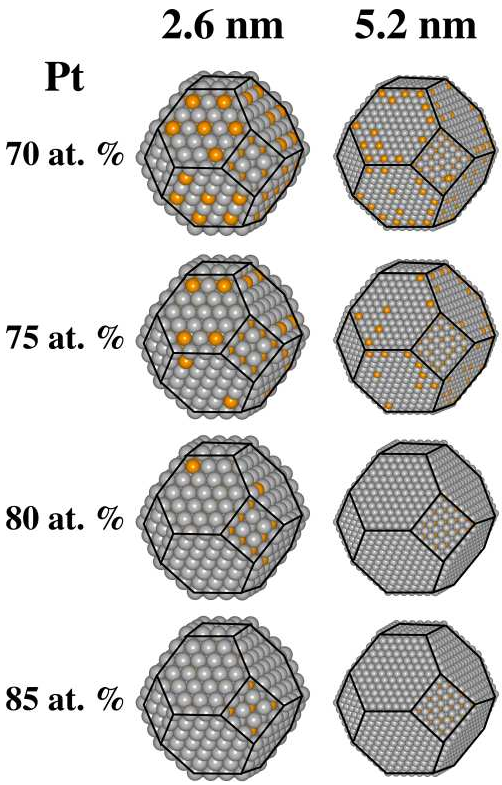

Figure 5.10: Equilibrium atomic structures of the outermost surfaces of Pt_3Fe nanoparticles with various overall Pt compositions and sizes after surface segregation.

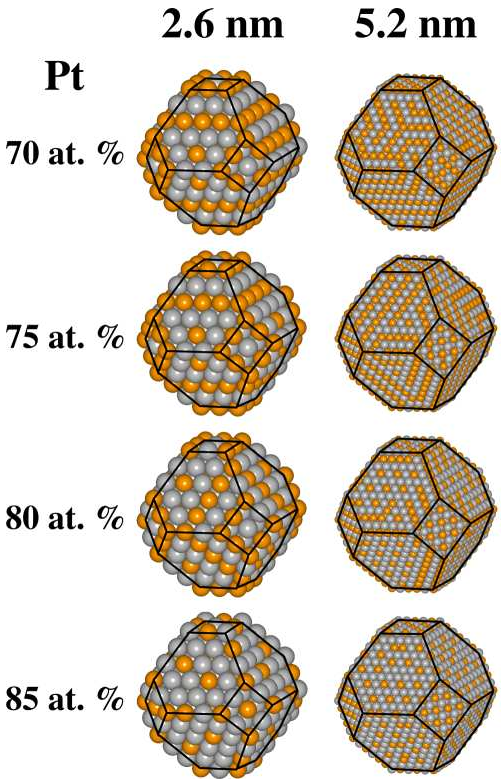

Figure 5.11: Equilibrium atomic structures of subsurface layers of Pt_3Fe nanoparticles with various overall Pt compositions and sizes after surface segregation.

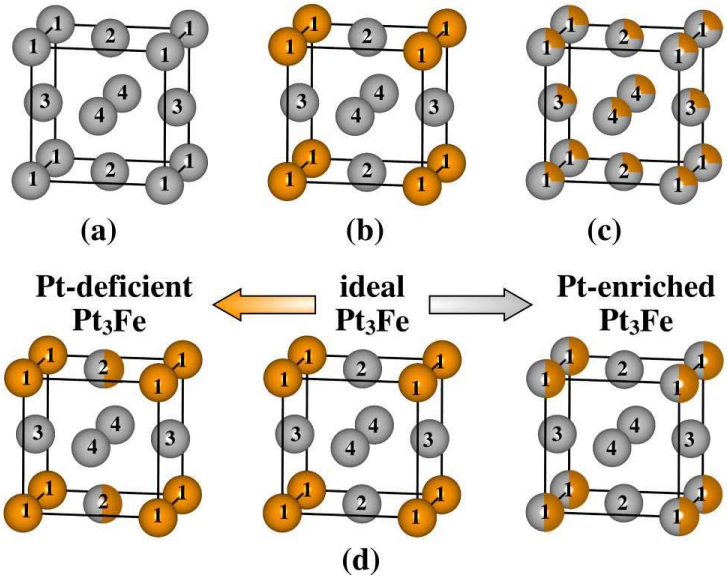

Figure 5.12: (a) The unit cell of Pt_3Fe $L1_2$ crystal is divided into four equivalent sublattices which are denoted by 1, 2, 3, 4 as shown in the figure. (b) unit cell of the stoichiometric ordered Pt_3Fe $L1_2$ crystal. (c) disordered Pt_3Fe alloy. (d) off-stoichiometric ordered Pt_3Fe $L1_2$ crystals.

Table 5.2: Atomic ordering in the core regions of nanoparticles indicated by the Fe fractions on the four sublattices of Pt_3Fe $L1_2$ unit cell.

	Fe fraction on sublattices							
overall Pt concentration	2.6 nm				5.2 nm			
	1	2	3	4	1	2	3	4
70 at. %	0.00	1.00	0.48	0.00	0.30	0.04	0.99	0.08
75 at. %	0.00	1.00	0.00	0.15	0.01	0.01	1.00	0.02
80 at. %	0.04	1.00	0.01	0.00	0.00	0.00	0.99	0.00
85 at. %	0.00	1.00	0.00	0.08	0.03	0.04	0.67	0.04

6.0 A FIRST PRINCIPLES STUDY OF OXYGEN REDUCTION REACTION ON A PLATINUM(111) SURFACE MODIFIED BY A SUBSURFACE TRANSITION METAL M (M = NICKEL, COBALT, OR IRON)

6.1 ABSTRACT

We have performed first-principle density functional theory calculations to investigate how a subsurface transition metal M (M = Ni, Co, or Fe) affects the energetics and mechanisms of oxygen reduction reaction (ORR) on the outermost Pt mono-surface layer of Pt/M(111) surfaces. In this work, we found that the subsurface Ni, Co, and Fe could down-shift the d-band center of the Pt surface layer and thus weaken the binding of chemical species to the Pt/M(111) surface. Moreover, the subsurface Ni, Co, and Fe could modify the heat of reaction and activation energy of various elementary reactions of ORR on these Pt/M(111) surfaces. Our DFT results revealed that, due to the influence of the subsurface Ni, Co, and Fe, ORR would adopt a hydrogen peroxide dissociation mechanism with an activation energy of 0.15 eV on Pt/Ni(111), 0.17 eV on Pt/Co(111), and 0.16 eV on Pt/Fe(111) surface, respectively, for their rate-determining O_2 protonation reaction. In contrast, ORR would follow a peroxyl dissociation mechanism on a pure Pt(111) surface with an activation energy of 0.79 eV for its rate-determining O protonation reaction. Thus, our theoretical study explained why the subsurface Ni, Co, and Fe could lead to multi-fold enhancement in catalytic activity for ORR on the Pt mono-surface layer of Pt/M(111) surfaces.

6.2 INTRODUCTION

Proton exchange membrane fuel cells (PEMFCs) can generate electricity through direct electrochemical conversion of hydrogen and oxygen into water. Switching from current fossil-fuel powered vehicles on road to hydrogen fuel-cell vehicles could benefit our society with improved air quality, health, and climate.[126] However, the sluggish kinetics of oxygen reduction reaction (ORR) at the cathode limits the energy conversion efficiency of PEMFCs and thus hinders their wide applications. Consequently, much research effort has been devoted to finding low-cost, high-performance, and long-durability electrocatalysts as the cathodes of PEMFCs.[3–7] In particular, alloying precious Pt with other transition metals has been used as an effective approach to tailoring the electronic structure and activity for ORR of Pt-based catalysts.[8,9] For example, Adzic et al.[10,11] deposited a Pt monolayer on various transition metal surfaces and found that the Pt monolayer on a Pd(111) substrate led to significantly improved catalytic activity for ORR. Using an annealing technique, Stamenkovic et al.[12,13] investigated the catalytic activities of surface segregated Pt alloys for ORR and found that the annealed Pt_3Ni and Pt_3Co alloys with Pt enriched outermost layers had much higher catalytic activity than poly-crystalline Pt.

To rationally design Pt alloy catalysts for ORR, first-principles density functional theory (DFT) calculations have been widely employed to establish the correlation between surface (most relevantly, the outermost layer and the subsurface layer) composition and catalytic activities of Pt alloys. It has been elaborated by Hammer and Nørskov that the calculated d-band center of transition metal surfaces is a useful indicator tomeasure the chemical reactivity ofmetallic catalysts.[14] Specifically, the difference in energy of the d-band center with respect to the Fermi level of metallic surfaces was found to well correlate with the O adsorption energy on these surfaces.[14] For ORR, some downshift of the d-band center with respect to that of pure Pt would lead to slightly weaker oxygen adsorption on the surface and was believed to enhance the reaction activity on such metallic catalysts.[8,9] Varying the type of subsurface transition metals has been shown to finetune the position of the d-band center of the outermost Pt monolayer and thus becomes a possible approach to design Pt alloy catalysts for ORR.[15,16] Furthermore, the optimized structure and energy of reactant,

intermediate, and product species (such as O_2, O, OH, and H_2O) adsorbed on the pure Pt and Pt alloy surfaces could be reliably computed using the DFT method.[17–24] It was found that there was a strong linear correlation between the adsorption energies of O and OH,[25] which are important factors governing the rate of ORR on metallic catalyst surfaces. It is widely believed that an optimal catalyst for ORR should bind the reactant intermediates neither too weakly nor too strongly.[26] If the catalyst binds O too weakly on its surface, the possibility for ORR to occur will be limited. On the other hand, if the catalyst binds OH too strongly on its surface, the availability of active sites on the catalyst surface will be reduced. As a result, a volcano plot is normally observed when plotting the catalytic activity for ORR as a function of the calculated O adsorption energy (or the position of the d-band center). An ideal catalyst for ORR must keep an optimal balance between retaining O on the surface and removing OH from the surface. These studies proposed that the Pt surfaces modified by subsurface transition metals (such as Ni, Co, or Fe) would exhibit better catalyst performance for ORR than pure Pt because the weaker adsorption of OH on these surfaces could improve the availability of the active sites of the catalysts.[8,9] This theoretical argument supports well the systematic experimental measurements for various Pt alloy catalysts.[10,12] However, previous DFT calculations focused primarily on the heat of reactions for various elementary reactions of ORR. In this work, we calculated not only the heat of reactions but also the activation energy of all possible ORR elementary reactions on the surface of catalysts. In this way, we were able to gain further insights into the mechanism of ORR on the catalyst surfaces.

First-principle DFT calculations with a climbing image nudged elastic band (CI-NEB) method could be used to find the transition state of chemical reactions.[27,28] This computational approach has already been employed to determine the activation barriers of some elementary steps (such as O_2 dissociation, O protonation, O_2 protonation, and OH protonation) of ORR catalyzed by pure Pt.[29–31] For instance, the activation energy for direct O_2 dissociation was predicted to be about 0.27 eV on a $2\sqrt{3} \times 4$ surface cell (representing a low O coverage) but about 0.52 eV on a $\sqrt{3} \times 2$ surface cell (representing a high O coverage) of Pt(111) under vacuum conditions, indicating a strong dependence of the direct O_2 dissociation process on oxygen coverage.[29] In addition, the activation energy for direct O_2

dissociation reaction had been shown to be affected by the existence of acid electrolyte,[30] co-adsorbed sodium and water,[31] or electrode potential.[32] Yielding kinetic information of ORR on the catalyst surface, first-principle transition state calculations have also been successfully used to evaluate the catalytic activity of coreshell particles with a series of core metals[33] and elucidate the mechanism of ORR on the surface of different transition metals.[34]

In this work, we used first-principle DFT method to calculate the heat of reaction and activation energy of all possible elementary reactions of ORR on pure Pt (111) surface as well as Pt (111) mono-layer surfaces modified by subsurface transition metal Ni, Co, or Fe. Thus, we probed the ligand (chemical alloying) effect of the subsurface transition metals on the activity for ORR on the Pt monolayer (or skin) catalysts. In particular, we focused on elucidating how O–O bond scission process and O–H bond formation process could be tailored to improve the rate of ORR through modifying the electronic structure of the Pt surface with subsurface transition metals. It notes that the similar surface composition (a pure Pt outermost layer over a transition metal enriched subsurface layer) could be readily acquired through annealing process that promotes Pt segregation to the outermost layer of many Pt alloys.[57–59]

6.3 COMPUTATIONAL METHODS

The first-principle DFT calculations in this study were performed using the Vienna Ab-initio Simulation Package (VASP) code.[71,72] In all the calculations, we used ultrasoft pseudopotentials[121] and a kinetic energy cutoff of 400 eV to expand the electronic wave functions in the plane-wave basis. The generalized gradient approximation with Perdew-Wang 91 functional[42] was used for evaluating exchange-correlation energy. Spin-polarization was included in all the DFT calculations. We have used a $5 \times 5 \times 1$ Monkhorst-Pack k-point mesh[75] for k-space integration in our surface slab calculations. Fully-optimized surface structures and adsorption configurations were obtained by reducing the Hellman-Feynman force acting on each ion to less than 0.01 eV/Å. The transition states of reactions were located using the

climbing image nudged elastic band (CI-NEB) method[27], in which all the force components perpendicular to the tangent of the reaction pathway were reduced to be less than 0.05 eV/Å.

Pure bulk Pt has a face-centered cubic lattice structure, whose lattice parameter was determined to be 3.99 Åin this work. Pure Pt (111) surface was modeled using a slab super-cell containing four layers of the Pt atoms and a 12 Å vacuum region. In our model, each atomic layer had four Pt atoms consistent with 2×2 surface cell. Modified Pt (111) surfaces differ from the pure Pt (111) surface by replacing the four subsurface Pt atoms with transition metal atoms. In this work, we modified the subsurface of the Pt (111) surface with Ni, Co, or Fe elements and denoted these modified surfaces as Pt/Ni, Pt/Co, Pt/Fe (111) surfaces. In all the structural optimization calculations, the positions of the atoms in the two top surface layers were allowed to relax while the positions of the atoms in the two bottom surface layers were fixed.

Modeling 1/4 ML adsorption on the surfaces, we placed one adsorbate (H, O, OH, O_2, OOH, H_2O_2, or H_2O) molecule on the (111) surfaces and then optimized the structure of the adsorbate surface system using the DFT method. Binding energy (E_b) of an adsorbate to the surface was calculated as the energy difference between the molecule-surface adsorption system and the system of isolated clean surface and gas molecule. Negative E_b indicates an attractive interaction between the adsorbate and the surface. Thus, negative E_b is a prerequisite for the chemical reaction to take place on the catalyst surface.

From DFT adsorption and transition state calculations, we evaluated the heat of reaction (ΔE) and activation energy (E_a) of various elementary reactions of ORR on the surface of catalysts. ΔE refers to the energy difference between the final state (products) and the initial state (reactants) of a chemical reaction while Ea is defined as the energy difference between the transition state and the initial state of a chemical reaction. In this study, we have included zero-point energy (ZPE) corrections on all the calculated heat of reaction and reaction activation energies. ZPE corrections were calculated as ZPE $= \sum_i \frac{1}{2} h\nu_i$, where h is Planks constant and ν_i is the frequency of the ith vibrational mode of binding molecules. Besides ZPE corrections, quantum tunneling could affect the protonation reactions of ORR at very low temperature. Using the approach suggested in Ref. 127, we estimated that

the tunneling effect were only expected to be significant at the temperature below 155 K. Since the studied catalysts are normally used at about 350 K in PEMFC, we neglected the quantum tunneling corrections in this study.

6.4 ADSORPTION OF ORR INTERMEDIATES

In this work, we first determined the relaxed adsorption configurations and the corresponding binding energies for all the chemical species (namely, H, O, O_2, OH, H_2O, OOH, and H_2O_2) involved in the three possible ORR mechanisms on the pure Pt and modified Pt/M (111) surfaces. For each chemical species, we examined its optimized adsorption configurations at various possible sites on the (111) surfaces and then identified its lowest-energy adsorption configuration. The possible adsorption sites on the (111) surface of an face-centered cubic crystal include top (right on the top of a surface atom), fcc (center of the triangle formed by three neighboring surface atoms and having no atom right beneath in the subsurface layer), hcp (center of the triangle formed by three neighboring surface atoms and having an atom right beneath in the subsurface layer), and bridge (middle point of two adjacent surface atoms) sites. In Table 6.1, we listed our calculated lowest binding energies and the site preferences of various chemical species on the pure Pt and modified Pt/M (111) surfaces. In addition, some lowest-energy adsorption configurations were graphically shown in Figure 6.1 using atomic structures.

For 1/4 ML coverage of atomic H on the Pt and Pt/M (111) surfaces, our DFT calculations indicated that the binding energy of H at a top site was higher than that at an fcc site by less than 0.002 eV. Hence, both the top and fcc sites could be considered as the most favorable location for H adsorption on the catalyst surfaces in this work. In fact, previous theoretical study has already pointed out that H atom could bind to Pt (111) surface more strongly at a top site than an fcc site for a 3 layer surface slab model but vice versa for a 5 layer surface slab model. The observed low activation energy barrier for H diffusion on Pt (111) surface[128,129] also suggested that H atom could easily hop between different top and fcc sites. In contrast, the solely most energetically favorable configuration for atomic

Table 6.1: Calculated binding energies of different ORR chemical species on pure Pt and modified Pt (Pt/Ni, Pt/Co, and Pt/Fe) (111) surfaces.

		Pt	Pt/Ni	Pt/Co	Pt/Fe
species	site		Binding energies (eV)		
H	top	−2.74	−2.52	−2.45	−2.38
H	fcc	−2.74	−2.52	−2.45	−2.38
O	fcc	−3.96	−3.51	−3.39	−3.20
OH	bridge	−2.23	−1.98	−2.05	−1.94
OH	top	−2.22	−2.00	−2.06	−1.94
O_2	bridge	−0.69	−0.32	−0.32	−0.22
OOH	bridge	−1.15	−0.91	−0.95	−0.83
H_2O_2	bridge	−0.37	−0.29	−0.32	−0.28
H_2O	top	−0.25	−0.20	−0.22	−0.19

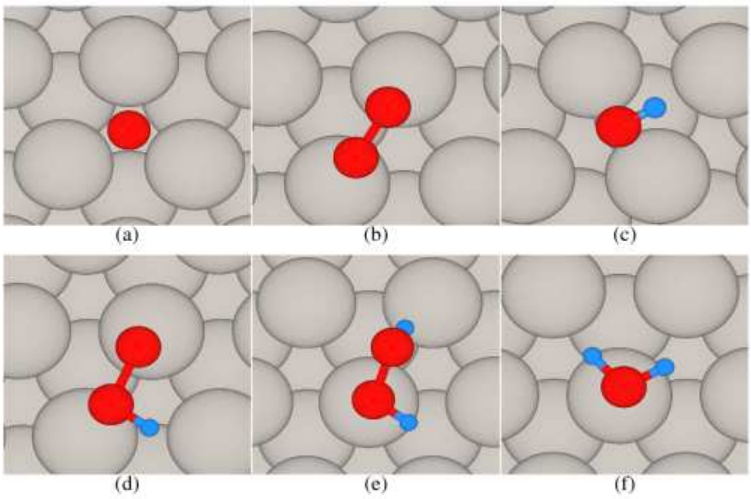

Figure 6.1: Atomic structure of the lowest-energy configuration for various adsorbates on Pt (111) surface.

O adsorbed on the surfaces is the adsorption of O at an fcc site. Moreover, we found that the binding energies were very close (±0.02 eV) for OH molecule adsorbed at a bridge site (see Figure 6.1(c)) or a top site of the surfaces. Hence, we considered both cases as the lowest-energy configurations of OH on the surfaces.

It was found that O_2 molecule prefers binding to the surface at a bridge site with its two O atoms pointing to the two adjacent surface atoms. Similar as O_2, OOH molecule would be favorably adsorbed at a bridge site with its O–H bond tilting away from the surface as shown in Figure 6.1(d).

Figure 6.1(e) shows that when adsorbed on the surface H_2O_2 molecule adopts a twisted configuration in which one O–H bond points downward to a surface atom and the other O–H bond extends toward a nearby hcp site. H_2O molecule was found to be favorably adsorbed at a top site with its O end down and the whole molecular plane nearly parallel to the surface.

6.5 TRANSITION STATES OF ELEMENTARY ORR STEPS

Using the CI-NEB method implemented in VASP, we determined the minimum energy path (MEP) and located the transition states for various elementary steps (summarized in Figure 1.3) of ORR. Specifically, we studied the O_2 dissociation, OOH dissociation, and H_2O_2 dissociation reactions for O–O bond scission process (see Figure 6.2) as well as the O_2 protonation, OOH protonation, O protonation, and OH protonation reactions for hydrogen association process (see Figure 6.3) of ORR on the pure Pt and modified Pt/M (M = Ni, Co, Fe) (111) surfaces. For each elementary reaction, we started from the lowest-energy adsorption configuration of the reactants on the surface (initial state), ended to the lowest-energy adsorption configuration of the products on the surface (final state), and identified the transition state as the highest-energy configuration in a linear transition path from the initial state to the final state. In Table 6.2, we listed our calculated heat of reaction (ΔE) and activation energies (E_a) for the seven elementary steps in ORR on the Pt and Pt/M (111) surfaces.

For O_2 dissociation reaction (shown in Figure 6.2(a)), the initial state is the adsorption

Table 6.2: Calculated heat of reaction (ΔE) and activation energy (E_a) (in unit of eV) for various elementary steps of ORR on Pt (111) and Pt/M (111) (M = Ni, Co, or Fe) surface.

Reactions	Pt		Pt/Ni		Pt/Co		Pt/Fe	
	ΔE	E_a	ΔE	E_a	ΔE	E_a	ΔE	E_a
O–O bond scission								
$O_2^* \longrightarrow O^* + O^*$	−1.02	0.63	−0.65	0.83	−0.34	0.87	−0.17	1.07
$OOH^* \longrightarrow O^* + OH^*$	−1.51	0.05	−1.14	0.32	−1.00	0.31	−0.83	0.40
$H_2O_2^* \longrightarrow OH^* + OH^*$	−1.75	0.26	−1.39	0.08	−1.46	0.10	−1.35	0.07
Protonation								
$O_2^* + H^+ + e^- \longrightarrow OOH^*$	−0.14	0.25	−0.60	0.15	−0.66	0.17	−0.79	0.16
$OOH^* + H^+ + e^- \longrightarrow H_2O_2^*$	−0.28	0.19	−0.79	0.07	−0.84	0.12	−1.03	0.07
$O^* + H^+ + e^- \longrightarrow OH^*$	−0.14	0.79	−0.66	0.57	−0.93	0.46	−1.13	0.34
$OH^* + H^+ + e^- \longrightarrow H_2O^*$	−0.70	0.09	−1.27	0.04	−1.24	0.06	−1.46	0.03

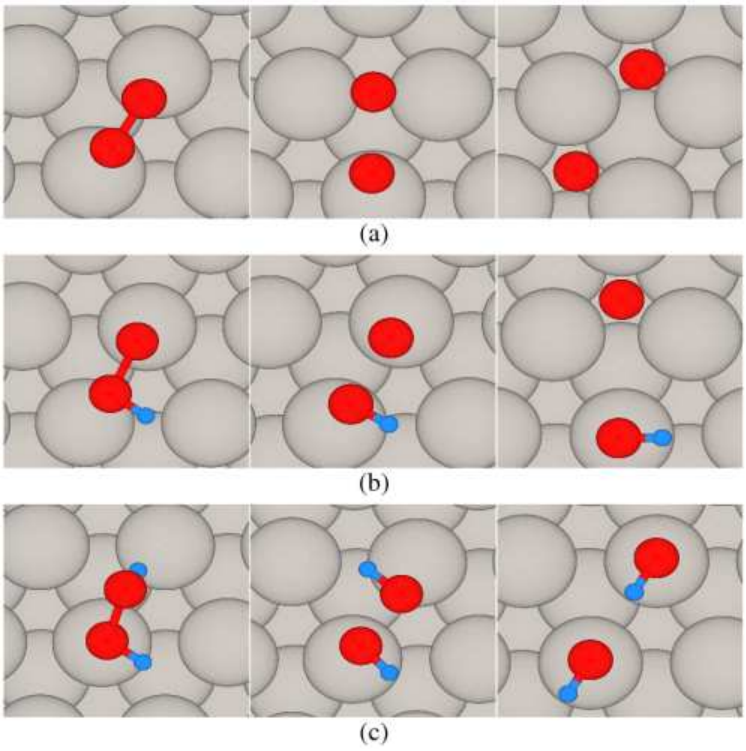

Figure 6.2: Atomic structures of the initial state (left panel), transition state (middle panel), and final state (right panel) for dissociation reactions.

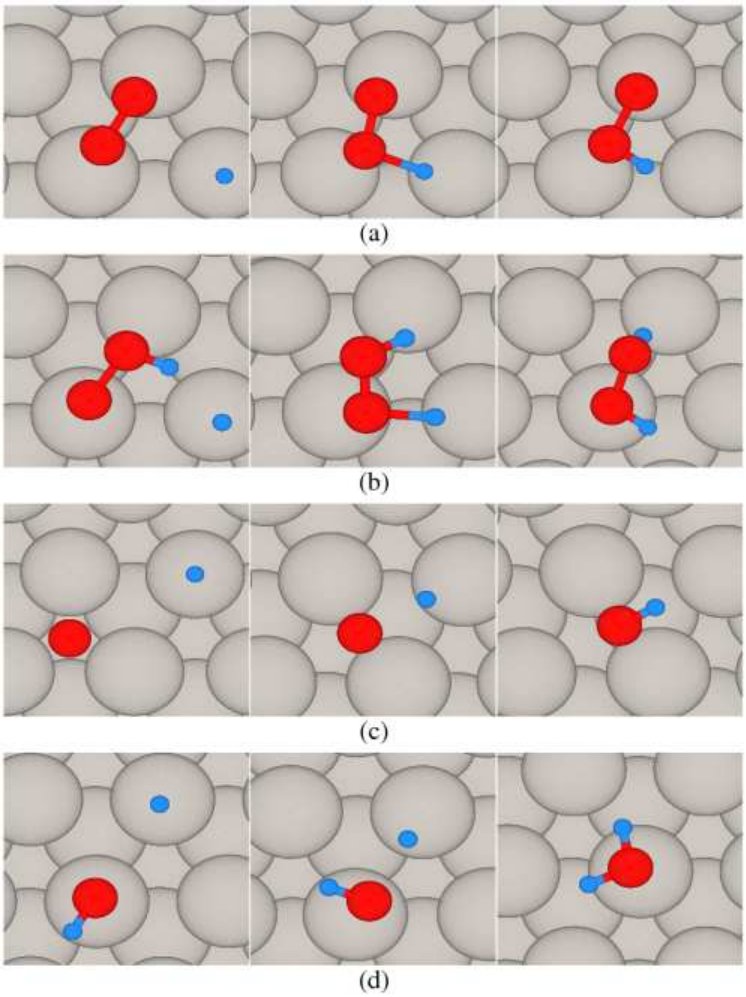

Figure 6.3: Atomic structures of the initial state (left panel), transition state (middle panel), and final state (right panel) for hydrogenation reactions

of O_2 at a bridge site while the final state is the adsorption of two separated O atoms (both at fcc sites) on the surface. In its transition state, one O atom just lies at a bridge site during its motion to the nearby fcc site.

For OOH dissociation reaction (shown in Figure 6.2(b)), the initial state is the adsorption of OOH molecule at a bridge site on the surface while the final state is the adsorption of the separated O atom at an fcc site and OH molecule at a top site. In the transition state, the separated O atom gets near to the closest top site in its motion to the nearby fcc site.

For H_2O_2 dissociation reaction (shown in Figure 6.2(c)), the initial state is the adsorption of H_2O_2 molecule at a bridge site with a twisted configuration on the surface while the final state is the adsorption of two OH molecules on the top sites and with both O–H bonds pointing to the same direction. In the transition state, the two O–H bonds of the H_2O_2 molecule are parallel to the surface and point to opposite directions.

For O_2 protonation reaction (shown in Figure 6.3(a)), the initial state is the co-adsorption of an O_2 molecule at a bridge site and an atomic H at a nearby top site. In the final state, these two species associate with each other and form an OOH molecule absorbed at a bridge site. In the transition state, the O_2 molecule tilts on the (111) surface and extends one O end to interact with the H atom.

For OOH protonation reaction (shown in Figure 6.3(b)), the initial state is the co-adsorption of an OOH molecule at a bridge site and an atomic H at a nearby top site on the surface. These two species would react to form a H_2O_2 molecule adsorbed at a bridge site in the final state. In the transition state, the two species move close to each other and start to form an O–H bond.

For O protonation reaction (shown in Figure 6.3(c)), the initial state is the co-adsorption of an O atom at an fcc site and a H atom at an adjacent top site while the final state is the adsorption of the formed OH molecule at a bridge site. In the transition state, the O atom lies at a bridge site and attracts the H atom moving out of its initial top site on the surface.

For OH protonation reaction on the (111) surface (shown in Figure 6.3(d)), the initial state is the co-adsorption of OH and H at the adjacent top sites and the final state is the adsorption of H_2O molecule at a top site. In the transition state, the OH molecule rotates by about 60° on the surface while the H atom moves closer to the OH from its initial top site.

Our results in Table 6.2 for pure Pt (111) surface are in good agreement with previous DFT calculations.[34] It is noticeable in Table 6.2 that the activation energy of the OOH dissociation reaction is much smaller than that of the O_2 dissociation reaction on the pure Pt (111) surface. Although the peroxyl dissociation mechanism has an extra O_2 protonation step as compared with the oxygen dissociation mechanism (shown in Figure 1.3), the activation energy for this additional step was found to be 0.25 eV which was not as pronounced as the

activation energy difference (0.58 eV) between the OOH dissociation and O_2 dissociation reactions on the Pt (111) surface. Consequently, our DFT study suggested that it was more possible for ORR on the Pt (111) surface to proceed following the peroxyl dissociation mechanism than the direct oxygen dissociation mechanism. On the other hand, the activation energy (0.19 eV) of the OOH protonation reaction is about four times larger than that (0.05 eV) of the OOH dissociation reaction on the Pt (111) surface. It infers that OOH molecule would energetically favor dissociation reaction than protonation reaction once it is formed on the Pt (111) surface. Thus, our DFT study also suggested that it was more possible for ORR on the Pt (111) surface to proceed following the peroxyl dissociation mechanism than the hydrogen peroxide dissociation mechanism. Among the five elementary steps of ORR in the peroxyl dissociation mechanism (see Figure 1.3), the step of O protonation to form OH was predicted to have the highest activation energy of 0.79 eV and hence be the rate-determining (or bottleneck) of ORR on the pure Pt (111) surface in this work. Other work has found that this prediction held true even after considering solvation effect.[130]

6.6 MODIFICATION OF ORR REACTION ENERGETICS BY SUBSURFACE TRANSITION METALS

Our DFT calculation results in Table 6.1 and Table 6.2 show clearly subsurface transition metals would affect both the heat of reaction and activation energy of ORR occurring on the outermost Pt monolayer of the Pt/M (M = Ni, Co, and Fe) (111) surfaces. This effect can be attributed to the change in the electronic structure of the outermost Pt layer modified by the subsurface transition metals. In this work, we determined the *d*-band center (defined as the first moment of the surface *d*-band with respect to the fermi energy[14,131]) of the outermost Pt (111) surface layer to be −2.41 eV for the pure Pt surface, −2.58 eV for the Pt/Ni surface, −2.70 eV for the Pt/Co surface, and −2.80 eV for the Pt/Fe surface. Thus, the subsurface Ni, Co, and Fe were found to down-shift the *d*-band center of the surface Pt. It has been reported that the binding energy of adsorbates to metal surfaces was strongly correlated with the position of the *d*-band center of the outermost surface layer and a down-

shift in the *d*-band center would lead to weaker surface adsorption.[15,16] Well agreeing with this prediction, our results in Table 6.1 shows that the binding energy of small species (H and O atoms) to the surfaces decreases with the lowing location of their *d*-band centers (the lower the *d*-band center is, the weaker the binding energy is). However, the binding energies of large species (OH, O_2, OOH, H_2O_2, and H_2O molecules) to different surfaces do not vary exactly corresponding to the change of their *d*-band centers. Nevertheless, the modification of Pt (111) surface with the subsurface Ni, Co, or Fe could lead to weaker binding of all the species involved in ORR as compared with that on the pure Pt (111) surface.

Subsequently, the heat of reaction (ΔE, the energy difference between the lowest-energy adsorption configurations of products and reactants) of ORR elementary steps will be affected by the subsurface transition metals. It is noticeable from our results in Table 6.2 that as compared with pure Pt the subsurface Ni, Co, and Fe would increase the heat of reaction of all the three possible O–O bond scission reactions but decrease the heat of reaction of all the four possible hydrogenation reactions. The last step of the three proposed mechanisms for ORR (see Figure 1.3) is the OH hydrogenation reaction, which has lower ΔE on the Pt/M (111) surfaces than on the pure Pt (111) surface. It implies that the subsurface Ni, Co, or Fe made the conversion of OH to H_2O on the Pt mono-surface layer more energetically favorable and thus removed OH from the catalyst surfaces more rapidly. This has been believed to be a main reason accounting for the observed activity enhancement for ORR on the Pt surface segregated Pt_3Ni alloy.[12]

Moreover, the activation energy (E_a) of ORR elementary reactions will be affected by the subsurface transition metals. It has been summarized as Brønsted-Evans-Polanyi (BEP) relationship that the activation energy of a reaction will most often be linearly related to its heat of reaction[132–134], namely, more negative ΔE is normally associated with less positive E_a of a reaction. It was found in 6.2 that the O_2 protonation, OOH protonation, O protonation, and OH protonation reactions had lower E_a (associated with a decrease in ΔE) on the Pt/M (M = Ni, Co, or Fe) than the pure Pt (111) surfaces while the O_2 dissociation and OOH dissociation reactions had higher E_a (associating with an increase in ΔE) on the Pt/M than the pure Pt (111) surfaces. Thus, our these DFT calculation results are quite consistent with BEP relationship.

Contrary to BEP relationship, E_a of the H_2O_2 dissociation reaction decreases with an increase of ΔE on the Pt/M (M = Ni, Co, or Fe) (111) surfaces as compared with those values on the pure Pt (111) surface. It is noticed that the H_2O_2 dissociation reaction (see Figure 6.2(c)) involves a rotation of O–H bond on the surface of the catalysts. Conceivably, the energy required to rotate O–H bond would be small if the OH molecule bind weakly to the surface. Therefore, we believed that the weaker binding of OH molecule to the Pt/M (111) surfaces facilitates the O–H bond rotation and thus lowers the total energy barrier for the H_2O_2 dissociation on the Pt/M (111) surfaces than the pure Pt (111) surface.

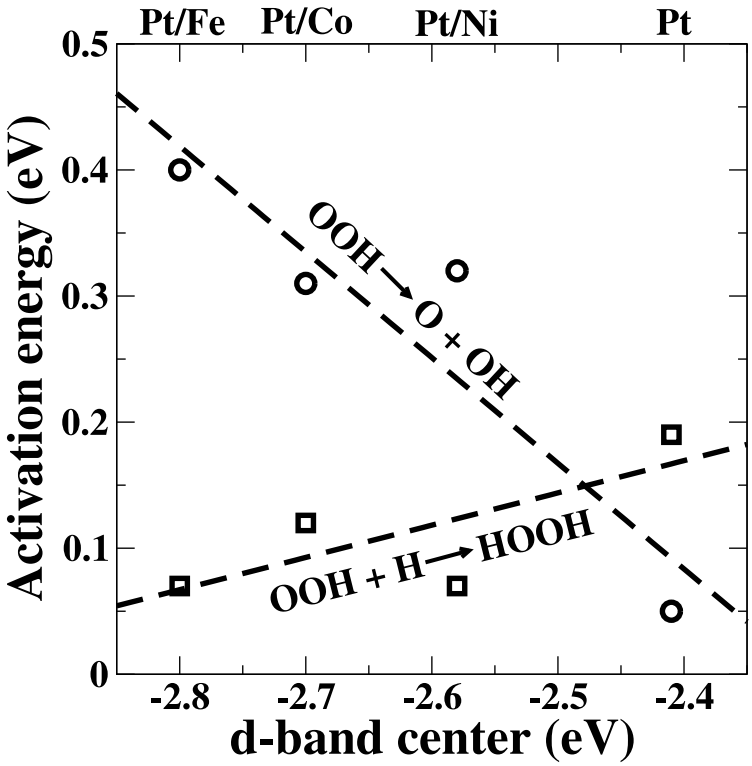

Figure 6.4: Variation of the activation energies of OOH dissociation reaction (circles) and OOH protonation (squares) reaction on Pt (111) and Pt/M (111) (M = Ni, Co, Fe) surfaces with respect to the *d*-band centers of these surfaces.

6.7 MODIFICATION OF ORR REACTION MECHANISM BY SUBSURFACE TRANSITION METALS

As discussed in section 6.5, our DFT calculation results suggested that ORR on the pure Pt (111) surface would proceed following the peroxyl dissociation mechanism and have a rate-determining step of the O protonation reaction whose activation energy was predicted to be 0.79 eV in this work. If ORR also proceeds following the peroxyl dissociation mechanism on the modified Pt/M (M = Ni, Co, or Fe) (111) surfaces, the rate-determining step would still be the O protonation reaction (see data in Table 6.2). However, the activation energy for this rate-determining step would respectively decrease by 0.22 eV (28 %), 0.33 eV (42 %), and 0.45 eV (57 %) on the Pt/Ni, Pt/Co, and Pt/Fe (111) surface than the pure Pt (111) surface. Lowering activation energy for the rate-determining step implies faster ORR on these catalysts surfaces. Therefore, this theoretical result is apparently consistent with experimental observations that Pt surface-segregated PtNi, PtCo, and PtFe alloy catalysts would have enhanced activity for ORR than pure Pt.[8,12,13] However, our DFT results also pointed out that as compared to that on the pure Pt surface the activation energy of the OOH dissociation reaction would increase by 0.27 eV, 0.26 eV, and 0.35 eV on the Pt/Ni, Pt/Co, and Pt/Fe (111) surfaces respectively. It implies that this OOH dissociation reaction could slow-down the ORR on the modified Pt/M (111) surfaces. Therefore, our DFT results do not explain well why multi-fold activity enhancement could be achieved on PtNi, PtCo, and PtFe alloy catalysts as compared with pure Pt if ORR always proceeds through the peroxyl dissociation mechanism.

Furthermore, we investigated the scenario that ORR mechanism might change on the Pt/M (111) surfaces. Our DFT results in Table 6.2 indicated that the direct oxygen dissociation mechanism was not viable for ORR on the modified Pt/M (111) surfaces due to the rather high activation energy for the O_2 dissociation reaction on these surfaces. On the pure Pt (111), the activation energy of OOH dissociation reaction is lower than that of OOH protonation reaction. However, the subsurface transition metal Ni, Fe, and Fe were found in this work (see Figure 6.4) to be able to cause the activation energy of the OOH dissociation reaction higher than that of the OOH protonation reaction. Consequently, our theoretical

study suggested that ORR would take the hydrogen peroxide dissociation route rather than the peroxyl dissociation route on the Pt/M (M = Ni, Co, or Fe) (111) surface. Provided following the hydrogen peroxide dissociation mechanism, the rate-determining step of ORR would be the O_2 protonation reaction whose activation energy was calculated to be 0.15 eV on the Pt/Ni surface, 0.17 eV on the Pt/Co surface, and 0.16 eV on the Pt/Fe surface. Thus, the multi-fold activity enhancement of ORR on PtNi, PtCo, and PtFe alloy catalysts compared to pure Pt could be explained as that ORR proceeds through the hydrogen peroxide dissociation mechanism on the modified Pt/M (M = Ni, Co, or Fe) (111) surfaces with an activation energy of about 0.16 eV for its rate-determining reaction step while through the peroxyl dissociation mechanism on the pure Pt (111) surface with an activation energy of 0.79 eV for its rate-determining reaction step.

6.8 EFFECTS OF ELECTRIC POTENTIAL ON ORR

In above, we discussed the heats of reactions and activation energies of ORR under zero electrode potential condition. In fact, cathode electrocatalysts are subjected to positive electric potential in working PEMFC. Hence, the effects of the electric potential on the energetics and mechanisms of ORR have also been investigated in this work. Among the elementary reactions of ORR, the O_2 dissociation, OOH dissociation, and H_2O_2 dissociation reactions (i.e. O–O bond scission process) do not involve electron transfer. As a result, the heats of reaction and activation energies of these three reactions are not expected to be affected by the positive electrode potential. On the other hand, one electron will transfer from the electrode to the protonated species in the O_2 protonation, OOH protonation, O protonation, and OH protonation reactions (i.e. hydrogen association process). To address the effect of electric potential, Nørskov et al[26] proposed to express the free energy landscape of the adsorbed ORR intermediates as a function of the electric potential and thus linked the proceeding of the ORR on the surface of electrocatalysts with the variation of the electrode potentials. When electrode potential is zero, all the elementary reactions of ORR are exothermic and could proceed as listed for the three ORR mechanisms in Figure 1.3. With the increase of

electrode potential U, the free energy of the adsorbed O_2, OOH, H_2O_2, O, and OH molecules would be reduced by $4eU$, $3eU$, $2eU$, $2eU$, and eU respectively. Consequently, there exists a highest electrode potential under which all the elementary reactions are still exothermic for the assumed ORR mechanism on the surface of catalysts. This critical potential actually defines the working potential of the electrocatalyst. Above the working potential, some elementary reaction of ORR would have positive reaction free energy change and thus require high activation energy on the catalyst surfaces. Following the proposed computation approach,[26] we found that the working potentials of the pure and modified Pt (111) surfaces were determined by the free energy change between the adsorbed O and OH in the direct oxygen dissociation mechanism and by the free energy change between the adsorbed O_2 and OOH in the peroxyl dissociation mechanism and the hydrogen peroxide dissociation mechanism.

Table 6.3: Calculated working electrode potential (in unit of V) of Pt (111) and Pt/M (111) (M = Ni, Co, Fe) surface for ORR by assuming the three different mechanisms. The values in the table are the relative working electrode potential with respect to that of the pure Pt (111) surface following the oxygen dissociation mechanism.

	Pt	Pt/Ni	Pt/Co	Pt/Fe
oxygen dissociation	0.00	0.24	0.42	0.49
peroxyl dissociation or hydrogen peroxide dissociation	−0.02	0.12	0.19	0.12

In Table 6.3, we gave the calculated relative working potentials of the Pt and Pt/M (111) surfaces with respect to the working potential of the pure Pt (111) surface under the oxygen dissociation mechanism. Our calculation results showed that, the working potentials of the Pt (111) surface were nearly equal but that of the Pt/M (111) surfaces differed appreciably for the three ORR mechanisms. Moreover, the working potentials of the Pt/M (111) surfaces shifted toward more positive values as compared with that of the Pt (111) surface. This is consistent with the electrochemical measurements on the Pt_3Ni alloys catalysts.[12]

Moreover, we would like to discuss under electric potentials which mechanism of ORR (the peroxyl dissociation or hydrogen peroxide dissociation mechanism) is more preferable on the Pt and Pt/M (111) surfaces. If the activation energy of the OOH dissociation reaction is lower than that of the OOH protonation reaction (like ORR on the Pt (111) under zero electric potential), then the peroxyl dissociation on mechanism is kinetically preferred. Otherwise (like ORR on the Pt/M (111) under zero electric potential), the hydrogen peroxide dissociation mechanism is kinetically preferred. As mentioned above, the increasing electric potentials have no effect on the OOH dissociation reactions but would make the OOH protonation reaction more difficult. Consequently, the ORR on the Pt (111) surface will always assume the peroxyl dissociation mechanism below its working potential. To estimate the change of the activation energy of the OOH protonation step under the electric potential, we first linearly fitted the heats of reaction and activation energies of this reaction on the Pt and Pt/M (111) surfaces (data given in Table 6.2) based on the BEP relationship. Then, we extrapolated the fitted line to obtain the value corresponding to zero heat of reaction, which sets an upper limit to the change of the reaction activation energy under working potential of the electrodes. In this way, we predicted the activation energy of the OOH protonation reaction with zero heat of reaction to be 0.23 eV, still lower than those values for the OOH dissociation reaction on the Pt/M (111) surfaces. Consequently, it infers that even under electric potentials the ORR would proceed following the peroxyl dissociation mechanism on the Pt (111) surface and the hydrogen peroxide dissociation mechanism on the Pt/M (M = Ni, Co, Fe) (111) surfaces. Moreover, we employed the BEP relationship to determine the activation energy at zero heat of reaction to be 0.26 eV for the O_2 protonation reaction, 0.86 eV for the O protonation reaction, and 0.15 eV for the OH protonation. Thus, the O_2 protonation reaction is still the rate-determining step in the hydorgen peroxide dissociation mechanism and the O protonation reaction is still the rate-determining step in the peroxyl dissociation mechanism. Therefore, our analysis above suggests that although the positive electrode potential in the electrochemical environment causes changes in reaction energetics, it does not alter the assumed mechanism and the type of the corresponding rate-determining step for the ORR on the pure Pt and modified Pt/M (M = Ni, Co, Fe) (111) surfaces.

6.9 CONCLUSION

In this work, we employed first-principle DFT method to study the influence of the subsurface transition metals (M = Ni, Co, or Fe) on ORR occurring on the outermost Pt (111) monolayer. To this end, we first determined the lowest-energy configurations of H, O, O_2, OH, H_2O, OOH, and H_2O_2 adsorbed on the pure Pt and the modified Pt/M (111) surfaces. Then, we used these lowest-energy configurations to construct the initial and final states of various elementary steps of ORR on these surfaces. The ORR elementary steps studied here include O_2 dissociation, OOH dissociation, and H_2O_2 dissociation reactions for O–O bond scission process as well as O_2 protonation, OOH protonation, O protonation, and OH protonation reactions for hydrogen association process. Furthermore, we located the transition states and calculated the corresponding activation energies of these elementary steps of ORR using nudged elastic band method.

We found from our DFT calculations that the subsurface Ni, Co, or Fe could modify the electronic structure of the outermost Pt monolayer in down-shifting its *d*-band center. As a consequence of this effect, the binding of various chemical species becomes weaker to the Pt/M (111) surface than the pure Pt (111) surface. The weaker binding of ORR intermediates on the Pt/M (111) surfaces leads to higher heat of reaction for the three reactions of O–O bond scission process but lower heat of reaction for the four reactions of hydrogen association process as compared to those of the corresponding reactions on the Pt (111) surface. It is generally believed that for a reaction the activation energy is directly proportional to the heat of reaction. Thus, the activation energy of the OOH dissociation turns out to be higher on the Pt/M (111) surfaces than the pure Pt (111) surface. Conversely, the activation energy of the OOH protonation becomes lower on the Pt/M (111) surfaces than the pure Pt (111) surface. Our calculation results indicated that this effect could cause the hydrogen peroxide dissociation mechanism for ORR becomes viable on the Pt/M (111) surfaces. In contrast, the peroxyl dissociation mechanism is the most possible route for ORR to proceed on the pure Pt (111) surface.

Another outcome resulting from the weaker binding of ORR intermediates on the Pt/M (111) surfaces is that it requires less energy to rotate O–H bond on the Pt/M (111) surfaces

than the Pt (111) surface. When H_2O_2 dissociates into two OH molecules, one O–H bond initially pointing downward to a top site would rotate on the surface to be finally parallel to the surface. Owing to weak surface binding and hence easy O–H bond rotation, the activation energy of the H_2O_2 dissociation reaction were found to be even lower on the Pt/M (111) surfaces than the Pt (111) surface. This is quite significant because it implies that the breaking of O–O bond could be readily accomplished through H_2O_2 dissociation and would not be a rate-determining step for ORR on the Pt/M (111) surfaces.

Moreover, our DFT results in Table 6.2 pointed out that the rate-determining step for ORR through the peroxyl dissociation mechanism on the Pt (111) surface would be the O protonation reaction with an activation energy of 0.79 eV. In contrast, the rate-determining step for ORR through the hydrogen peroxide dissociation mechanism would be the O_2 protonation reaction with an activation energy of 0.15 eV on the Pt/Ni (111), 0.17 eV on the Pt/Co (111), and 0.16 eV on the Pt/Fe (111) surfaces. It infers that the rate of ORR on the modified Pt/M (M = Ni, Co, or Fe) surfaces could be multi-fold faster than that on the Pt (111) surface. Here, our theoretical results are in excellent agreement with experimental measurements.[8,12,13] Furthermore, we estimated the effect of electric potentials on the energetics of the ORR reactions and concluded the positive electrode potential would alter neither the assumed reaction mechanism nor the rate-determining step for ORR on the Pt and Pt/M (111) surfaces.

Therefore, our theoretical study in this work reveals new insight into how subsurface transition metals would modify the electronic structure and further catalytic activity of the outermost Pt monolayer surfaces. The attained knowledge will be useful for designing and fabricating Pt alloys as high-performance electro-catalysts in PEMFCs.

7.0 COMPARISON OF REACTION ENERGETICS FOR OXYGEN REDUCTION REACTIONS ON PLATINUM (100), PLATINUM (111), PLATINUM/NICKEL (100), AND PLATINUM/NICKEL (111) SURFACES: A FIRST-PRINCIPLES STUDY

7.1 ABSTRACT

In this study, we calculated the reaction energetics (including surface adsorption energy, heat of reaction, and activation energy) of oxygen reduction reactions (ORR) on Pt(100) and Pt/Ni(100) surfaces using firstprinciples density functional theory methods. Our calculation results suggest that, on the Pt and Pt/Ni(100) surfaces, the ORR would proceed following direct oxygen dissociation mechanism in which the rate-determining step is OH hydrogenation reaction. Furthermore, we compared the calculated reaction energies of the ORR on the Pt(100), Pt(111), Pt/Ni(100), and Pt/Ni(111) surfaces. Our results indicated that the subsurface Ni atoms would weaken the strength of various ORR chemical intermediates binding to the outermost Pt monolayers and further cause an increase in the heats of reaction for all the O–O bond dissociation reactions but a decrease in the heats of reaction for all the hydrogenation reactions of the ORR on the Pt/Ni surfaces as compared to the pure Pt surfaces. However, we found that the extent of such ligand effect was more pronounced on the (111) surfaces than the (100) surfaces. Moreover, we determined the activation energy for the rate-determining step of the ORR on the Pt(100) to be 0.80 eV, on the Pt/Ni(100) to be 0.79 eV, on the Pt(111) to be 0.79 eV, and on the Pt/Ni(111) to be 0.15 eV. Consequently, our study predicted that the catalytic activity for the ORR should be higher on the (111) surfaces than the (100) surfaces and would be much higher on the Pt/Ni(111) than all the other three surfaces.

7.2 INTRODUCTION

Proton-exchange membrane (PEM) fuel cells can directly convert chemical energy stored in hydrogen fuels into electricity and thus have potential applications in powering transportation vehicles or portable electronic devices.[126] The performance of PEM fuel cells is strongly dependent on the efficiency of the electrocatalysts employed, especially the cathode catalyst that promotes oxygen reduction reactions (ORR).[135] Among pure metals, precious metal Pt is found to have the best activity for ORR.[3] It has been established that alloying Pt with other transition metals is an effective approach to further enhancing the activity of electrocatalysts for ORR. For example, Adzic et al. deposited Pt monolayers over various transition metal substrates and observed improved catalytic activity for ORR, especially on the Pt monolayer over Pd(111) substrate.[98] Stamenkovic et al. reported that the measured catalytic activities of binary Pt_3M (M = Ni, Co, Fe, Ti, V) alloy electrocatalysts for ORR were much higher than that of polycrystalline Pt catalyst. In particular, single-crystal $Pt_3Ni(111)$ surface could enhance the performance by more than 10 times as compared to pure Pt.[12,13] Luo et al. found that core–shell PtNiFe alloy nanoparticles (with only about 30 atom % Pt) could have almost five times better mass activity than commercial Pt catalyst.[136] In addition, Pt-skin $Pt_3(CoNi)_1$ ternary catalysts were found to have about 3.5 times greater activity than Pt polycrystalline catalyst and even better activity than Pt_3Co catalyst for ORR.[137] It was believed that the observed activity enhancement in the Pt alloy catalysts is mainly due to the modification to the electronic structure of the outermost Pt monolayer by the subsurface transition metals (i.e., ligand effect).[15] In this aspect, Ni, Co, and Fe are found to be most effective alloying elements.[8,13]

Moreover, the activity of metal electrocatalysts can be improved through controlling the shapes of their nanostructures.[138] Such works are stimulated by the experimental findings that the activity of Pt and its alloy catalysts for ORR is dependent on the index of the surfaces, i.e., surface structures. In nonadsorbing $HClO_4$ electrolytes, single-crystal Pt(110), (111), and (100) surfaces were observed to have the activity for ORR following a descending order.[12,139,140] In contrast, it was found that the annealed single-crystal Pt_3Ni (111) surface exhibited the highest activity for ORR among the $Pt_3Ni(111)$, (110), and (100) surfaces.[12]

The most active $Pt_3Ni(111)$ had nearly ten times higher activity than the $Pt_3Ni(100)$ surface. Consequently, it is not surprising that Zhang et al. found that {111}-terminated Pt3Ni nano-octahedra were at least five times more active for ORR than {100}-terminated Pt_3Ni nanocubes,[141] and the specific activity toward ORR on {720}- bounded Pt concave nanocubes was reported to be at least two times higher than that of low-indexed Pt nanocubes and nanocuboctahedra.[142] Similarly, {111}-terminated nanotruncated Pt3Co octahedra had been found to have higher activity than {100}-terminated Pt_3Co nanocubes.[143] In addition, {100}- terminated Pt-Mn nanocubes were reported to have higher ORR activity than the commercial catalyst.[144] It appears that the activity for ORR of various surfaces is closely related to the structures of these surfaces. The Pt and Pt alloy catalysts mentioned above have face-centered cubic (fcc) crystal lattice. In fcc crystal, the atoms in the (111) surface would form hexagonal surface cells and have nine nearest neighboring atoms while the atoms in the (100) surface would form square surface cells and have eight nearest neighboring atoms. It is predicted from density functional theory (DFT) calculations[23,145] that the most stable location for O atom to adsorb is an fcc hollow site (center of the triangle formed by three neighboring surface atoms and having no atom right beneath in the subsurface layer) on the Pt(111) surface, whereas it is a bridge site (middle point of two adjacent surface atoms) on the Pt(100) surface. Therefore, the different geometric structures of the (111) and (100) surfaces would affect the energetics of ORR and lead to the observed surface-sensitive catalytic performance.

In order to elaborate both the ligand and structural effects on influencing the catalytic activity for ORR, we performed first-principles DFT calculations to determine the reaction energetics (i.e., surface adsorption energies, heats of reaction, and activation energies) for all the possible elementary reactions of the ORR on Pt(100), Pt(111), Pt/Ni(100), and Pt/Ni(111) surfaces. Many previous works[23,26,146–149] focused on studying only the adsorption energy of various chemical species (relevant to the ORR) on the surface of catalysts and have yielded valuable information for catalyst design. No doubt, the potential energies of the transition states between these stable states are also quite important as to quantify the kinetics of the elementary steps of the ORR. First-principles transition state calculations have already been employed to elucidate the reaction mechanisms of the ORR on

Pt(111)[29,30,32,34,130,150,151] and Pt alloy (111) surfaces.[18,24,34] For instance, we investigated how the subsurface 3d transition metals (Ni, Co, and Fe) affect the ORR pathway on the Pt(111) outermost monolayers with first-principles transition state calculations in an early work.[2] However, the transition states of the ORR on the (100) surfaces of electrocatalysts have not ever been reported. Hence, in this work, we first calculated the energies of the stable adsorption states and transition states related to the progression of the ORR on Pt(100) and Pt/Ni(100) surfaces and then compared the attained reaction energetics of the ORR on the Pt(100), Pt(111), Pt/Ni(100), and Pt/Ni(111) surfaces to discuss both the ligand and structural effects on the ORR.

7.3 COMPUTATIONAL MODELS AND METHODS

First-principles DFT calculations in this study were performed using the Vienna Ab-Initio Simulation Package (VASP) code.[71,72] In all the calculations, we used ultrasoft pseudopotentials[121] and plane-wave basis set with 400 eV kinetic energy cutoff. The generalized gradient approximation (GGA) with Perdew-Wang 91 functional[42] was used for evaluating exchange-correlation energy. Spin-polarization was included in all the DFT calculations. A $5 \times 5 \times 1$ Monkhorst-Pack k-point mesh[75] was used for k-space integration in our surface calculations. Fully optimized atomic structures were obtained by minimizing the Hellman-Feynman forces acting on each ion to be less than 0.01 eV/Å. The transition states of chemical reactions were located using the climbing image nudged elastic band (CI-NEB) method,[27,28] in which all the force components perpendicular to the tangent of the reaction pathway were reduced to be less than 0.05 eV/Å. Every transition state was verified to have only one imaginary vibrational frequency.

The Pt(100) surface was modeled using a slab model which contains four atomic layers and four atoms at each layer (corresponding to a 2×2 unit cell). A 12 Åthick vacuum was added in the slab model to sufficiently separate adjacent periodic images. In the Pt/Ni(100) surface model, the four subsurface Pt atoms in the Pt(100) surface model were replaced with Ni atoms. Both the Pt(100) and Pt/Ni(100) surface models were constructed based on

bulk fcc Pt crystal whose lattice constant was calculated to be 3.99 Å. In all the structure optimization calculations, the positions of the atoms in the bottom two surface layers were fixed while the positions of all the other atoms were fully relaxed.

In this work, the surface adsorption energy (or binding energy (E_b)) of a molecule adsorbate is defined as the energy difference between the molecule-surface adsorption system and the systems of isolated clean surface and gas molecule. Negative E_b implies that the adsorbate can be stably adsorbed on the surface of the catalysts. Moreover, we evaluated the heats of reaction (ΔH_0) and activation energies (E_a) of various elementary reactions of the ORR on the catalysts' surfaces. ΔH_0 refers to the enthalpy difference between the final state (products) and the initial state (reactants) of a chemical reaction while E_b is defined as the enthalpy difference between the transition state and the initial state of a chemical reaction. In this study, we have included zero-point energy (ZPE) corrections into all the calculated heats of reaction and reaction activation energies. ZPE corrections were calculated as $ZPE = \sum_i 1/2h\nu_i$, where h is Planck's constant and ν_i is the frequency of the ith vibrational mode of the binding molecule.

7.4 COMPUTATIONAL RESULTS

7.4.1 Previous Results of ORR on Pt(111) and Pt/Ni(111) Surfaces

In ref 2, we listed three possible mechanisms (oxygen dissociation, peroxyl dissociation, and hydrogen peroxide dissociation mechanisms) of the ORR on the surfaces of metal catalysts. As shown in Figure 1.3, there are seven kinds of chemical species (H, O, OH, O_2, OOH, H_2O_2, and H_2O), four types of elementary hydrogenation reactions (O_2 hydrogenation, OOH hydrogenation, O hydrogenation, and OH hydrogenation), and three types of elementary dissociation reactions (O_2 dissociation, OOH dissociation, and H_2O_2 dissociation) associated with these three ORR mechanisms. In all the three mechanisms, the ORR on the catalyst surface starts with the adsorption of O_2 molecule and ends with the production of H2O

molecule. Mainly, the three mechanisms differ in through which dissociation reaction (O_2 dissociation, OOH dissociation, and H_2O_2 dissociation) the O-O bond is split.

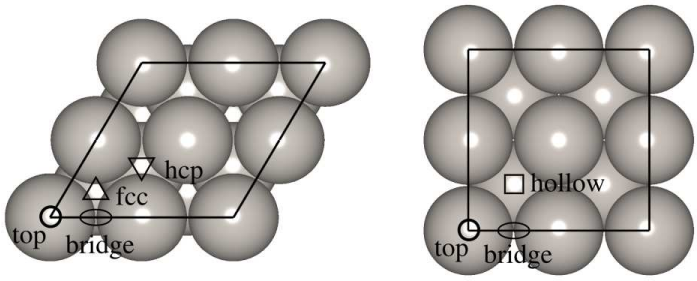

Figure 7.1: Atomic structure of the simulation cell modeling (a) (111) surface and (b) (100) surface.

With DFT structure optimization calculations, we identified that the most stable sites on the Pt(111) and Pt/Ni(111) surface are the top (or fcc) sites for H adsorption, the fcc sites for O adsorption, the bridge (or top) sites for OH adsorption, the bridge sites for O_2 adsorption, the bridge sites for OOH adsorption, the bridge sites for H_2O_2 adsorption, and the top sites for H_2O adsorption.[2] The locations of the top, bridge, and fcc sites on the(111) surface of an fcc crystal are marked in Figure 7.1(a). Moreover, we constructed the initial and final states of various elementary steps of the ORR on the (111) surfaces using these lowest-energy configurations and determined the corresponding transition states using the CI-NEB method. Our theoretical results in ref 2 indicated that as compared to the Pt(111) surface the subsurface Ni in the Pt/Ni(111) surface would down-shift the d-band center of the outermost Pt monolayer and weaken the binding energy of the ORR intermediates to the extent that the ORR adopted a different reaction pathway. On the Pt(111) surface, the ORR was predicted to follow the peroxyl dissociation mechanism with the O hydrogenation reaction (which has activation energy of 0.79 eV) as the rate-determining step. On the Pt/Ni(111) surface, the ORR was predicted to adopt the hydrogen peroxide dissociation mechanism with the O_2 hydrogenation reaction (which has relatively low activation energy of 0.15 eV) as the rate-determining step. Hence, our previous study provided an explanation about why the subsurface Ni could lead to multifold enhancement in catalytic activity for

the ORR on Pt/Ni(111) catalysts with respect to that on pure Pt electrocatalysts. In the following, we apply the same computational approach to studying the preferable mechanism of the ORR on the Pt(100) and Pt/Ni(100) surfaces.

It can be noted that the reaction energetics of the ORR on Pt(111) surfaces had also been studied by other theoretical groups considering the electrochemical conditions such as solvent, thermal entropy, and electrode potential (as elegantly reviewed by Keith et al. in ref 149). Describing the solvent effect with continuum Poisson-Boltzmann theory, Sha et al. found in their DFT calculations that water solvent could induce an increase in the activation energy for O_2 dissociation and OOH dissociation reactions but a decrease in the activation energy for OH formation and H_2O formation reactions on the Pt(111) surface as compared to the corresponding values in gas environment.[130,151] Nevertheless, their results indicated that the ORR would favor the peroxyl dissociation mechanism on the Pt(111) in both gas and solvent environments consistent with our DFT results in gas environment.[130] Moreover, Keith et al. found that, even including both the solvent effects and thermal contributions, the reaction pathway of the ORR on Pt(111) surface would not be qualitatively different from that predicted from gas-phase DFT calculations.[149] Furthermore, the activation energies for the ORR on Pt(111) surface were calculated as a function of electrode potentials using the simulation model with explicit water layers.[32,150] It was found that, with increasing electrode potentials, the activation energy for the hydrogenation reactions would increase while the activation energy for the dissociation reactions would remain constant. These studies suggested that the reaction pathway of the ORR might depend on the electrical potential of the electrode.

7.4.2 Adsorption of Chemical Species on Pt(100) and Pt/Ni(100) Surfaces

As shown in Figure 7.1(b), there are three possible surface sites on the Pt and Pt/Ni (100) surfaces at which chemical species could adsorb. Hence, we calculated the optimized configuration and the binding energy of each ORR intermediate (H, O, OH, O_2, OOH, H_2O_2, and H_2O) adsorbed at all these three possible surface sites on the Pt(100) and Pt/ Ni(100)

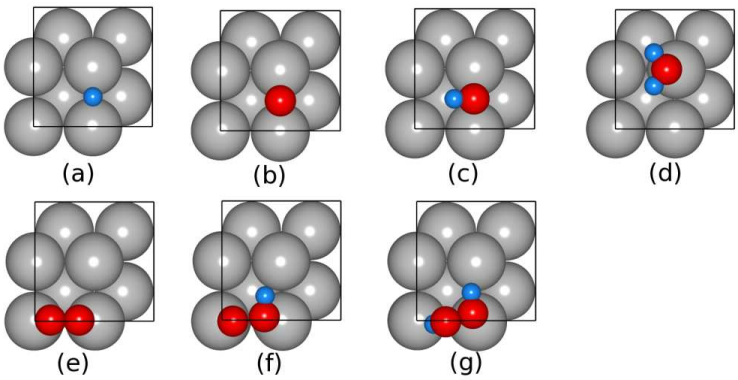

Figure 7.2: Atomic structures of the lowest-energy configuration of various ORR intermediates adsorbed on pure Pt(100) surface.

surfaces. We gave in Table 7.1 the calculated binding energies and plotted in Figure 7.2 the atomic structure of the lowest-energy adsorption configuration of the seven ORR intermediates on the (100) surfaces.

We found rather good agreement when comparing our DFT results with previous experimental and theoretical data. We predicted the lowest binding energy of H at the bridge site of the Pt(100) to be −2.87 eV, which is close to −2.788 eV (−269 kJ/mol) from experimental measurement;[152] the lowest binding energy of OH at the bridge site of the Pt(100) to be −2.78 eV, which is comparable to experimental value −2.86 eV (−276 kJ/ mol).[152] In addition, our results in Table 7.1 reported that the binding energies of atomic O on the Pt(100) surface were −2.92, −3.60, and −4.03 eV at the top, hollow, and bridge surface sites, respectively, with the bridge site being the most energetically favorable adsorption surface site. In comparison, previous DFT calculations using projector-augmented-wave (PAW) method with Perdew-Burke-Ernzerhof (PBE) exchange-correlation functional gave quite close binding energies of −3.054 eV (top site), −3.874 eV (hollow site), and −4.204 eV (bridge site).[145] It was found in our study that O_2 prefers adsorbing at the bridge site with the binding energy of −1.10 eV, which agrees with −1.02 eV from other DFT calculations (with PAW method and GGA-PW91 exchange correlation functional).[147]

Table 7.1: Calculated Binding Energies of Different ORR Chemical Species on Pure Pt and Pt/Ni (100) Surfaces.

		binding energies (eV)	
species	site	Pt	Pt/Ni
H	top	−2.64	−2.55
	hollow	−2.53	−2.55
	bridge	−2.87	−2.82
O	top	−2.92	−3.06
	hollow	−3.60	−3.70
	bridge	−4.03	−3.96
OH	top	−2.34	−2.32
	hollow	−2.31	−2.26
	bridge	−2.78	−2.71
O_2	top	–	–
	hollow	−0.29	−0.21
	bridge	−1.10	−0.91
OOH	top	–	–
	hollow	–	–
	bridge	−1.41	−1.27
H_2O_2	top	–	–
	hollow	–	–
	bridge	−0.39	−0.37
H_2O	top	−0.27	−0.26
	hollow	−0.13	−0.11
	bridge	–	–

Our results in Table 7.1 indicated that the lowest-energy adsorption configuration of the same chemical species would be at the same surface site on both the Pt(100) and Pt/Ni(100)

surfaces. For instance, we calculated the binding energy of atomic H on the Pt(100) surface to be −2.64, −2.53, and −2.87 eV at the top, hollow, and bridge surface sites, respectively. We also calculated the binding energy of atomic H on the Pt/Ni(100) surface to be −2.55, −2.55, and −2.82 eV at the top, hollow, and bridge surface sites, respectively. Hence, the lowest-energy adsorption configuration of H on both the Pt and Pt/Ni(100) surfaces is the adsorption of H atom at the bridge site of the surfaces. Comparing the binding energies of the same chemical species on the Pt(100) and Pt/Ni(100) surfaces, we found that the subsurface Ni in the Pt/Ni(100) surface would weaken the binding of all seven ORR intermediates on the outermost Pt monolayer.

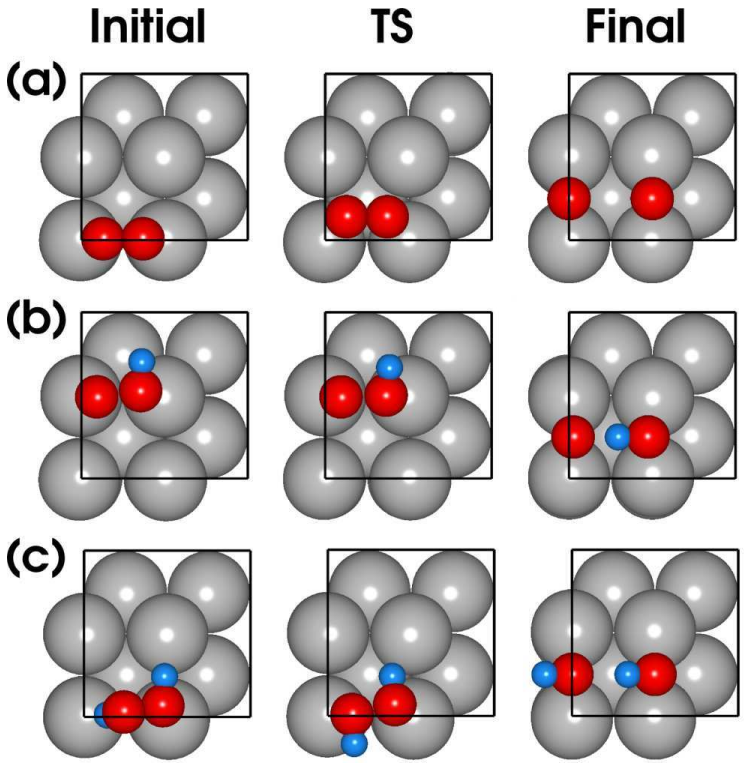

Figure 7.3: Atomic structures of the initial state (left panel), transition state (middle panel), and final state (right panel) for dissociation reactions.

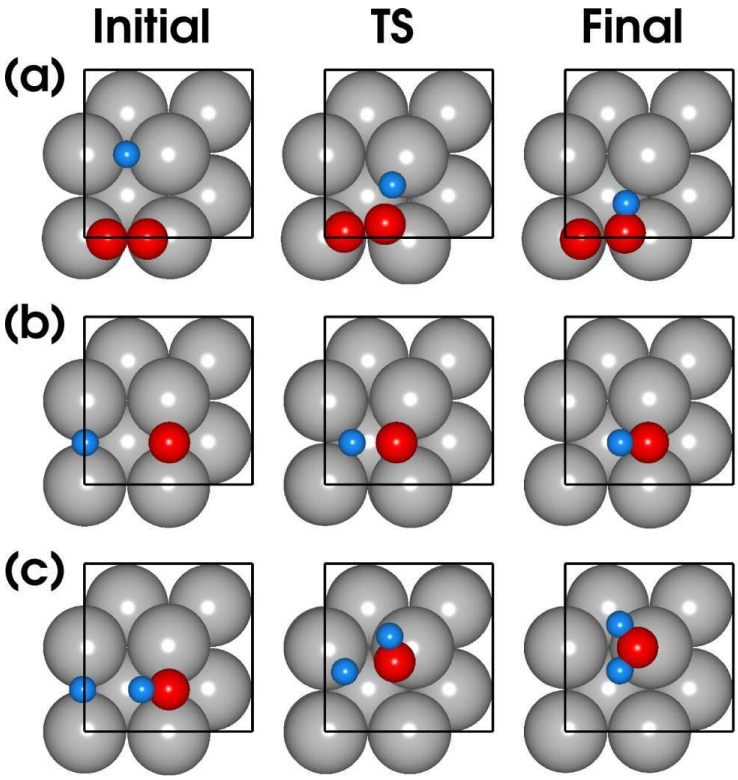

Figure 7.4: Atomic structures of the initial state (left panel), transition state (middle panel), and final state (right panel) for hydrogenation reactions

Table 7.2: Calculated Heats of Reaction (ΔH_0) and Activation Energies (E_a) (in Units of eV) for Various Elementary Steps of ORR on Pt(100) and Pt/Ni(100) Surfaces.

	Pt		Pt/Ni	
reactions	ΔH_0	E_{a}	ΔH_0	E_{a}
O–O bond scission				
$O_2^* \longrightarrow O^* + O^*$	-1.20	0.15	-1.01	0.11
$OOH^* \longrightarrow O^* + OH^*$	-2.15	0.00	-1.95	0.04
$H_2O_2^* \longrightarrow OH^* + OH^*$	-2.74	0.11	-2.56	0.24
hydrogenation				
$O_2^* + H^+ + e^- \longrightarrow OOH^*$	0.26	0.48	0.19	0.49
$OOH^* + H^+ + e^- \longrightarrow H_2O_2^*$	OOH dissociaiton before H_2O_2 formation			
$O^* + H^+ + e^- \longrightarrow OH^*$	-0.43	0.36	-0.53	0.34
$OH^* + H^+ + e^- \longrightarrow H_2O^*$	0.06	0.80	-0.10	0.79

7.4.3 Reaction Energies of ORR on Pt(100) and Pt/Ni(100) Surfaces

As illustrated in Figures 7.3 and 7.4, we constructed the initial and final states of various elementary steps of the ORR on the (100) surfaces based on the adsorption energies and configurations (given in Table 7.1 and Figure 7.2) and subsequently determined the corresponding transition states using the CI-NEB method. Moreover, we reported the calculated reaction energies (heat of reaction and activation energy) for these elementary steps in Table 7.2.

There were three possible routes for reactant O_2 molecule to break the O-O bond during the ORR on the Pt and Pt/Ni(100) surface. (i) O_2 dissociation reaction (Figure 7.3(a)): for this reaction, we assumed the initial state as an O_2 molecule adsorbed at a bridge site and the final state as two O atoms adsorbed at two separate bridge sites. The transition state of the O_2 dissociation reaction was found to be that the O_2 molecule displaced slightly away from its initial adsorption site. (ii) OOH dissociation reaction (Figure 7.3(b)): the initial state is an OOH molecule adsorbed at a bridge site while the final state is the separated O and OH adsorbed at two bridge sites. In the transition state, the OOH molecule displaced slightly away from its initial adsorption site. (iii) H_2O_2 dissociation reaction (Figure 7.3(c)): the initial state is an H_2O_2 molecule adsorbed at a bridge site, and the final state is two OH molecules adsorbed at two bridge sites and with the same orientation. In the transition state, the adsorbed H_2O_2 adopted a planar molecular structure and stayed parallel to the surface.

In Figure 7.4, we plotted the progression of the three hydrogenation reactions of the ORR on the Pt and Pt/Ni(100) surface. (i) O_2 hydrogenation reaction (Figure 7.4(a)): the initial state is the coadsorption of an O_2 molecule at a bridge site and an atomic H at a bridge site. The final state is the formed OOH molecule absorbed at a bridge site. In the transition state, the O_2 molecule extends one O to interact with the migrating H atom. It can be seen in Table 7.1 that this O_2 hydrogenation reaction is endothermic. (ii) O hydrogenation reaction (Figure 7.4(b)): the initial state is the coadsorption of an atomic O at a bridge site and an atomic H at another bridge site across a hollow site while the final state is the adsorption of the formed OH molecule at a bridge site. In the transition state, the atomic H moves toward

the atomic O forming an O-H bond of 1.557 Å. (iii) OH hydrogenation reaction (Figure 7.4(c)): the initial state is the coadsorption of OH and H at two bridge sites, and the final state is the adsorption of H_2O molecule at a nearby top site. In the transition state, the OH molecule rotates by about 90 degree on the surface and moves to a nearby top site while the H atom moves toward the OH. In this study, we found no route for the OOH hydrogenation reaction in which OOH associates with H to form H_2O_2. Our DFT calculations indicated that the OOH molecule always favors dissociating into OH and O before the formation of H_2O_2 on the (100) surfaces.

7.4.4 Reaction Mechanism of ORR on Pt(100) and Pt/Ni(100) Surfaces

The ORR on the Pt(100) and Pt/Ni(100) starts from the adsorption of O_2 on the surfaces in all the three possible mechanisms (as specified in Figure 1.3). Immediately following the O_2 adsorption, the O_2 molecule will either dissociate into two O atoms within the oxygen dissociation mechanism or associate with H to form OOH in both the peroxyl dissociation and the hydrogen peroxide dissociation mechanisms. We predicted in this work that the activation energy of the O_2 dissociation reaction was 0.15 eV on the Pt(100) and 0.11 eV on the Pt/Ni(100) surface. In contrast, we predicted the activation energy of the O_2 hydrogenation reaction to be 0.48 eV on the Pt(100) and 0.49 eV on the Pt/Ni(100) surface. Consequently, the O_2 dissociation reaction has much lower activation energy than the O_2 hydrogenation reaction on the two (100) surfaces. Hence, it is inferred from our DFT calculations that the oxygen dissociation mechanism should be the most feasible pathway for the ORR on the (100) surfaces. Furthermore, our results in Table 7.2 revealed that the rate-determining step for the ORR on the (100) surfaces is the OH hydrogenation reaction (which has activation energy of 0.80 eV on the Pt(100) and 0.79 eV on the Pt/Ni(100) surface) following the oxygen dissociation mechanism.

Examining the influence of electrode potential (U) on the ORR, we employed the method proposed by Nørskov et al.[26] and computed the free-energy diagram of the ORR on the Pt(100) and Pt/Ni(100) surfaces. In Figure 7.5, we plotted these free-energy diagrams assuming the oxygen dissociation ORR mechanism at various electrode potentials. It can be

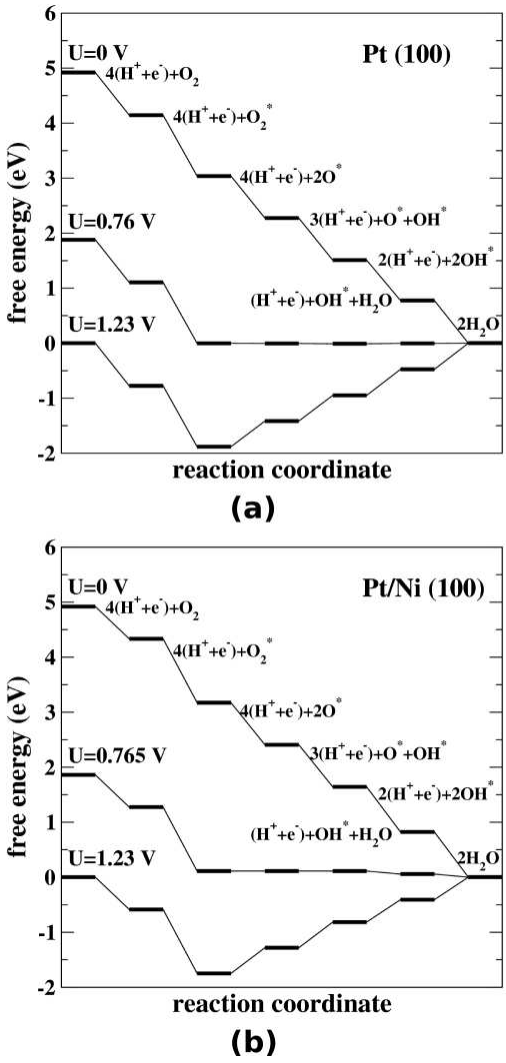

Figure 7.5: Free-energy diagrams for ORR at different electrode potential U on (a) Pt(100) surface and (b) Pt/Ni(100) surface through oxygen dissociation mechanism.

seen in Figure 7.5 that all the elementary steps of the ORR on the (100) surfaces are exothermic (negative free energy changes) when $U = 0$ V. With increasing electrode potential, the free energy change of the hydrogenation reactions become less negative. At the open-circuit voltage $U = 1.23$ V, both the O and OH hydrogenation reactions turn out to be endothermic on the (100) surfaces. Consequently, there is a highest electrode potential under which all the elementary reactions are still exothermic for the oxygen dissociation ORR mechanism

on the (100) surfaces. This critical potential actually defines the working potential of the electrocatalysts. Above the working potential, some elementary reactions of ORR would have positive reaction free energy change and thus require high activation energy on the catalyst surfaces. Our results in Figure 6 predict that the highest working electrode potential is 0.76 V for the Pt(100) surface (Figure 7.5(a)) and 0.765 V for the Pt/Ni(100) surface (Figure 7.5(b)) with the ORR progression via the oxygen dissociation mechanism. Thus, the external electrode potential would not alter the ORR mechanism on the (100) surfaces as long as its value is below 0.76 V.

In consistent with our thermodynamic analysis, the DFT study on the activation energies for the ORR also found that with increasing electrode potential the hydrogenation reactions became more difficult whereas the dissociation reactions were unaffected.[32,151] Consequently, with an increase of applied electrode potential, the peroxyl dissociation and hydrogen peroxide dissociation mechanisms of the ORR (which requires facile hydrogenation reactions before O–O dissociation) become less preferable compared to the direct oxygen dissociation ORR mechanism. Hence, our prediction that the direct oxygen dissociation mechanism is the preferable pathway for the ORR on the (100) surfaces would not be altered even under high electrode potentials.

7.5 DISCUSSION

7.5.1 Ligand Effect

In Figure 7.6, we summarize comparatively our DFT calculation results about the surface adsorption energy, heat of reaction, and activation energy of the ORR on the Pt(100), Pt(111), Pt/Ni(100), and Pt/Ni(111) surfaces. Specifically, we plotted the relative differences in these reaction energies on the Pt/Ni(100) and (111) surfaces with respect to the corresponding values on the Pt(100) and (111) surfaces. In this way, we can illustrate how the subsurface Ni atoms (i.e., ligand effect) would affect the reaction energetics of the ORR on the

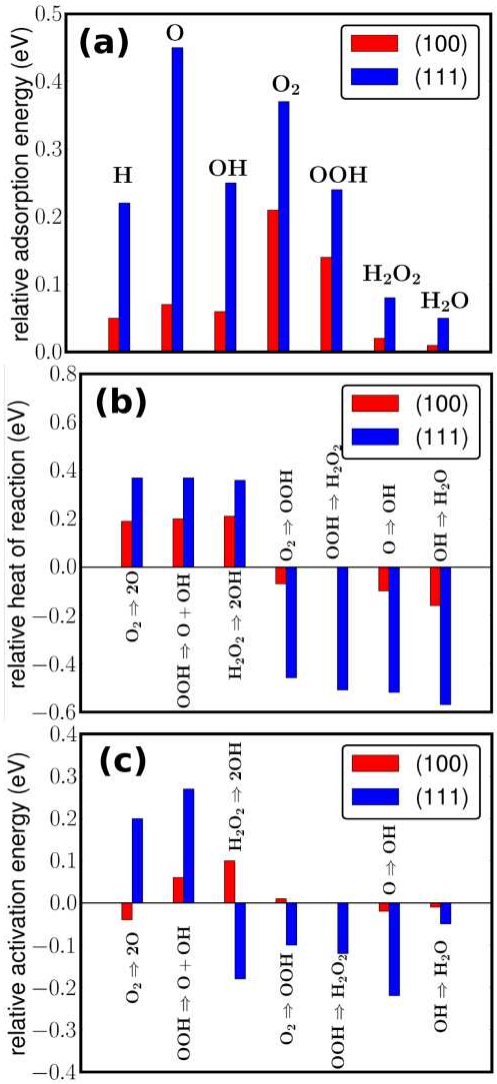

Figure 7.6: Relative energetic quantities related to ORR on the (100) and the (111) surfaces.

Pt/Ni surfaces as compared to on the pure Pt surfaces. It was shown in Figure 7.6(a) that the relative adsorption energies were positive for the ORR intermediates on both the (100) and (111) surfaces. This result revealed that the subsurface Ni atoms would cause chemical species to bind more weakly on the outermost Pt monolayer of the Pt/Ni(100) and (111) surfaces than the respective pure Pt surfaces. As a direct result of this effect, the heats of reaction for the three elementary O–O bond dissociation reactions increase on the Pt/Ni

surfaces with respect to those on the Pt surfaces, and the heats of reaction for the four elementary hydrogenation reactions decreases on the Pt/Ni surfaces with respect to those on the Pt surfaces (as shown in Figure 7.6(b)).

Most often, the activation energy of a chemical reaction is linearly related to its heat of reaction.[132,133] Thus, an increase (or decrease) in heat of reaction is normally associated with an increase (or decrease) in activation energy of the reaction. However, our results in Figure 7.6(c) show that the relative changes of the activation energies for the ORR elementary steps on the Pt/Ni surfaces and Pt surfaces are not always well correlated with the relative change of the heats of reaction on these surfaces. For example, we found that the activation energy would decrease for the H_2O_2 dissociation reaction on the Pt/Ni(111) relative to that on the Pt(111) surface and for the O_2 dissociation reaction on the Pt/Ni(100) relative to that on the Pt(100) surface, although the heat of reaction for the same reactions increased. In addition, the O_2 hydrogenation reaction was found to have higher activation energy but lower heat of reaction on the Pt/Ni(100) surface than on the Pt(100) surface.

In summary, our study indicated that the subsurface Ni atoms in the Pt/Ni surfaces would modify the electronic structure of the outermost Pt layer, weaken the binding of the chemical species to the surface, and hence change the reaction energies of the ORR on the catalysts. It should be mentioned that we used a simplified surface model which has a complete Ni subsurface layer in this theoretical study. In real Pt-Ni alloy catalysts, the Ni concentration in the subsurface could be much less (for example, about 50 atom % in the annealed Pt_3Ni (111) sample[12]). Therefore, the actual ligand effect in the annealed Pt-Ni catalysts could be conceivably smaller than our predictions.

7.5.2 Structural Effect

Shown in Figure 7.1, the (111) and (100) surfaces of a face-centered cubic crystal have different structural arrangement of atoms. Hence, the densities of surface atoms of the two surfaces are not equal. In this work, we assumed that all the elementary steps of the ORR could be accomplished within a 2×2 (111) or (100) surface unit cell, corresponding to 0.25 ML coverage of O during the ORR. With this assumption, the density of active sites on the

(100) surface would be about 13.4% lower than that on the (111) surface. Consequently, the structural effect accounts for at least 13.4% activity reduction for the ORR on the (100) surface as compared to that on the (111) surface with the same surface area. Moreover, we found in this study that the ORR could proceed following different reaction mechanisms on the different surfaces of catalysts. Our theoretical study suggests that the ORR would favorably proceed with the peroxyl dissociation mechanism on the Pt(111) surface whereas with the oxygen dissociation mechanism on the Pt(100) surface.

Furthermore, the structural effect of the catalyst surfaces influences the extent of the ligand effect induced by the subsurface Ni atoms on the ORR on the Pt/Ni surfaces. Clearly shown in Figure 7.1(a) and (b), the subsurface Ni atoms cause larger changes in the adsorption energy and heat of reaction of the ORR on the Pt/Ni(111) than the Pt/Ni(100) surface. Due to large changes in reaction energetics, our results in ref[2] revealed that the subsurface Ni atoms could even lead to a change of the mechanism for the ORR on the Pt/Ni(111) surface (where the ORR was predicted to assume the hydrogen peroxide dissociation mechanism) as compared to on the pure Pt(111) surface (where the ORR was predicted to assume the peroxyl dissociation mechanism). In contrast, our DFT results imply that the ORR would share the same mechanism (the oxygen dissociation mechanism) on both the Pt/Ni(100) and Pt(100) surfaces.

7.5.3 Comparison of ORR on Pt(100), Pt(111), Pt/Ni(100), and Pt/Ni(111) Surfaces

In Figure 7.7, we summarize comparatively our DFT calculation results about the favorite pathway of the ORR on the Pt(100), Pt(111), Pt/Ni(100), and Pt/Ni(111) surfaces. In particular, we identify the rate-determining step for the ORR to be the OH hydrogenation reaction with activation energy of 0.80 eV on the Pt(100) surface, the O hydrogenation reaction with activation energy of 0.79 eV on the Pt(111) surface, the OH hydrogenation reaction with activation energy of 0.79 eV on the Pt/Ni(100) surface, and the O_2 hydrogenation reaction with activation energy of 0.15 eV on the Pt/Ni(111) surface. It should be pointed out that in this study we assumed the Langmuir-Hinshelwood type of hydrogenation

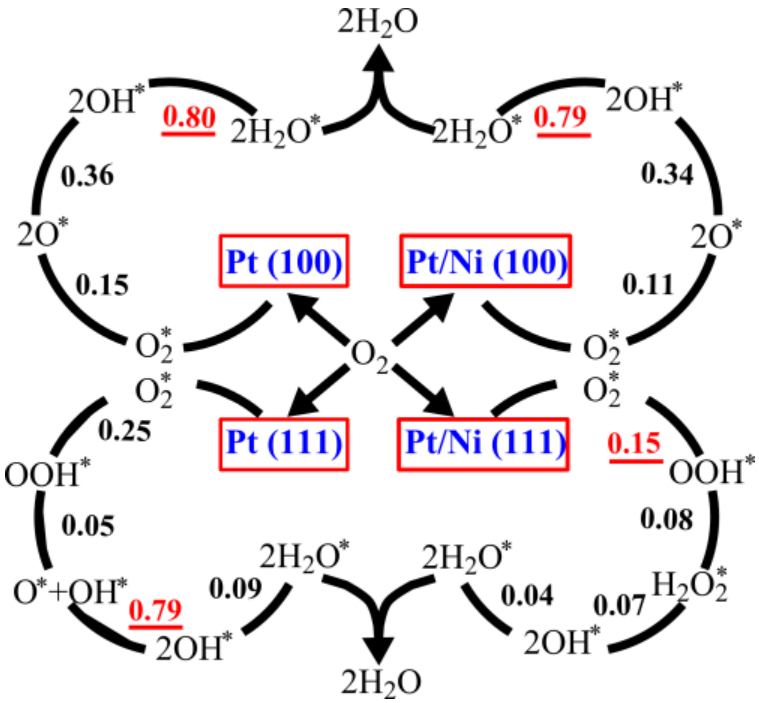

Figure 7.7: Relative energetic quantities related to ORR on the (100) and the (111) surfaces.

reactions in which protons were already transferred from electrolytes to the catalyst surface and associated with an electron. Employing the procedure given in ref 30, we estimated the energy barrier for this proton transfer reaction $H^+ + e^- \longrightarrow H^*$ at 0.8 V to be 0.20 eV on the Pt(100) surface, 0.33 eV on the Pt(111) surface, 0.25 eV on the Pt/Ni(100) surface, and 0.55 eV on the Pt/Ni(111) surface. Hence, if considering the reaction of proton transfer from electrolytes to the catalysts as an elementary step of the ORR, we found that the rate-determining step for ORR on the Pt/Ni(111) surface could just be the proton transfer reaction with activation energy of 0.55 eV.

As discussed in section 7.5.2 , the density of active sites is reduced on the (100) surfaces as compared to the (111) surface. Considering both the activation energy of the ratedetermining step and the density of the active sites, we infer from our DFT calculations that the ORR would proceed more slowly on the Pt(100) than the Pt(111) surface, and importantly, the Pt/Ni (111) surface would have much higher activity for the ORR than all the other three

surfaces. Remarkably, our theoretical predictions in this study are in good agreement with previous experimental results which reported that the Pt(111) surface sample had about two times higher activity for ORR than the Pt(100) surface sample whereas the $Pt_3Ni(111)$ single-crystal surface sample exhibited an activity enhancement for ORR by about 10 times as compared to the $Pt_3Ni(100)$ surface sample.[12]

7.6 CONCLUSIONS

In this work, we calculated the reaction energetics (surface adsorption energy, heat of reaction, and activation energy) related to all the possible elementary steps of the ORR on the Pt(100) and Pt/Ni(100) surfaces using the first-principles DFT method. Our calculation results suggested that the ORR would most possibly proceed following the oxygen dissociation mechanism, in which the O–O bond in the O_2 molecule is split immediately after the O_2 surface adsorption, on both the Pt(100) and Pt/Ni(100) surfaces. Moreover, we predicted that the rate-determining step for the ORR on the two (100) surfaces would be the OH hydrogenation reaction which required activation energy of 0.80 eV on the Pt(100) surface and 0.79 eV on the Pt/Ni(100) surface. Examining both the ligand and structural effects, we compared our calculated reaction energetics of the ORR on the Pt(100), Pt(111), Pt/Ni(100), and Pt/Ni(111) surfaces. It was found that the subsurface Ni atoms would weaken the strength of various ORR chemical intermediates binding to the outermost Pt monolayers on both the Pt(111) and (100) surfaces and hence cause an increase in the heats of reaction of all the O–O bond dissociation reactions and a decrease in the heats of reaction of all the hydrogenation reactions of the ORR on the Pt/Ni surfaces with respect to those on the pure Pt surfaces.

Furthermore, we noticed that the difference in structures led to that the ligand effect induced by the subsurface Ni atoms was more pronounced in the ORR on the (111) surfaces than the (100) surfaces. On the (111) surfaces, we predicted that the strong ligand effect changed the ORR mechanism from the proxyl dissociation mechanism on the Pt(111) surface to the hydrogen peroxide dissociation mechanism on the Pt/Ni(111) surface. In contrast,

the relatively weak ligand effect was found not to change the ORR mechanism on the (100) surfaces. In this work, we determined the activation energies for the ratedetermining step of the ORR on the Pt(100) to be 0.80 eV, on the Pt/Ni(100) to be 0.79 eV, on the Pt(111) to be 0.79 eV, and on the Pt/Ni(111) to be 0.15 eV. Thus, it can be inferred that the catalytic activity for the ORR would be slightly higher on the Pt/Ni(100) than on the Pt(100) surface, would be reasonably higher on the Pt(111) than on the Pt(100) surface, and would be much higher on the Pt/Ni(111) than the Pt(111) surface. These predictions agree well with experimental measurements.

In summary, our study yields new molecular-level understanding related to the progression of the ORR on the Pt(100) and Pt/Ni(100) catalyst surfaces. Importantly, we provide an explanation, in terms of ligand and structural effects, to the experimentally observed trend of the activity for the ORR on the single-crystal Pt(100), Pt(111), Pt/Ni(100), and Pt/Ni(111) electrocatalysts. The theoretical insights gained in this study are useful for designing high-performance metal catalysts in PEM fuel cells.

8.0 KINETIC MONTE CARLO SIMULATION OF OXYGEN REDUCTION REACTION ON PLATINUM (111) AND PLATINUM (100) SURFACES

8.1 ABSTRACT

In this work, kinetic Monte Carlo algorithm is implemented to study the kinetics of ORR based on the mechanistic information obtained in the second study. The information of the elementary reactions involved in ORR such as the adsorption sites of the reactants and products, activation energies, etc. is input into the KMC code. The KMC simulation can simulate the dynamics of ORR and output the current density (joules/cm^2/s) generated from the reactions. Then, the simulated current density which is a measure of ORR activity can be directly compared to experimental measurement. In the study, kinetics of ORR on Pt (111) and Pt (100) surfaces were simulated. The simulated current density of ORR on Pt (111) and Pt (100) at electrode potential 0.8 V is in the same magnitude with experimental measurement, although the actual value is about 2 times lower. The reasonable agreement with experiments also in turn indicates that the previous mechanistic study is reliable.

8.2 INTRODUCTION

In the previous studies, we have performed mechanistic studies of ORR on Pt (111) and Pt (100) surfaces with first-principles DFT simulations. During these studies, we have obtained the activation energies and various elementary steps and identified possible reaction mechanism and rate-determining steps. However, the link between these molecular details of ORR and the kinetics of ORR, which contains the information about the dependence of reaction

rate on reaction conditions, is still missing. Although kinetics plays such an important role in catalysis, its theory has for a long time mainly been restricted to macroscopic rate equations. These implicitly assume a random distribution of adsorbates on the catalysts' surface. Effects of lateral interactions, reactant segregation, site blocking, and defects have only been described ad hoc. With kinetic Monte Carlo (KMC) simulation, it has become possible to follow reaction systems on an atomic scale, and thus to study these effects. In this work, we have developed a KMC code and input the mechanistic information of ORR into the code. By doing this, we are capable of investigating the kinetics of ORR on Pt (111) and Pt (100) surfaces. We output the macroscopic information such as current as a function of time.

8.3 SIMULATION METHODS

The kinetic Monte Carlo (KMC) algorithm is written in the FORTRAN object-oriented language and contains a series of objects useful for describing molecular kinetics and atomic surface structure. Individual adsorbates, surface reactions, and the atomic surface structure comprise a set of fundamental objects around which the code is constructed. We first describe the fundamental objects in the simulation and then discuss the supplementary objects that are used to connect these fundamental objects.

The most basic fundamental object in the simulation is the species object. The species object defines the reactants, products, and intermediates by their physical properties. This includes their adsorption properties (binding energy at different surface sites) as well as their physical characteristics (atomization energy). This information provides the detailed makeup for each species. Surface species are then used to build a set of surface reaction objects. A surface reaction is defined by the type of reaction along with the specification of the reactants and products. Each reaction is assigned forward and reverse activation energies along with corresponding preexponential factors that are valid for the zero coverage limit. Coverage effects are explicitly accounted for in the lateral interaction model described later.

Both the surface species and the individual reactions are fundamental objects that depend on the simulation surface or grid object. A grid object contains information about the

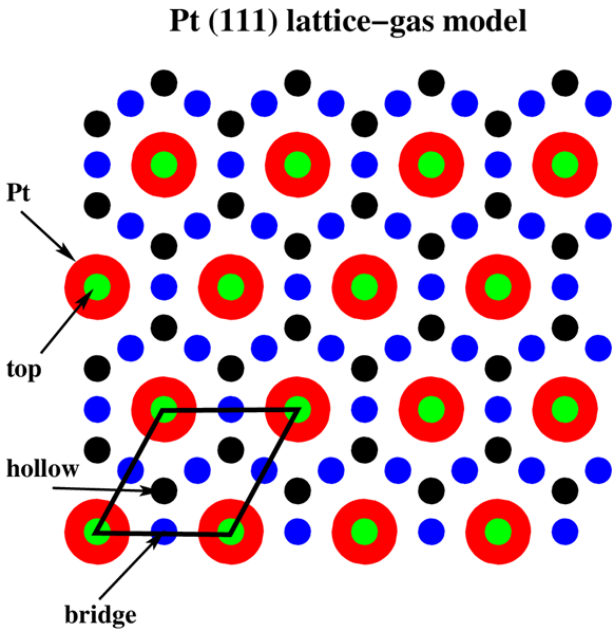

Figure 8.1: Mapping of Pt (111) surface into lattice grid points.

type of the surface site, its location in space, connectivity to neighboring surface sites, and occupation status. An array of grid objects are used to represent Pt (111) and Pt (100) surfaces. The actual mapping of Pt (111) surface is shown in Fig. 8.1 Periodic boundary conditions are used to model an actual surface. When the metal and the adsorbate layers are initialized, all atop, bridge, and hollow grid sites are defined by their location in space with respect to the (111) surface. The adsorbate and metal layers are connected with pointers so that surface sites can address the location of metal atoms to which they are bound. In addition, the surface layer sites identify and store information about neighboring surface sites which are within close proximity. The cutoff distance for the surrounding environment is two times the metal-metal distance.

The interaction model object is used to determine the lateral interaction energy between different species as a function of distance on the grid. In this work, we use a modified bond order conservation (BOC) method for calculating through-surface interactions[153,154] and a sum of hard atomic spheres method for calculating pairwise through-space interactions.

Through-surface interactions are based on well-known BOC principles.[154,155] The BOC predicted interactions were rescaled by 20 % to match first-principle DFT quantum chemical results. An earlier comparison of the strict BOC predictions with DFT results suggested that these interactions are overpredicted.[154] If two neighboring adsorbates can occupy their respective sites without resulting in a negative binding energy for either site, adsorption is allowed.

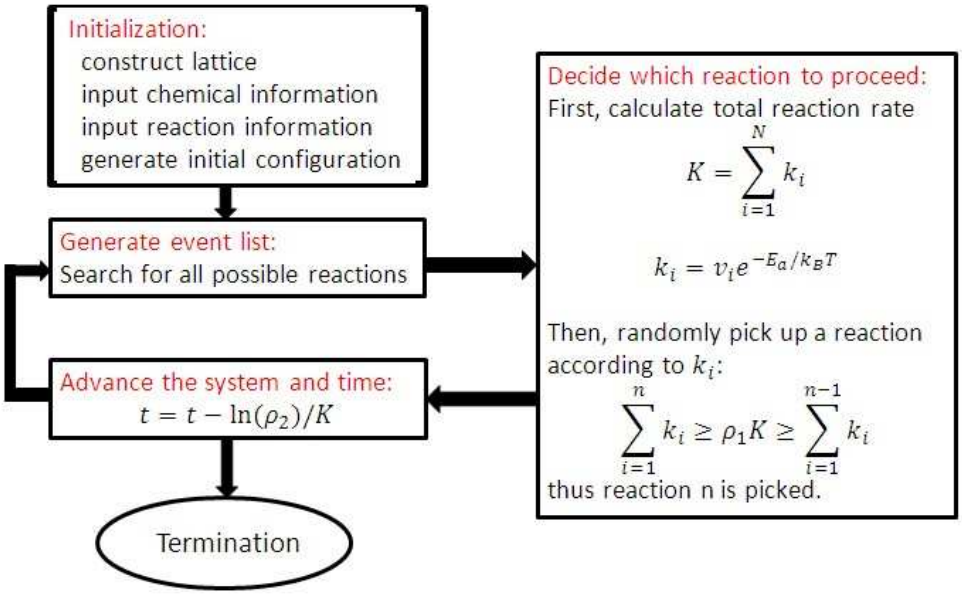

Figure 8.2: Flowchart of KMC algorithm.

The surface reaction environment is an object that includes both the reaction ensemble and its outcome. The object is used to build all possible reaction ensembles based on the local environment of the reactants. Generally, the input includes two grid sites, the surface reaction, and the interaction model. The builder then decides whether the reaction is possible based upon the occupancy of the grid sites involved. If the reaction is possible, more detailed calculations are performed. The builder also determines what the favorable product sites are. These product sites will favor positions near the original pair of grid sites that were chosen, but may not be equivalent to them. The occupancy, the binding energy, and the

local environment of these product sites affect the reaction probabilities. This results in a multisite Monte Carlo approach. So, although two sites are chosen, many sites are actually involved in the developing the reaction environment.

The simulation object is at the heart of the approach. It inventories all possible events along with their explicit local reaction environment, calculates their rates, determines which reactions occur, equilibrates the surface structure, analyzes the simulation results, and generates the output. An outline of the algorithm is shown in Fig. 8.2.

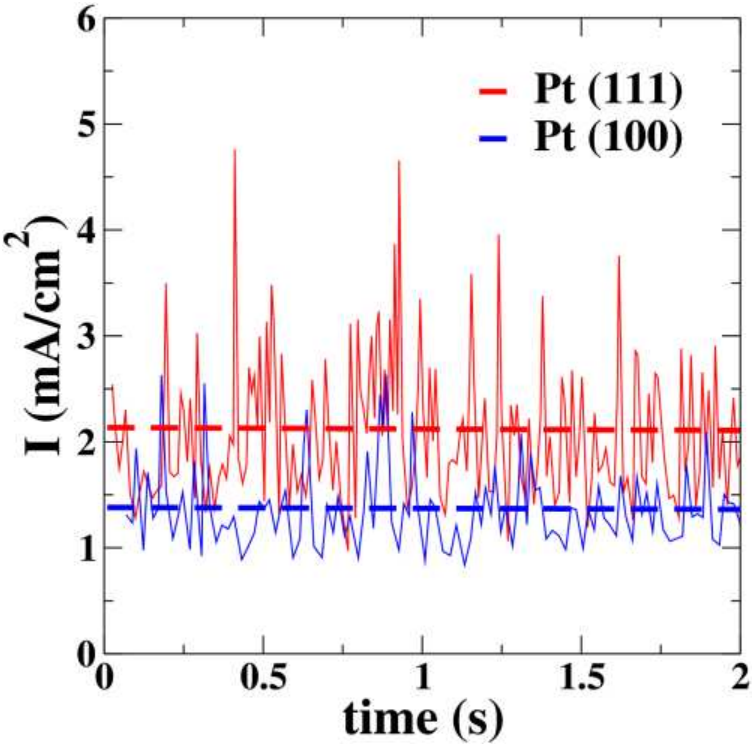

Figure 8.3: Current generated from oxygen reduction reaction as a funciton of time.

8.4 RESULTS

Previously, we calculated the binding energies for various chemical intermediates and activation energies for various elementary reactions involved in ORR on Pt (111) and Pt (100) surfaces. In this study, we use these data as input to KMC code. The vibrational frequency

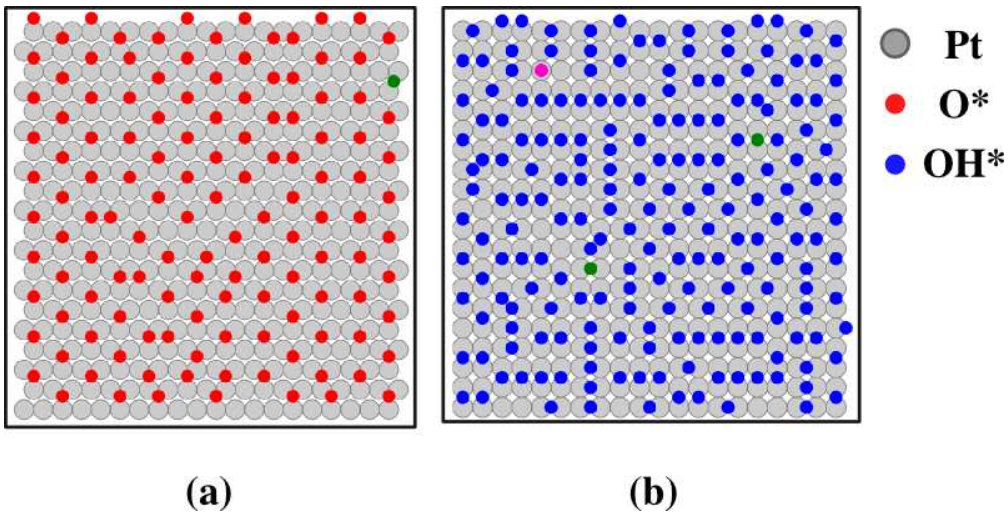

Figure 8.4: The surface configuration after the generated current reaches equilibirum on (a) Pt (111) (b) Pt (100) surface. Grey dots represent Pt atoms. Red dots represent O atom. Blue dots represent OH molecule.

for each reaction is fixed to $1 \times 10^1 3/\text{s}$ which is typical for chemical reactions. We also include the reaction of the adsorption of hydrogen ions to the surface. The activation energy for this reaction is a function of electrode potential U. We simulated the ORR on Pt (111) and Pt (100) surface at $U = 0.8$ V. We output the current generated from those electrochemical reactions as a function of time in Fig. 8.3. The currents are in average 2.13 and 1.38 mA/cm^2 on Pt (111) and Pt (100). The results are in the same magnitude to experimental measurements that the current is about 5.5 mA/cm^2 on Pt (111) at 0.8 V surface.[12] The reactivity of Pt (100) is about two times lower than Pt (111) surface, which is in good agreement to experimental findings.[12] It is also observed that ORR proceeds through OOH dissociation mechanism on Pt (111) surface and O_2 dissociation mechanism on Pt (100) surface. This observation is in consistent with our prediction from calculated activation energies in previous chapters. The surface of Pt (111) is mostly covered with oxygen atoms as shown in Fig. 8.4 (a). This is a result of difficulty in removing oxygen from the surface, in other works, atomic oxygen reduction is the rate-determining step. On Pt (100) surface, the rate-determining step is OH hydrogenation, so the surface covered mostly by OH.

9.0 OXYGEN CHEMISORPTION-INDUCED SURFACE SEGREGATION IN PLATINUM-NICKEL (111) SURFACES

9.1 ABSTRACT

In this study, we studied the oxygen chemisorption-induced surface segregation in Pt-Ni (111) surface with grand canonical Monte Carlo simulations and developed Pt-Ni-O modified embedded-atom method interatomic potential. We found, in oxygen atmosphere, the adsorbed oxygen atoms would make Ni atoms in Pt-Ni atoms segregate to the outermost surface due to the stronger binding energy between Ni and O atoms as compared to Pt-O binding. Our simulation results confirmed the experimental findings and provided molecular-level details of the surface composition and structure of segregated Pt-Ni (111) surface.We also demonstrated that by varying the Pt-Ni composition and oxygen partial pressure, the surface composition and structure of the segregated Pt-Ni (111) surface could be manipulated. Hence, bimetallic surfaces with different catalytic characteristic and reactivity could be achieved.

9.2 INTRODUCTION

Previous studies have shown that Pt-based alloys lead to increased catalytic activity for the oxygen reduction reaction (ORR) in the cathode of proton-exchange membrane fuel cells (PEMFCs) as compared to pure Pt catalysts. For example, Pt_3M (M=Ni, Co, Fe, Ti, V) have shown to more active for catalyzing ORR.[12,13] This increase in activity is attributed to the unique surface composition formed through surface segregation process when the Pt-based

alloys are annealed in vacuum. The annealed sample leads to a oscillatory composition profile in which the surface forms a "Pt-skin" outermost layer and the second layer is enriched with the 3d transition metal. The electronic structure of the "Pt-skin" is therefore modified by the subsurface transition metal to have a weaker oxygen binding energy , so catalysts' surfaces are less poisoned by the strong oxygen adsorption. However, in the oxidizing environment in the cathode of PEMFCs, this desired surface configuration may not be stable and may be deactivated eventually by the surface segregation of 3d transition metals provided that 3d/Pt (111) surfaces have been predicted to bind oxygen much more strongly than pure Pt (111) and Pt/3d (111).[23,156] Experimetally, it has been demonstrated that 3d transition metals would segregated to the outermost layer in oxygen environment.[156,157]

Due to the importance of surface composition and structure in catalytic activity, it is of utmost importance and interest to control the reactivity of bimetallic surfaces by controlling their surface composition and structures. Recently, it has been demonstrated in a Pt-Cu system that such control could be achieved by modifying the atomic structure of the surface through annealing the sample in different atmospheric environment.[158] Through the method, different surface structures such as overlayer, near surface alloy, and surface alloy were prepared and shown to have markedly different characteristics.

In this study, we employed grand canonical Monte Carlo simulations (GCMC) and MEAM interatomic interaction model to study the surface segregation phenomenon in Pt-Ni (111) surface in oxygen atmosphere. We also studied the surface structure of Pt-Ni (111) as a function of the composition of Pt-Ni alloy and the partial pressure of oxygen gas.

9.3 COMPUTATIONAL METHODS

9.3.0.1 Grand-canonical Monte Carlo Simulation In order to simulate adsorption/desorption process on alloy surfaces, we performed GCMC, in which temperature (T), volume of the simulation box (V), and the chemical potential (μ) of the atoms (atomic oxygen in this work) being added/deleted to/from the system are fixed. In our GCMC simulation, the Metropolis algorithm was employed to sample the configuration space. Our sampling scheme is consists of four types of trial movements:

(1) We displace a randomly selected atom from its original position. In bulk simulations, the direction of the displacement is also randomly selected. In surface simulations, atoms are displaced in the normal direction to the surface. The magnitude of the displacement is chosen to be in the range of (0, $r_{\max}$). At a given temperature, the maximum displacement $r_{\max}$ is updated during the simulation so that the acceptance rate of new configuration is about 0.5 in bulk simulation. In surface simulations, rmax is fixed to 0.02 Åin order to avoid drastic structure change.

(2) We exchange the positions of two randomly selected metal atoms with different element types.

(3) An oxygen atom is inserted at a random selected adsorption site.

(4) A randomly selected adsorbed oxygen atom is removed from the system.

Event (1) and (2) are accepted according to the probability of $\min\left(1, \exp\left(-\Delta E/k_B T\right)\right)$, in which ΔE is the potential energy change associated with the performed trial movement, k_B is the Boltzmann's constant, and T is the simulation temperature. Event (3) and (4) result in change of number of atoms in the system, hence, new configurations are accepted with different probabilities. The insertion of oxygen atom is accepted with probability:

$$P(N \to N+1) = \min\left(1, \frac{V}{\Lambda^3(N+1)} \exp\left(\beta[\mu - \Delta E_{N+1,N}]\right)\right) \tag{9.1}$$

The removal of oxygen atom is accepted with probability:

$$P(N \to N-1) = \min\left(1, \frac{\Lambda^3 N}{V} \exp\left(\beta[\mu + \Delta E_{N-1,N}]\right)\right) \tag{9.2}$$

Here, $\beta = 1/k_BT$ and $\Lambda = \sqrt{h^2/2\pi m k_B T}$ is the thermal de Broglie wavelength (h is Plank's constant and m is the particle mass). In order to have a good acceptance of insertion acceptance rate, the oxygen atoms are inserted to prescribed adsorption sites instead of random position in the simulation box. As a result, the volume V in Equ. 9.1 and 9.2 is not the volume of the simulation box but accessible volume. In our simulations, the accessible volume is approximated as the volume of a thin box layer above the surface with a height of 5 Å.

9.3.0.2 Settings for density functional theory calculations In order to parameterize the MEAM potentials for the Pt-Ni-O system, first-principles density functional theory (DFT) calculations were employed to determine some bulk and surface properties which were served as target values. The DFT calculations in this study were performed using the Vienna Ab initio Simulation Package (VASP) code.[71,72] In all the calculations, we used ultrasoft pseudopotential[121] and a kinetic energy cutoff of 400 eV to expand the electronic wave functions in the plane-wave basis. The generalized gradient approximation with Perdew-Wang 91 functional[42] was used for evaluating exchange-correlation energy. Spin-polarization was included in all the DFT calculations. A $16 \times 16 \times 16$ Monkhorst-Pack[75] k-point mesh was used for Brillouin zone integration in our bulk unit cell calculations, while a $5 \times 5 \times 1$ mesh was used in our surface slab calculations. Fully-optimized surface structures and adsorption configurations were obtained by reducing the Hellman-Feynman force acting on each ion to less than 0.01 eV/Å.

9.4 DEVELOPING PT-NI-O TERNARY MEAM POTENTIALS

The Pt-Ni-O ternary system consists of three binary subsystems, i.e. Pt-Ni, Pt-O, and Ni-O systems. In our previous study on the surface segregation in Pt-Ni nanoparticles, we have presented a well-tested Pt-Ni MEAM potential that could quantitatively predict the surface concentration profile in Pt-Ni extended surface and nanoparticles. In this study, the same Pt-Ni potential was adopted and we focused on developing the MEAM potentials for Pt-O

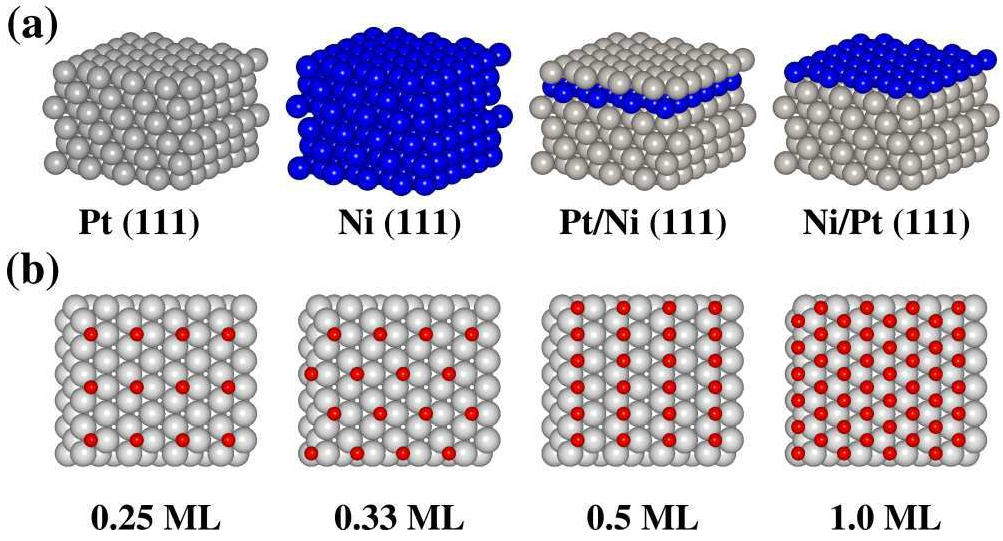

Figure 9.1: (a) Four surface slab models for oxygen adsorption energy calculations. (b) Four oxygen adsorption configurations with different coverages for oxygen adsorption energy calculations.

and Ni-O subsystems. In the formulism of MEAM potential, distribution of net charges and the resulted long-range interaction in the simulated system are not involved, so instead of developing a potential for Pt oxides and Ni oxides, we hereby limit the scope of our Pt-Ni-O MEAM potentials to dealing with surface adsorption of oxygen on the surfaces of Pt, Ni, and Pt-Ni alloy. To this end, the parameters involved in the MEAM potentials were developed by fitting to the DFT-calculated oxygen adsorption energies, which are calculated as

$$\Delta E_O = \frac{1}{N_O}(E_{\text{slab/O}} - E_{\text{slab}} - \frac{N_O}{2}E_{\text{O}_2}) \tag{9.3}$$

where $E_{\text{slab/O}}$ and E_{slab} are energies of surface slab model with or without oxygen adsorbates and N_O and E_{O_2} are the number of oxygen atoms and the energy of oxygen molecule. The oxygen adsorption energies were calculated on four kinds of surfaces slabs, i.e. Pt(111), Ni(111), Pt/Ni(111), and Ni/Pt(111). Pt(111) and Ni(111) are simply pure metal surfaces, while Pt/Ni(111) and Ni/Pt(111) are surfaces with Pt overlayer on Ni(111) slab and Ni overlayer on Pt(111) slab. The atomic structures of the four surface slab models are shown in

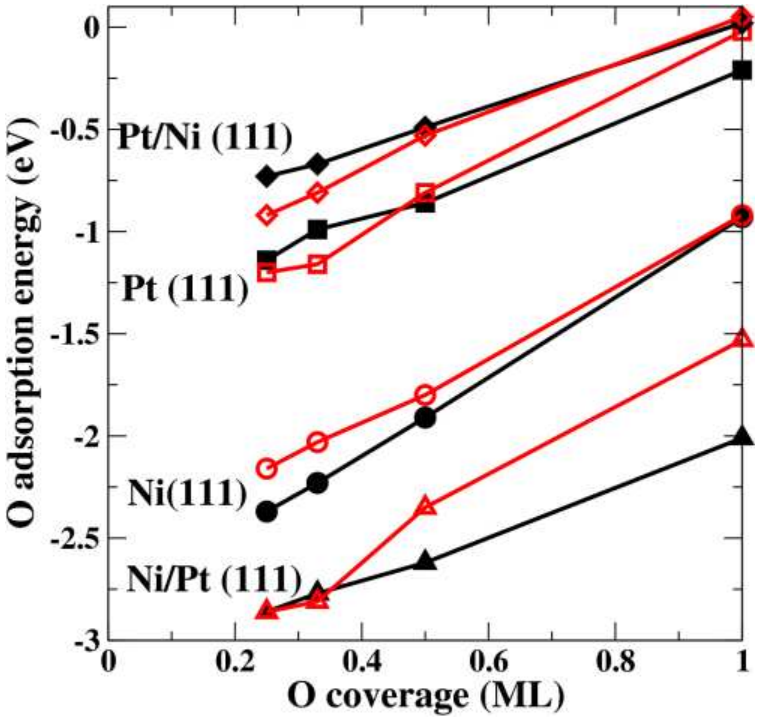

Figure 9.2: Oxgyen adsorption energies on various surface slab models and oxygen adsorption configurations. Black lines with solid markers are oxygen adsorption energies calculated by DFT. Red lines with hollow markers are oxygen adsorption energies calculated by MEAM potential.

Figure 9.1(a). Besides, based on the four different surface slab models, examination of effects of different adsorption sites and oxygen coverage were also involved in our fitting process given that adsorption site preference and the lateral interaction between oxygen adsorbates are essential factors in determining the surface coverage and ordering. The various considered atomic configurations of adsorbed oxygen atoms of different surface coverage are shown in Figure 9.1(b). In the figure, all oxygen atoms are adsorbed on the fcc hollow site. The various oxygen adsorption energies calculated from both DFT and the developed Pt-Ni-O MEAM potential are plotted in Figure 9.2. The oxygen adsorption energies calculated by MEAM potential (hollow markers linked with red lines) are in qualitative agreement with the DFT-calculated values (full markers linked with black lines). Firstly, the developed MEAM

potential can well reproduce the relative binding strength on the four kinds of surfaces, among which Ni/Pt(111) surface binds oxygen the most strongly and is followed by Ni(111), Pt(111), and Pt/Ni(111) surfaces. Secondly, The MEAM potential also captures the repulsive nature of interaction between the adsorbed oxygen atoms: binding energy increases with increasing oxygen coverage. The slopes of the increasing binding energy with respect to the oxygen coverage are well reproduced as compared to DFT values. The adsorption of oxygen atoms on hcp hollow site was also tested. DFT calculations suggest oxygen binds much less stably on hcp site than fcc site, while our MEAM potential cannot differentiate hcp site and fcc site. For example, oxygen adsorption energy on Pt(111) with 1/4 ML coverage is -1.14 eV for fcc site and -0.72 eV on hcp site. On the other hand, MEAM potential predicts -1.20 eV on both fcc and hcp sites. This discrepancy could result in inaccuracy in predicting the ordering of the adsorbed oxygen atoms, which will be manifested in the following paragraph.

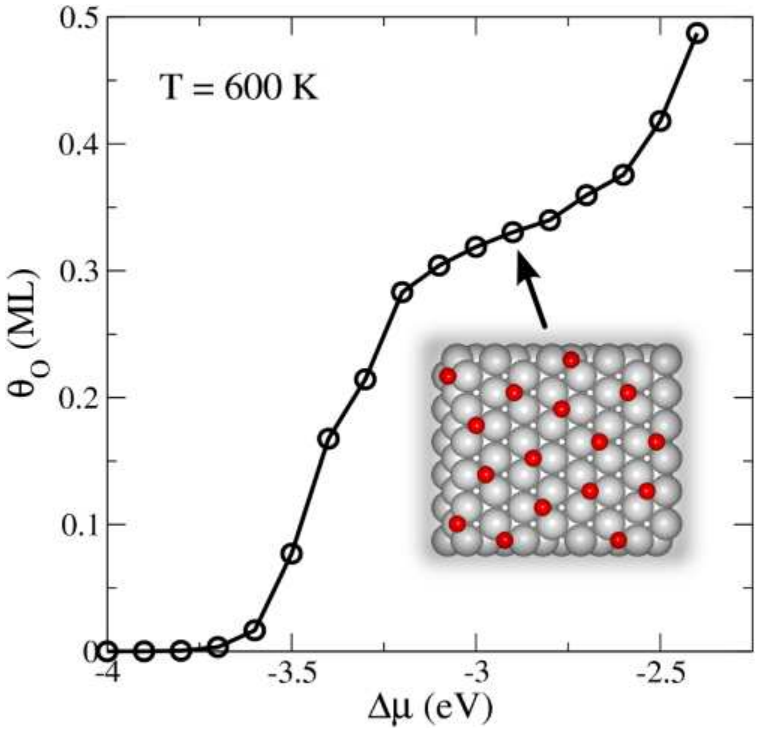

Figure 9.3: Oxygen coverage as a funciton of the chemical potential of oxygen ($\Delta\mu_O$) at $T = 600$ K.

To further validate the developed MEAM potential, we conducted GCMC simulation to investigate the oxygen coverage on Pt (111) surface as a function of oxygen chemical potential ($\Delta\mu_O$) at $T = 600$ K. In the simulation, we employed a Pt surface slab with 15 layers and 48 atoms in each layer. For each $\Delta\mu_O$ tested, 2×10^6 steps were performed to guarantee the convergence of the system energy. In each MC step, we tried to either displace an atom or insert/delete an oxygen atom in/from the prescribed adsorption sties. The resulted curve of oxygen coverage as a function of $\Delta\mu_O$ is plotted in Figure 9.3.

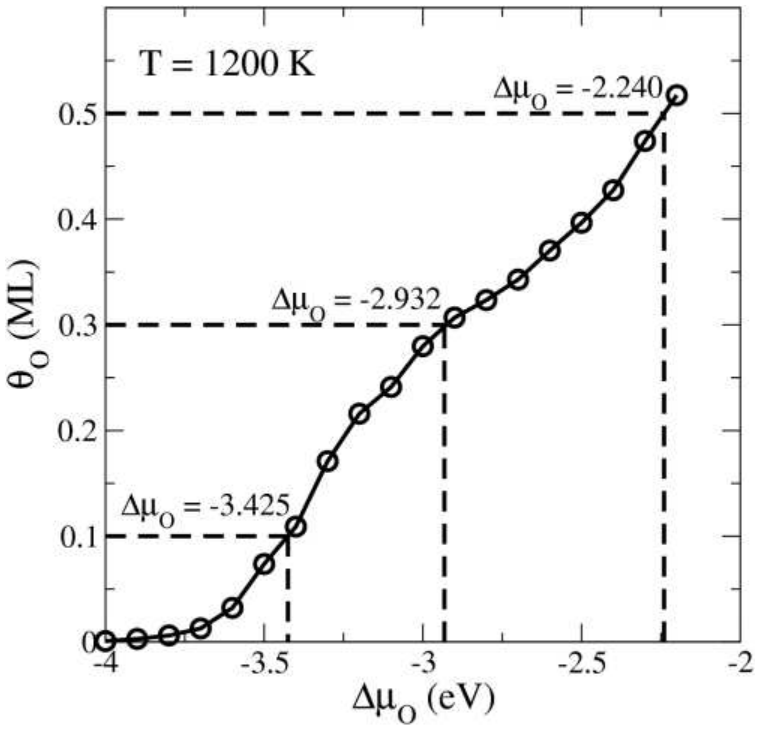

Figure 9.4: Oxygen coverage as a funciton of the chemical potential of oxygen ($\Delta\mu_O$) at $T = 1200$ K.

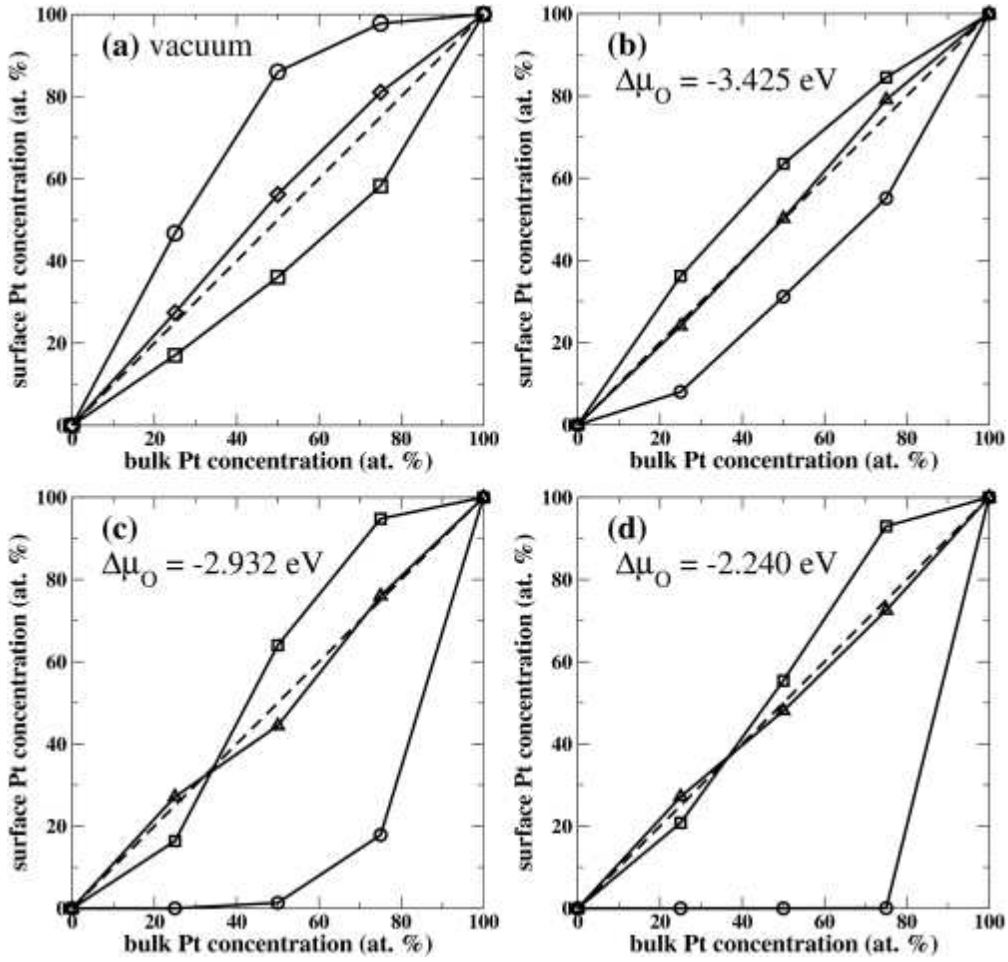

Figure 9.5: Surface composition profile of Pt-Ni (111) surface in (a) vacuum (b) $\Delta\mu_O = -3.425$ eV (c) $\Delta\mu_O = -2.932$ eV (d) $\Delta\mu_O = -2.240$ eV

9.5 RESULTS AND DISCUSSION

In this section, we intend to investigate the equilibrium surface structural factors such as surface composition profile and surface atomic ordering of Pt-Ni (111) surface at high annealing temperature $T = 1200$ K in the oxygen environment. The equilibrium surface structure of Pt-Ni (111) surface is a function of two variables, i.e. the bulk composition of Pt-Ni alloy and the partial pressure of oxygen. So, in order to investigate the surface segregation phenomenon, we carried out GCMC simulations under various oxygen chemical potentials and

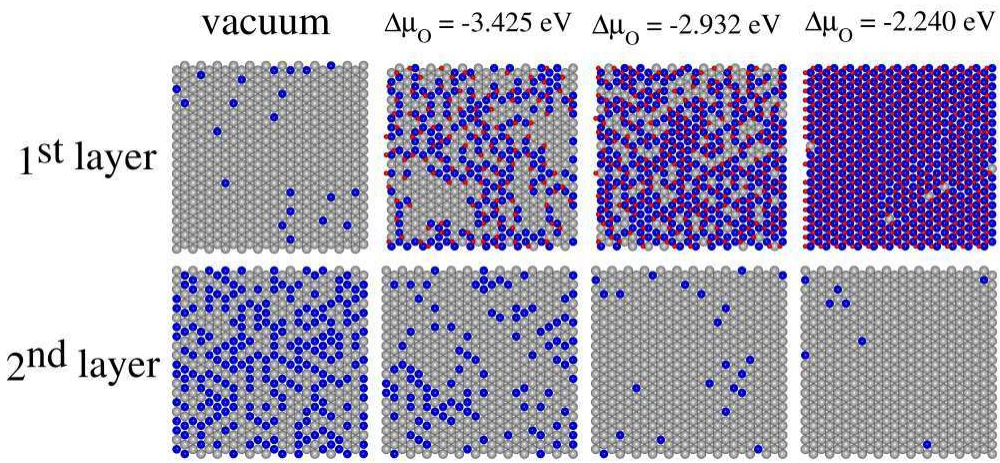

Figure 9.6: The atomic structures of the surface-segregated $Pt_{75}Ni_{25}$ (111) surface and subsurface under various atmospheric environments.

bulk compositions. The oxygen chemical potentials are chosen based on their corresponding coverage on Pt (111) at $T = 1200$ K. In Figure 9.4, the oxygen coverage on Pt (111) at $T = 1200$ K is plot as a function of oxygen chemical potential. As shown in the figure, three values of chemical potentials, which are corresponding to 0.1 ML, 0.3 ML, and 0.5 ML adsorbed oxygen on Pt (111) surface, are selected. Besides, three different Pt-Ni alloy compositions are chosen for studying the dependence of surface composition profile on bulk composition. Combining the two variables, the surface composition profiles under various conditions are shown in Figure 9.5. As a comparison, the surface composition profile of Pt-Ni alloy in vacuum is also included in the figure. In vacuum, Pt atoms are enriched in the first and third layer and are depleted in the subsurface layer as shown in Figure 9.5(a). When oxygen gas is presented in the environment, the surface composition is reversed. For $\Delta\mu_O = -3.425$ eV (shown in Figure 9.5(b)), Pt atoms are depleted in the outermost layer due to the stronger adsorption between Ni atom and O atom. The second layer is slightly Pt-enriched because the subsurface Pt atoms make the adsorption even more stronger on the surface Ni atoms. The third layer basically has the same composition to the bulk composition. With increasing oxygen chemical potential, Pt depletion in the first layer becomes

more and more pronounced. For example, for $\Delta\mu_O = -2.240$ eV (shown in Figure 9.5(d)), the outermost surface is covered with pure Ni atoms under the three different bulk composition tested. Under higher oxygen chemical potential, the second layer shows Pt-depletion in the subsurface layer in $Pt_{25}Ni_{75}$ alloy. For the other compositions, Pt enrichment in the subsurface layer is found.

The atomic structures of the surface-segregated $Pt_{75}Ni_{25}$ (111) surface and subsurface under various atmospheric environments are shown in Figure 9.6. In vacuum, surface-segregated $Pt_{75}Ni_{25}$ (111) surface has a nearly pure Pt cover and a mixing Pt-Ni subsurface with half Ni and half Pt atoms. The subsurface is not completely random but with some short-range ordering. With increased oxygen chemical potential, the Pt concentration decreases in the outermost surface but increases in the subsurface. At $\mu_O = -3.425$ eV, the outermost layer can be identified to have two types of regions. In the fisrt type, Ni atoms and Pt atoms are mixed. In the other type of regions, there are only Pt atoms in them. In the subsurface layer, underneath the first type of region, the region is basically coverred by pure Pt atoms. Underneath the second type of region, which is pure Pt in the outermost layer, the subsurface is a mixing of Ni and Pt atoms. For $\mu_O = --2.932$ eV, the outermost layer is a surface of mixing of Ni and Pt atoms and the subsurface is almost pure Pt. For $\mu_O = --2.240$ eV, an overlayer of Ni atoms formed on top of the Pt substrate.

9.6 CONCLUSION

In this work, we have studied the surface segregation process in Pt-Ni (111) surface in the atmosphere of oxygen gas by employing GCMC simulation. In order to describing the interaction in Pt-Ni-O system, we have developed interatomic potential for the system in the framework of MEAM. During the development process, we fitted the MEAM model to reproduce the oxygen binding energies on Pt (111), Ni (111), Pt/Ni (111), and Ni/Pt (111) surfaces with various oxygen coverages.

With a reasonable model of Pt-Ni-O system, GCMC simulations have been carried out to investigate the surface composition and structure of Pt-Ni (111) surface annealed in oxygen

environment. In the simulation, it has been shown Ni atoms would segregate to the outermost layer due to the strong binding between O adsorbates and surface Ni atoms, which is the reverse process of Pt surface segregation when the surface is annealed in vacuum. It is also demonstrated that equilibrium surface composition and structure of Pt-Ni (111) could be controlled by varying the Pt-Ni composition and partial pressure of oxygen gas (chemical potential of oxygen gas). For $Pt_{75}Ni_{25}$ alloy, the outermost layer covers by more and more Ni atoms with increasing oxygen partial pressure and finally forms an Ni overlayer. The subsurface, on the other hand, covers by more and more Pt atoms with increasing oxygen partial pressure.

In summary, we simulated the surface segregation phenomenon in Pt-Ni (111) surface under oxygen environment. The segregation of Ni atoms to the outermost surface explained one possibility of deactivation of Pt-Ni bimetallic catalysts. By controlling the Pt-Ni composition and oxygen partial pressure, the surface composition and structure could be manipulated to prepare bimetallic surface with different characteristics in catalytic reactivity.

10.0 SIMULATION STUDY OF ELECTROCHEMICAL DISSOLUTION PROCESS IN PLATINUM AND PLATINUM-GOLD NANOPARTICLES

10.1 ABSTRACT

In this work, the degradation of Pt nanoparticle catalyst through Pt dissolution is studied employing grand-canonical Monte Carlo (GCMC) simulation. Pt dissolution process was found to be initialized through the dissolution of under-coordinated Pt atoms sitting on the corners and edges of the nanoparticle. After the initial dissolution of Pt atoms on corners and edges, more under-coordinated Pt atoms are generated and the dissolution process is accelerating. The smaller Pt nanoparticle is more vulnerable to the Pt dissolution process than the larger nanoparticle. A Pt nanoparticle with about 5 nm diameter is stable in the environment. It was also found that Au atoms segregated to the under-coordinated sites would stabilize the nanoparticle because Au atoms will not dissolute and the dissolution process will not be initialized. The simulation explains the stabilizing effect of Au observed in the experiments.

10.2 INTRODUCTION

Proton-exchange membrane fuel cells (PEMFCs) draw intensive research interests in these years because of its promising role as an efficient alternative energy conversion device to substitute for traditional combustion engines. Numerous research efforts have been devoted to improve the reactivity of the catalyst in the cathode of PEMFCs due to the sluggish oxygen reduction reaction (ORR) on the surfaces of typical carbon supported Pt nanoparticles. [12,13]

Hence, in recent years, alloying Pt with transition metals as a method of modifying the reactivity of Pt catalysts have been extensively studied. However, although efficient catalysts could be prepared, degradation of the catalysts are often found during the service and hinders the deployment of PEMFCs. Especially in the cathode side, where the environment is highly oxidizing, even the most novel metal – platinum – could not remain stable in such drastic conditions.

The degradation of platinum nanoparticles supported on a carbon material is strongly dependent on the operating conditions, such as platinum loading, particle size, or spatial particle distribution, and the respective working electrode potentials, temperature, pH, and impurities as just some of the most important factors. A variety of helpful summaries on electrode catalyst stability provide an excellent overview of these aspects.[159–161] Especially, the dynamics during start-stop cycles of fuel cells were found to be extremely harmful to the catalyst and often have a dominant influence on its stability.[159] The main reason for the catalyst degradation is that the cathode potential can locally rise to values up to 1.5 V during the initial phase when the fuel gas purging is insufficient, causing aging of the carbon support as well as the platinum nanoparticles. The prevailing degradation mechanisms under these specific startstop conditions are only poorly understood, because of the inherent complexity of a multicomponent fuel cell system. Degradation mechanisms, such as particle agglomeration, detachment, platinum dissolution, and support corrosion may occur in the cathode electrode. Platinum dissolution as one of the main possible degradation mechanism is recently elaborated in the literature.[162] It has been found for dissolution process in Pt extended surfaces, a threshold electrode potential about 1.15 V_{RHE} exists. Besides, two possible dissolution mechanisms were identified. In the first mechanism, Pt dissolution occurs during the positive-going potential, which is attributed to the direct dissolution of Pt atoms. The second dissolution is more dominating occurs during the negative-going potential, which is proposed to be due to the dissolution of Pt oxide. Adzic et al. demonstrated that alloying Pt with Au could stabilize the electrocatalysts against dissolution under potential cycling without significant changes in the activity.[163]

In this work, we investigate Pt dissolution process in Pt nanoparticles and the stabilizing effect of Au with grand canonical Monte Carlo (GCMC) simulation. We developed

interatomic potential for Pt-Au alloy in the framework of MEAM. Surface segregation in the Pt-Au alloys is studied to obtain the knowledge of equilibrium surface composition and structure. Pt dissolution process is studied in atomic detail. Nanoparticle size dependence of Pt dissolution is also investigated. Stabilizing effect of Au in the surface-segregated Pt-Au nanoparticle is studied.

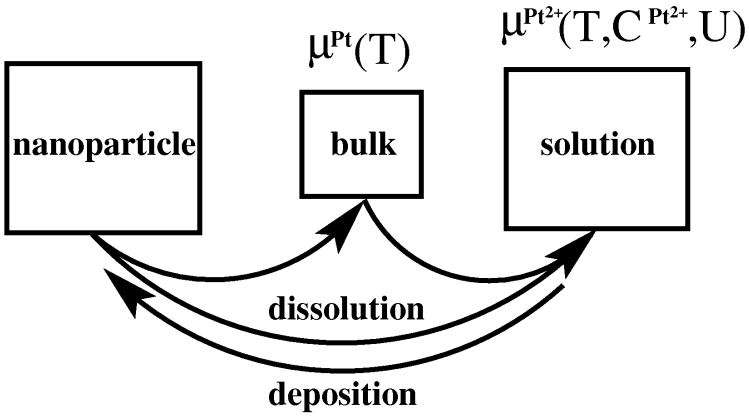

Figure 10.1: Schematic plot of the method used to calculate the chemical potential of Pt_2^+ ions.

10.3 COMPUTATIONAL METHODS

The Pt_2^+ ions have chemical potential $\mu^{Pt^{2+}}(T, C^{Pt^{2+}}, U)$ which is a function of temperature (T), concentration of Pt_2^+ ion ($C^{Pt^{2+}}$), and the electrode potential (U). In order to calculate $\mu^{Pt^{2+}}$, an imaginary route for the dissolution process is devised (see Fig.10.1. A detached Pt atom from the surface of a Pt nanoparticle firstly reaches a Pt bulk system with a chemical potential μ^{Pt}, which can be readily calculated. In the next step of the dissolution process, a Pt atom from the bulk is dissolved to Pt_2^+ solution. The chemical potential change during this dissolution process, $\Delta\mu$, can be calculated from the electrochemical reduction reaction

$Pt_2^+ + 2\,e^- \rightleftharpoons Pt$ and the standard electrode potential associated with it. As a result of the two-step route, $\mu^{Pt^{2+}}$ can be calculated as the sum of μ^{Pt} and $\Delta\mu$ (the minus sign is because dissolution process is the reverse of reduction reaction), i.e.

$$\mu^{Pt^{2+}} = \mu^{Pt} - \Delta\mu \tag{10.1}$$

μ^{Pt} is calculated within quasi-harmonic approximation by using the MEAM potential. The value of μ^{Pt} at the simulation temperature $T = 333$ K is -5.827 eV. On the other hand,

$$\Delta\mu = \Delta\mu^0 + k_B T \ln \frac{1}{C^{Pt^{2+}}} + 2eU \tag{10.2}$$

where $\Delta\mu_0$ is the Gibbs free-energy change under standard condition ($T = 298.15$ K, $\mu^{Pt^{2+}} =$ 1 M), k_B is Boltzmann constant, and e is the electron charge. The factor of 2 in the last term of Equ. 10.2 is because two electrons are transferred in the reaction. $\Delta\mu_0$ equals to -2.376 eV provided that the standard electrode potential of the Pt reduction reaction is 1.188 V. Additionally, by assuming $\mu^{Pt^{2+}}$ equals to 10^{-6} M, we can get

$$\mu^{Pt^{2+}} = -3.847 - 2eU \tag{10.3}$$

So, more positive the electrode potential is, more strong driving force will be for Pt atoms in nanoparticles to be dissolved. At low positive electrode potential or negative potential, deposition is more likely to happen.

In our GCMC simulation, we cycle the electrode potential in the range of 0.6 to 1.1 V. One complete cycle of electrode potential includes increasing from 0.6 to 1.1 V and decreasing back to 0.6 V with step size of 0.01 V. Along with the cycling of electrode potential, $\mu^{Pt^{2+}}$ also cycles according to Equ. 10.3. By doing so, we intend to simulate the cyclic voltammetry (CV) experiment. At each electrode potential point, we attempt one trial step to dissolve a randomly selected Pt atom from the surface or deposit a Pt atom to a randomly selected surface site. Among the trial steps, 99.8 % of the attempted steps are dissolution. The acceptance probability of dissolution and deposition are defined by

$$P(N \to N+1) = \min\left(1, \frac{V}{\Lambda^3(N+1)} \exp\left(\beta[\mu - \Delta E_{N+1,N}]\right)\right) \tag{10.4}$$

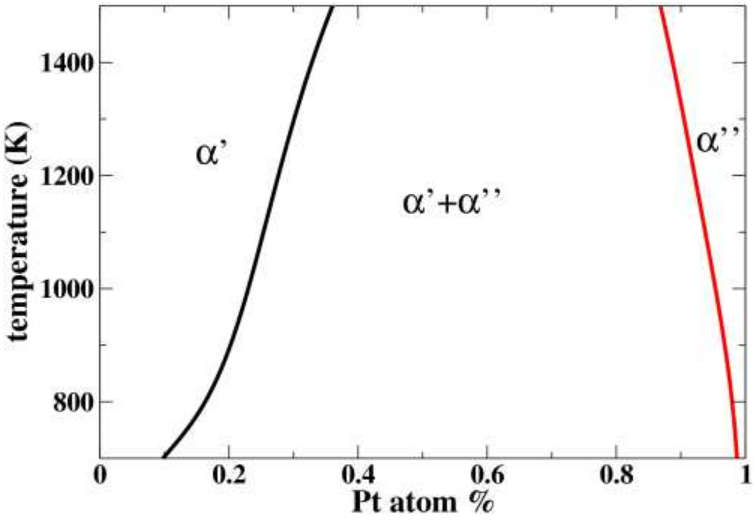

Figure 10.2: Calculated phase diagram of Pt-Au.

Table 10.1: Calculated surface segregation energies (in eV) for a Pt (or Au) impurity in the three low-index Au (or Pt) extended surfaces.

		Segregation energy (eV)			
		Au in Pt		Pt in Au	
surface	layer	MEAM	DFT	MEAM	DFT
(111)	1	-0.47	-0.46	0.25	0.34
	2	-0.11	-0.09	0.07	0.01
	3	0.00	-0.01	0.00	-0.04
(110)	1	-0.45	-0.68	0.32	0.45
	2	-0.32	-0.03	0.20	0.10
	3	-0.11	0.08	0.07	0.05
(100)	1	-0.58	-0.58	0.32	0.45
	2	-0.20	0.00	0.13	0.01
	3	0.00	0.00	0.00	-0.02

$$P(N \rightarrow N-1) = \min\left(1, \frac{\Lambda^3 N}{V} \exp\left(\beta[\mu + \Delta E_{N-1,N}]\right)\right) \tag{10.5}$$

Here, $\beta = 1/k_B T$ and $\Lambda = \sqrt{h^2/2\pi m k_B T}$ is the thermal de Broglie wavelength (h is Plank's constant and m is the particle mass). The potential energy of the system E is obtained from MEAM potential. In each simulation, we conducted 100 cycles, and the interested properties are averaged over 10 simulations with different random seeds.

Pt-Au MEAM potential was developed by fitting surface segregation energies in surfaces with different index calculated by using first-principles DFT method. The values of surface segregation energies are summarized in Tab. 10.1. The surface segregation energies suggest Au atoms would segregate to the surface and Pt atoms prefer staying in the bulk region. In Fig. 10.2, we calculated the phase diagram of bimetallic Pt-Au alloy. The phase boundaries are obtained by using adiabatic switching method[164], which is a method of free energy calculation. Our developed calculation could qualitatively capture the physics of Pt-Au alloy especially for the solubility of Au atoms in the Pt solvent as compared to experimetal phase diagram.[165]

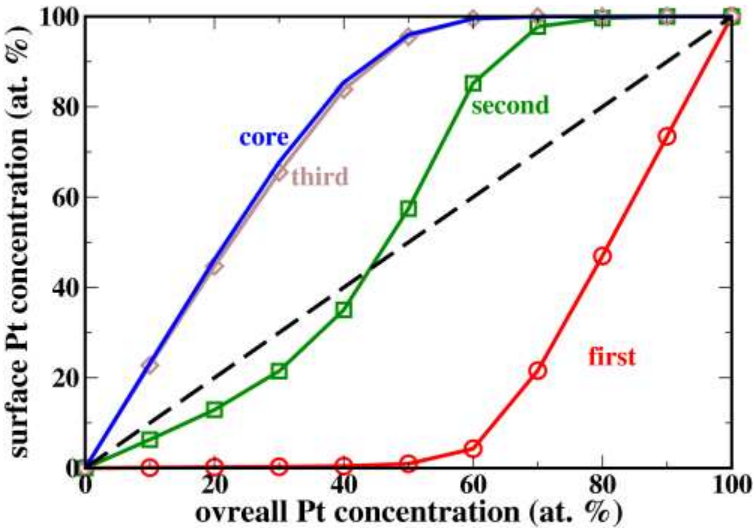

Figure 10.3: Surface composition profile of 3.5 nm Pt-Au nanoparticles with various overall composition.

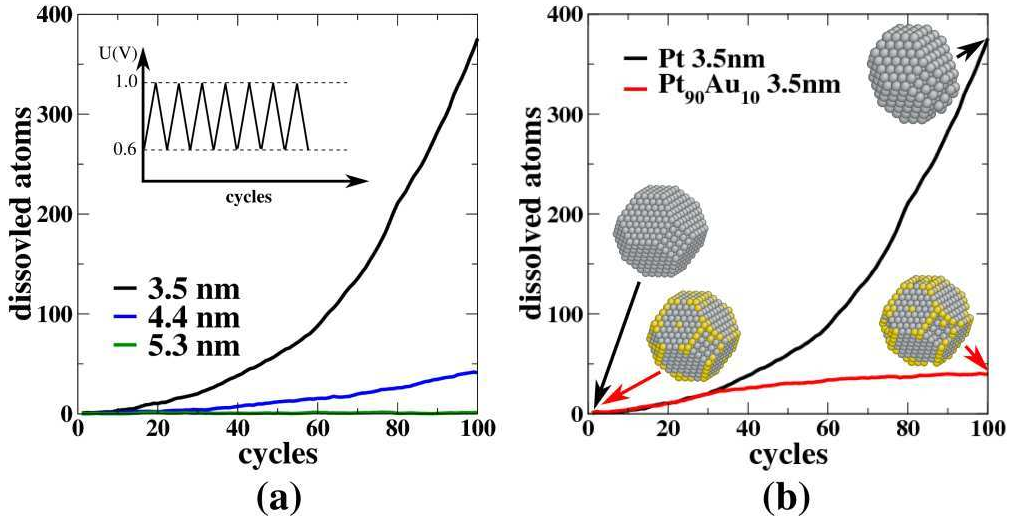

Figure 10.4: Comparison of dissolution process in Pt and $Pt_{90}Au_{10}$ nanoparticle.

10.4 RESULTS AND DISCUSSION

The surface composition profile of 3.5 nm Pt-Au nanoparticls is plotted in Fig. 10.3. The outermost surface is strongly enriched in Au due to the surface segregation. The core region of the nanoparticle, on the other hand, is enriched in Pt atoms. So, due to the surface segregation process, Au shell-Pt core nanoparticles are resulted. The second layer of the nanoparticle is firstly enriched in Au when the overall composition is lower than 40 at. % Pt. Higher than the composition, Pt is enriched in the subsurface. It is also found that the low-coordinated sites on the surface, such as corners and edges, are preferential for Au segregation.

Fig. 10.4 (a) shows the number of dissolved atoms as a function of number of cycles of applied cyclic electrode potential. In Pt nanoparticle with a diameter of 3.5 nm, significant amount of Pt atoms are dissolved and the velocity of dissolution is accelerating manifested by the increasing slope of the curve. It was found that the atoms in the corners and edges are the most vulnerable sites and the dissolution process starts from the dissolution of atoms in these sites. After initial dissolution of low-coordinated Pt atoms, more and more low-coordinated

Pt atoms are generated , which results in the acceleration of the dissolution process. In larger Pt nanoparticles, the dissolution is greatly depressed because larger nanoparticles are more thermodynamically stable. The dissolution process in 5.3 nm nanoparticle is practically not happening.

Dissolution process in surface segregated $Pt_{90}Au_{10}$ nanoparticle with a diameter of 3.5 nm is also simulated. The results are plotted in Fig. 10.4 (b) and the results for pure Pt are also included for comparison. The stabilizing effect of Au is obvious that after initial dissolution of several Pt atoms, the dissolution process is slowed since the slope of the curve become flat. The reason for the stabilizing effect is that segregated Au atoms occupy the low-coordinated sites on the surface and prevent the initialization of the Pt dissolution process since Au atoms have larger oxidizing potential than Pt atoms.

10.5 CONCLUSION

In this study, dissolution process in the Pt and Pt-Au nanoparticle electrocatalysts is studied by using GCMC simulation approach. Firstly, a Pt-Au binary interatomic potential is developed by fitting surface segregation energies for Au/Pt impurity in Pt/Au matrix calculated by quantum mechanical DFT calculations. The calculated binary Pt-Au phase diagram employing the developed MEAM potential is in agreement with experimental measurements. The equilibrium surface composition and structure of Pt-Au 3.5 nm nanoparticle is obtained by Monte Carlo simulations. The surface segregation process results in Au shell-Pt core Pt-Au nanoparticle. Au atoms are found prefer segregating to the low-coordinated surface sites. Pt dissolution in 3.5 nm pure Pt nanoparticle is found to be significant under cyclic electrode potential. The dissolution starts from the dissolution of low-coordinated Pt atoms (on corners and edges). The dissolution is accelerating because of more and more low-coordinated Pt atoms are generated after the initial dissolution of Pt atoms in corners and edges. Small amount of Au atoms can stabilize Pt nanoparticle through protecting the low-coordinated surface sites since Au atoms are more nobel and less vulnerable to the oxidizing environment.

APPENDIX

ABBREVIATIONS

PEMFC	Proton-Exchange Membrane Fuel Cell
MEA	Membrane Electrode Assembly
ORR	Oxygen Reduction Reaction
DFT	Density Functional Theory
MEAM	Modified Embeded-Atom Method
MC	Monte Carlo
GCMC	Grand-Canonical Monte Carlo
KMC	Kinetic Monte Carlo
CI-NEB	Climbing Image Nudged Elastic Band
ZPE	Zero-Point Energy
BEP	Brønsted-Evans-Polanyi

BIBLIOGRAPHY

[1] Energy information administration. international energy outlook 2011. May 2011, office of integrated analysis and forecasting, U. S. Department of Energy.

[2] Zhiyao Duan and Guofeng Wang. A first principles study of oxygen reduction reaction on a Pt(111) surface modified by a subsurface transition metal M (M = Ni, Co, or Fe). *Phys. Chem. Chem. Phys.*, 13:20178–20187, 2011.

[3] N.M. Marković and P.N. Ross Jr. Surface science studies of model fuel cell electrocatalysts. *Surface Science Reports*, 45(4–6):117–229, 2002.

[4] Rajesh Bashyam and Piotr Zelenay. A class of non-precious metal composite catalysts for fuel cells. *Nature*, 443:63–66, September 2006.

[5] Cicero W.B. Bezerra, Lei Zhang, Kunchan Lee, Hansan Liu, Aldaléa L.B. Marques, Edmar P. Marques, Haijiang Wang, and Jiujun Zhang. A review of Fe-N/C and Co-N/C catalysts for the oxygen reduction reaction. *Electrochimica Acta*, 53(15):4937–4951, 2008.

[6] Kuanping Gong, Feng Du, Zhenhai Xia, Michael Durstock, and Liming Dai. Nitrogen-doped carbon nanotube arrays with high electrocatalytic activity for oxygen reduction. *Science*, 323(5915):760–764, 2009.

[7] Yonghong Bing, Hansan Liu, Lei Zhang, Dave Ghosh, and Jiujun Zhang. Nanostructured Pt-alloy electrocatalysts for PEM fuel cell oxygen reduction reaction. *Chem. Soc. Rev.*, 39:2184–2202, 2010.

[8] Vojislav Stamenkovic, Bongjin Simon Mun, Karl J. J. Mayrhofer, Philip N. Ross, Nenad M. Markovic, Jan Rossmeisl, Jeff Greeley, and Jens K. Nørskov. Changing the activity of electrocatalysts for oxygen reduction by tuning the surface electronic structure. *Angewandte Chemie International Edition*, 45(18):2897–2901, 2006.

[9] J. Greeley, I. E. L. Stephens, A. S. Bondarenko, T. P. Johansson, H. A. Hansen, T. F. Jaramillo, J. Rossmeisl, I. Chorkendorff, and J. K. Nørskov. Alloys of platinum and early transition metals as oxygen reduction electrocatalysts. *Nature Chemistry*, 1:552, September 2009.

[10] R. R. Adzic, J. Zhang, K. Sasaki, M. B. Vukmirovic, M. Shao, J. X. Wang, A. U. Nilekar, M. Mavrikakis, J. A. Valerio, and F. Uribe. Platinum monolayer fuel cell electrocatalysts. *Topics in Catalysis*, 46(3-4):249–262, 2007.

[11] J. Zhang, Y. Mo, M. B. Vukmirovic, R. Klie, K. Sasaki, and R. R. Adzic. Platinum monolayer electrocatalysts for O_2 reduction: Pt monolayer on Pd(111) and on carbon-supported Pd nanoparticles. *The Journal of Physical Chemistry B*, 108(30):10955–10964, July 2004.

[12] Vojislav R. Stamenkovic, Ben Fowler, Bongjin Simon Mun, Guofeng Wang, Philip N. Ross, Christopher A. Lucas, and Nenad M. Marković. Improved oxygen reduction activity on $Pt_3Ni(111)$ via increased surface site availability. *Science*, 315(5811):493–497, January 2007.

[13] Vojislav R. Stamenkovic, Bongjin Simon Mun, Matthias Arenz, Karl J. J. Mayrhofer, Christopher A. Lucas, Guofeng Wang, Philip N. Ross, and Nenad M. Markovic. Trends in electrocatalysis on extended and nanoscale Pt-bimetallic alloy surfaces. *Nature Materials*, 6(3):241–247, 2007.

[14] B. Hammer, J. K. Nørskov, and Helmut Knozinger Bruce C. Gates. Theoretical surface science and catalysis–calculations and concepts. In *Impact of Surface Science on Catalysis*, volume Volume 45, pages 71–129. Academic Press, 2000.

[15] J. R. Kitchin, J. K. Nørskov, M. A. Barteau, and J. G. Chen. Modification of the surface electronic and chemical properties of Pt(111) by subsurface 3d transition metals. *The Journal of Chemical Physics*, 120(21):10240, 2004.

[16] J. R. Kitchin, J. K. Nørskov, M. A. Barteau, and J. G. Chen. Role of strain and ligand effects in the modification of the electronic and chemical properties of bimetallic surfaces. *Physical Review Letters*, 93(15):156801, 2004.

[17] Timo Jacob, Richard P. Muller, and William A. Goddard. Chemisorption of atomic oxygen on Pt(111) from DFT studies of Pt-clusters. *The Journal of Physical Chemistry B*, 107(35):9465–9476, 2003.

[18] Ye Xu, Andrei V. Ruban, and Manos Mavrikakis. Adsorption and dissociation of O_2 on Pt-Co and Pt-Fe alloys. *Journal of the American Chemical Society*, 126(14):4717–4725, April 2004.

[19] Jerome Roques and Alfred B. Anderson. Electrode Potential-Dependent stages in OH_{ads} formation on the Pt_3Cr alloy (111) surface. *Journal of The Electrochemical Society*, 151(11):E340–E347, November 2004.

[20] Jerome Roques and Alfred B. Anderson. Cobalt concentration effect in $Pt_{1-x}Co_x$ on the reversible potential for forming OH_{ads} from H_2O_{ads} in acid solution. *Surface Science*, 581(2-3):105–117, May 2005.

[21] T. Jacob. The mechanism of forming H_2O from H_2 and O_2 over a Pt catalyst via direct oxygen reduction. *Fuel Cells*, 6(3-4):159–181, 2006.

[22] Matthew P. Hyman and J. Will Medlin. Effects of electronic structure modifications on the adsorption of oxygen reduction reaction intermediates on model Pt(111)-alloy surfaces. *The Journal of Physical Chemistry C*, 111(45):17052–17060, November 2007.

[23] Yuguang Ma and Perla B. Balbuena. Surface properties and dissolution trends of Pt_3M alloys in the presence of adsorbates. *The Journal of Physical Chemistry C*, 112(37):14520–14528, 2008.

[24] Anand Udaykumar Nilekar and Manos Mavrikakis. Improved oxygen reduction reactivity of platinum monolayers on transition metal surfaces. *Surface Science*, 602(14):L89–L94, July 2008.

[25] F. Abild-Pedersen, J. Greeley, F. Studt, J. Rossmeisl, T. R. Munter, P. G. Moses, E. Skúlason, T. Bligaard, and J. K. Nørskov. Scaling properties of adsorption energies for Hydrogen-Containing molecules on Transition-Metal surfaces. *Physical Review Letters*, 99(1):016105, July 2007.

[26] J. K. Nørskov, J. Rossmeisl, A. Logadottir, L. Lindqvist, J. R. Kitchin, T. Bligaard, and H. Jónsson. Origin of the overpotential for oxygen reduction at a fuel-cell cathode. *The Journal of Physical Chemistry B*, 108(46):17886–17892, November 2004.

[27] Graeme Henkelman, Blas P. Uberuaga, and Hannes Jónsson. A climbing image nudged elastic band method for finding saddle points and minimum energy paths. *The Journal of Chemical Physics*, 113(22):9901, 2000.

[28] Graeme Henkelman and Hannes Jónsson. Improved tangent estimate in the nudged elastic band method for finding minimum energy paths and saddle points. *The Journal of Chemical Physics*, 113(22):9978, 2000.

[29] Liang Qi, Jianguo Yu, and Ju Li. Coverage dependence and hydroperoxyl-mediated pathway of catalytic water formation on Pt (111) surface. *The Journal of Chemical Physics*, 125(5):054701, 2006.

[30] Matthew P. Hyman and J. Will Medlin. Mechanistic study of the electrochemical oxygen reduction reaction on Pt(111) using density functional theory. *The Journal of Physical Chemistry B*, 110(31):15338–15344, 2006.

[31] Sally A. Wasileski and Michael J. Janik. A first-principles study of molecular oxygen dissociation at an electrode surface: a comparison of potential variation and coadsorption effects. *Physical Chemistry Chemical Physics*, 10(25):3613, 2008.

[32] Michael J. Janik, Christopher D. Taylor, and Matthew Neurock. First-Principles analysis of the initial electroreduction steps of oxygen over Pt(111). *Journal of The Electrochemical Society*, 156(1):B126–B135, January 2009.

[33] Wenjie Tang and Graeme Henkelman. Charge redistribution in core-shell nanoparticles to promote oxygen reduction. *The Journal of Chemical Physics*, 130(19):194504, 2009.

[34] Denise C. Ford, Anand Udaykumar Nilekar, Ye Xu, and Manos Mavrikakis. Partial and complete reduction of O_2 by hydrogen on transition metal surfaces. *Surface Science*, 604(19–20):1565–1575, September 2010.

[35] D.S. Sholl and J.A. Steckel. *Density Functional Theory: A Practical Introduction*. John Wiley and Sons, Hoboken, New Jersey, 2009.

[36] R.M. Martin. *Electronic Structure: Basic Theory and Practical Methods*. Cambridge University Press, Cambridge, UK, 2004.

[37] K. Honkala, A. Hellman, I. N. Remediakis, A. Logadottir, A. Carlsson, S. Dahl, C. H. Christensen, and J. K. Nørskov. Ammonia synthesis from first-principles calculations. *Science*, 307(5709):555–558, 2005.

[38] Rainer Schweinfest, Anthony T. Paxton, and Michael W. Finnis. Bismuth embrittlement of copper is an atomic size effect. *Nature*, 432:1008–1011, 2004.

[39] Koichiro Umemoto, Renata M. Wentzcovitch, and Philip B. Allen. Dissociation of $MgSiO_3$ in the cores of gas giants and terrestrial exoplanets. *Science*, 311(5763):983–986, 2006.

[40] P. Hohenberg and W. Kohn. Inhomogeneous electron gas. *Phys. Rev.*, 136:B864–B871, Nov 1964.

[41] W. Kohn and L. J. Sham. Self-consistent equations including exchange and correlation effects. *Phys. Rev.*, 140:A1133–A1138, 1965.

[42] John P. Perdew and Yue Wang. Accurate and simple analytic representation of the electron-gas correlation energy. *Physical Review B*, 45(23):13244, June 1992.

[43] John P. Perdew, Kieron Burke, and Matthias Ernzerhof. Generalized gradient approximation made simple. *Phys. Rev. Lett.*, 77:3865–3868, 1996.

[44] M. I. Baskes. Modified embedded-atom potentials for cubic materials and impurities. *Phys. Rev. B*, 46:2727–2742, Aug 1992.

[45] M I Baskes and R A Johnson. Modified embedded atom potentials for hcp metals. *Modelling and Simulation in Materials Science and Engineering*, 2(1):147, 1994.

[46] M.I. Baskes. Atomistic potentials for the molybdenum-silicon system. *Materials Science and Engineering: A*, 261(1–2):165–168, 1999.

[47] M.I. Baskes. Determination of modified embedded atom method parameters for nickel. *Materials Chemistry and Physics*, 50(2):152–158, 1997.

[48] James H. Rose, John R. Smith, Francisco Guinea, and John Ferrante. Universal features of the equation of state of metals. *Phys. Rev. B*, 29:2963–2969, Mar 1984.

[49] P. A. Dowben and W. A. Miller. *Surface Segregation Phenomena*. CRC, Boca Raton, FL, 1990.

[50] José A. Rodriguez. Physical and chemical properties of bimetallic surfaces. *Surface Science Reports*, 24(7–8):223–287, 1996.

[51] Micha Polak and Leonid Rubinovich. The interplay of surface segregation and atomic order in alloys. *Surface Science Reports*, 38(4–5):127–194, 2000.

[52] L. V. Pourovskii, A. V. Ruban, B. Johansson, and I. A. Abrikosov. Antisite-defect-induced surface segregation in ordered NiPt alloy. *Phys. Rev. Lett.*, 90:026105, Jan 2003.

[53] Frank L. Williams and D. Nason. Binary alloy surface compositions from bulk alloy thermodynamic data. *Surface Science*, 45(2):377–408, 1974.

[54] M.J. Kelley and V. Ponec. Surface composition of alloys. *Progress in Surface Science*, 11(3):139–244, 1981.

[55] S. Mukherjee and J.L. Morán-López. Theory of surface segregation in transition-metal alloys. *Surface Science*, 188(3):L742–L748, 1987.

[56] A. V. Ruban, H. L. Skriver, and J. K. Nørskov. Surface segregation energies in transition-metal alloys. *Phys. Rev. B*, 59:15990–16000, Jun 1999.

[57] Guofeng Wang, M. A. Van Hove, P. N. Ross, and M. I. Baskes. Monte Carlo simulations of segregation in Pt-Ni catalyst nanoparticles. *The Journal of Chemical Physics*, 122(2):024706, 2005.

[58] Guofeng Wang, M. A. Van Hove, P. N. Ross, and M. I. Baskes. Monte Carlo simulations of segregation in Pt-Re catalyst nanoparticles. *The Journal of Chemical Physics*, 121(11):5410–5422, 2004.

[59] Guofeng Wang, M. A. Van Hove, P. N. Ross, and M. I. Baskes. Surface structures of Cubo-Octahedral Pt-Mo catalyst nanoparticles from Monte Carlo simulations. *The Journal of Physical Chemistry B*, 109(23):11683–11692, June 2005.

[60] Guofeng Wang, M.A. Van Hove, P.N. Ross, and M.I. Baskes. Quantitative prediction of surface segregation in bimetallic Pt-M alloy nanoparticles (M = Ni, Re, Mo). *Progress in Surface Science*, 79(1):28–45, 2005.

[61] Sanjeev Mukerjee, Supramaniam Srinivasan, Manuel P. Soriaga, and James McBreen. Effect of preparation conditions of pt alloys on their electronic, structural, and electrocatalytic activities for oxygen reduction - xrd, xas, and electrochemical studies. *The Journal of Physical Chemistry*, 99(13):4577–4589, 1995.

[62] U. A. Paulus, A. Wokaun, G. G. Scherer, T. J. Schmidt, V. Stamenkovic, V. Radmilovic, N. M. Markovic, and P. N. Ross. Oxygen reduction on carbon-supported Pt–Ni and Pt–Co alloy catalysts. *The Journal of Physical Chemistry B*, 106(16):4181–4191, 2002.

[63] Bongjin Simon Mun, Masamitsu Watanabe, Massimiliano Rossi, Vojislav Stamenkovic, Nenad M. Markovic, and Jr. Philip N. Ross. A study of electronic structures of Pt_3M (M = Ti,V,Cr,Fe,Co,Ni) polycrystalline alloys with valence-band photoemission spectroscopy. *The Journal of Chemical Physics*, 123(20):204717, 2005.

[64] Vojislav R. Stamenkovic, Bongjin Simon Mun, Karl J. J. Mayrhofer, Philip N. Ross, and Nenad M. Markovic. Effect of surface composition on electronic structure, stability, and electrocatalytic properties of Pt-transition metal alloys:Pt-skin versus Pt-skeleton surfaces. *Journal of the American Chemical Society*, 128(27):8813–8819, 2006.

[65] Wei-Ping Zhou, Xiaofang Yang, Miomir B. Vukmirovic, Bruce E. Koel, Jiao Jiao, Guowen Peng, Manos Mavrikakis, and Radoslav R. Adzic. Improving electrocatalysts for o_2 reduction by fine-tuning the Pt-support interaction: Pt monolayer on the surfaces of a $Pd_3Fe(111)$ single-crystal alloy. *Journal of the American Chemical Society*, 131(35):12755–12762, 2009.

[66] T. He, E. Kreidlera, L. Xionga, J. Luob, and C. J. Zhong. Alloy electrocatalysts–combinatorial discovery and nanosynthesis. *Journal of The Electrochemical Society*, 153(9):A1637–A1643, 2006.

[67] Errun Ding, Karren L. More, and Ting He. Preparation and characterization of carbon-supported PtTi alloy electrocatalysts. *Journal of Power Sources*, 175(2):794–799, 2008.

[68] W. Chen, J. A. K. Paul, A. Barbieri, M. A. Van Hove, S. Cameron, and D. J. Dwyer. Structure determination of $Pt_3Ti(111)$ by automated tensor LEED. *Journal of Physics: Condensed Matter*, 5(27):4585, 1993.

[69] A. Atrei, L. Pedocchi, U. Bardi, G. Rovida, M. Torrini, E. Zanazzi, M.A. Van Hove, and P.N. Ross. LEED structural analysis of the (001) surface of the ordered fcc Pt_3Ti alloy. *Surface Science*, 261(1–3):64–68, 1992.

[70] Yuguang Ma and Perla B. Balbuena. Pt surface segregation in bimetallic Pt_3M alloys: A density functional theory study. *Surface Science*, 602(1):107–113, 2008.

[71] G. Kresse and J. Hafner. Ab initio molecular dynamics for liquid metals. *Physical Review B*, 47(1):558, January 1993.

[72] G. Kresse and J. Furthmüller. Efficiency of ab-initio total energy calculations for metals and semiconductors using a plane-wave basis set. *Computational Materials Science*, 6(1):15–50, July 1996.

[73] P. E. Blöchl. Projector augmented-wave method. *Phys. Rev. B*, 50:17953–17979, Dec 1994.

[74] R. O. Jones and O. Gunnarsson. The density functional formalism, its applications and prospects. *Rev. Mod. Phys.*, 61:689–746, 1989.

[75] Hendrik J. Monkhorst and James D. Pack. Special points for brillouin-zone integrations. *Physical Review B*, 13(12):5188, June 1976.

[76] N. Metropolis, A. W. Rosenbluth, M. N. Rosenbluth, A. H. Teller, and E. Teller. Equation of state calculations by fast computing machines. *The Journal of Chemical Physics*, 21(6):1087, March 1953.

[77] P. Deurinck and C. Creemers. Face-related segregation reversal at $Pt_{50}Ni_{50}$ surfaces studied with the embedded atom method. *Surface Science*, 441(2–3):493–506, 1999.

[78] S. M. Foiles. Calculation of the surface segregation of Ni–Cu alloys with the use of the embedded-atom method. *Phys. Rev. B*, 32:7685–7693, Dec 1985.

[79] Xiang-Yang Liu, P.P. Ohotnicky, J.B. Adams, C.Lane Rohrer, and R.W. Hyland Jr. Anisotropic surface segregation in Al-Mg alloys. *Surface Science*, 373(2–3):357–370, 1997.

[80] U. Bardi and P.N. Ross. Superlattice LEED patterns observed from [111] and [100] oriented single crystals of $TiPt_3$. *Surface Science*, 146(1):L555–L560, 1984.

[81] A. V. Ruban. Surface composition of ordered alloys: An off-stoichiometric effect. *Phys. Rev. B*, 65:174201, Apr 2002.

[82] L. Vitos, A.V. Ruban, H.L. Skriver, and J. Kollár. The surface energy of metals. *Surface Science*, 411(1–2):186–202, 1998.

[83] H. Okamoto. Pt-Ti (Platinum-Titanium). *Journal of Phase Equilibria and Diffusion*, 30(2):217–218, Feburary 2009.

[84] P. T. Mescher and W. L. Worrel. *Metall. Trans.*, 7A:299, 1976.

[85] P Deurinck and C Creemers. Monte Carlo simulation of Cu segregation and ordering at the (110) surface of $Cu_{75}Pd_{25}$. *Surface Science*, 419(1):62–77, 1998.

[86] Amdulla O Mekhrabov and M Vedat Akdeniz. Modelling and Monte Carlo simulation of the atomic ordering processes in Ni_3Al intermetallics. *Modelling and Simulation in Materials Science and Engineering*, 15(2):1, 2007.

[87] Byungkwon Lim, Majiong Jiang, Pedro H. C. Camargo, Eun Chul Cho, Jing Tao, Xianmao Lu, Yimei Zhu, and Younan Xia. Pd–Pt bimetallic nanodendrites with high activity for oxygen reduction. *Science*, 324(5932):1302–1305, 2009.

[88] Jason R. Croy, S. Mostafa, L. Hickman, H. Heinrich, and B. Roldan Cuenya. Bimetallic Pt-metal catalysts for the decomposition of methanol: Effect of secondary metal on the oxidation state, activity, and selectivity of pt. *Applied Catalysis A: General*, 350(2):207–216, 2008.

[89] B Pawelec, R Mariscal, R.M Navarro, S van Bokhorst, S Rojas, and J.L.G Fierro. Hydrogenation of aromatics over supported Pt-Pd catalysts. *Applied Catalysis A: General*, 225(1–2):223–237, 2002.

[90] L. C. A. van den Oetelaar, O. W. Nooij, S. Oerlemans, A. W. Denier van der Gon, H. H. Brongersma, L. Lefferts, A. G. Roosenbrand, and J. A. R. van Veen. Surface segregation in supported Pd-Pt nanoclusters and alloys. *The Journal of Physical Chemistry B*, 102(18):3445–3455, 1998.

[91] J. L. Rousset, A. J. Renouprez, and A. M. Cadrot. Ion-scattering study and Monte Carlo simulations of surface segregation in Pd-Pt nanoclusters obtained by laser vaporization of bulk alloys. *Phys. Rev. B*, 58:2150–2156, Jul 1998.

[92] Poul L. Hansen, Alfons M. Molenbroek, and Andrei V. Ruban. Alloy formation and surface segregation in Zeolite-Supported Pt-Pd bimetallic catalysts. *The Journal of Physical Chemistry B*, 101(10):1861–1868, 1997.

[93] Huiqiu Deng, Wangyu Hu, Xiaolin Shu, Lihua Zhao, and Bangwei Zhang. Monte Carlo simulation of the surface segregation of Pt–Pd and Pt–Ir alloys with an analytic embedded-atom method. *Surface Science*, 517(1–3):177–185, 2002.

[94] Lesley D. Lloyd, Roy L. Johnston, Said Salhi, and Nicholas T. Wilson. Theoretical investigation of isomer stability in platinum-palladium nanoalloy clusters. *J. Mater. Chem.*, 14:1691–1704, 2004.

[95] Subramanian K. R. S. Sankaranarayanan, Venkat R. Bhethanabotla, and Babu Joseph. Molecular dynamics simulation study of the melting of Pd-Pt nanoclusters. *Phys. Rev. B*, 71:195415, May 2005.

[96] G. E. Ramirez Caballero and P. B. Balbuena. Surface segregation phenomena in Pt-Pd nanoparticles: dependence on nanocluster size. *Molecular Simulation*, 32(3–4):297–303, 2006.

[97] Chao Wang, Dennis van der Vliet, Karren L. More, Nestor J. Zaluzec, Sheng Peng, Shouheng Sun, Hideo Daimon, Guofeng Wang, Jeffrey Greeley, John Pearson, Arvydas P. Paulikas, Goran Karapetrov, Dusan Strmcnik, Nenad M. Markovic, and Vojislav R. Stamenkovic. Multimetallic Au/$FePt_3$ nanoparticles as highly durable electrocatalyst. *Nano Letters*, 11(3):919–926, 2011.

[98] Junliang Zhang, Miomir B. Vukmirovic, Ye Xu, Manos Mavrikakis, and Radoslav R. Adzic. Controlling the catalytic activity of platinum-monolayer electrocatalysts for

oxygen reduction with different substrates. *Angewandte Chemie International Edition*, 44(14):2132–2135, 2005.

[99] Byeong-Joo Lee and M. I. Baskes. Second nearest-neighbor modified embedded-atom-method potential. *Phys. Rev. B*, 62:8564–8567, Oct 2000.

[100] Zhiyao Duan, Jun Zhong, and Guofeng Wang. Modeling surface segregation phenomena in the (111) surface of ordered Pt_3Ti crystal. *The Journal of Chemical Physics*, 133(11):114701, 2010.

[101] W.R. Tyson and W.A. Miller. Surface free energies of solid metals: Estimation from liquid surface tension measurements. *Surface Science*, 62(1):267–276, 1977.

[102] F. R. de Boer, R. Boom, W. C. Matterns, A. R. Miedema, and A. K. Niessen. *Cohesion in metals*. North-Holland, Amsterdam, 1988.

[103] David J. Watson and Gary A. Attard. The electro-oxidation of glucose using platinumcpalladium bulk alloy single crystals. *Electrochimica Acta*, 46(20–21):3157–3161, 2001.

[104] D.J Watson and G.A Attard. Surface segregation and reconstructive behaviour of the (100) and (110) surfaces of platinum–palladium bulk alloy single crystals: a voltammetric and LEED/AES study. *Surface Science*, 515(1):87–93, 2002.

[105] W. B. Pearson. *A Handbook of Lattice Spacings and Structures of Metals and Alloys*. Pergamon, New York, 1964.

[106] U Bardi. The atomic structure of alloy surfaces and surface alloys. *Reports on Progress in Physics*, 57(10):939, 1994.

[107] Takako Toda, Hiroshi Igarashi, and Masahiro Watanabe. Enhancement of the electrocatalytic O_2 reduction on Pt–Fe alloys. *Journal of Electroanalytical Chemistry*, 460(1-2):258 – 262, 1999.

[108] AnandUdaykumar Nilekar, Ye Xu, Junliang Zhang, Miomir B. Vukmirovic, Kotaro Sasaki, Radoslav R. Adzic, and Manos Mavrikakis. Bimetallic and ternary alloys for improved oxygen reduction catalysis. *Topics in Catalysis*, 46(3–4):276–284, 2007.

[109] Chao Wang, Nenad M. Markovic, and Vojislav R. Stamenkovic. Advanced platinum alloy electrocatalysts for the oxygen reduction reaction. *ACS Catalysis*, 2(5):891–898, 2012.

[110] Mingshu Chen, Dheeraj Kumar, Cheol-Woo Yi, and D. Wayne Goodman. The promotional effect of gold in catalysis by palladium-gold. *Science*, 310(5746):291–293, 2005.

[111] M A Vasiliev. Surface effects of ordering in binary alloys. *Journal of Physics D: Applied Physics*, 30(22):3037, 1997.

[112] Patrik Fredriksson and Bo Sundman. A thermodynamic assessment of the Fe-Pt system. *Calphad*, 25(4):535–548, 2001.

[113] R. Baudoing-Savois, Y. Gauthier, and W. Moritz. Segregation and ordering at the (1×2) reconstructed $Pt_{80}Fe_{20}(110)$ surface determined by low-energy electron diffraction. *Phys. Rev. B*, 44:12977–12990, Dec 1991.

[114] Mickey C. Y. Chan, Liang Chen, Feihong Nan, James F. Britten, Christina Bock, and Gianluigi A. Botton. Structure, ordering, and surfaces of Pt-Fe alloy catalytic nanoparticles from quantitative electron microscopy and x-ray diffraction. *Nanoscale*, 4:7273–7279, 2012.

[115] V. Blum, L. Hammer, Ch. Schmidt, W. Meier, O. Wieckhorst, S. Müller, and K. Heinz. Segregation in strongly ordering compounds: A key role of constitutional defects. *Phys. Rev. Lett.*, 89:266102, Dec 2002.

[116] Michael Müller and Karsten Albe. Lattice Monte Carlo simulations of FePt nanoparticles: Influence of size, composition, and surface segregation on order-disorder phenomena. *Phys. Rev. B*, 72:094203, 2005.

[117] Roman V. Chepulskii, W.H. Butler, A. van de Walle, and Stefano Curtarolo. Surface segregation in nanoparticles from first principles: The case of fept. *Scripta Materialia*, 62(4):179–182, 2010.

[118] C. Creemers, P. Deurinck, S. Helfensteyn, and J. Luyten. Segregation and ordering at alloys surfaces: modelling and experiment confronted. *Applied Surface Science*, 219(1–2):11–27, 2003.

[119] Wei Chen, P. Dalach, William F. Schneider, and C. Wolverton. Interplay between subsurface ordering, surface segregation, and adsorption on Pt–Ti(111) near-surface alloys. *Langmuir*, 28(10):4683–4693, 2012.

[120] P. Modrak. Electronic theory of surface segregation in binary transition metal alloys. *Progress in Surface Science*, 49(3):227–264, 1995.

[121] G. Kresse and D. Joubert. From ultrasoft pseudopotentials to the projector augmented-wave method. *Physical Review B*, 59(3):1758, January 1999.

[122] B. Wang, D. C. Berry, Y. Chiari, and K. Barmak. Experimental measurements of the heats of formation of Fe_3Pt, FePt, and $FePt_3$ using differential scanning calorimetry. *Journal of Applied Physics*, 110(1):013903, 2011.

[123] Jaesong Kim, Yangmo Koo, and Byeong-Joo Lee. Modified embedded-atom method interatomic potential for the Fe–Pt alloy system. *Journal of Materials Research*, 21:199–208, 0 2006.

[124] P. Beccat, Y. Gauthier, R. Baudoing-Savois, and J.C. Bertolni. Monotonous concentration profile and reconstruction at $Pt_{80}Fe_{20}(111)$: LEED study of a catalyst. *Surface Science*, 238(1–3):105–118, 1990.

[125] C. Creemers and P. Deurinck. Platinum segregation to the (111) surface of ordered $Pt_{80}Fe_{20}$: LEIS results and model simulations. *Surface and Interface Analysis*, 25(3):177–190, 1997.

[126] M. Z. Jacobson, W. G. Colella, and D. M. Golden. Cleaning the air and improving health with hydrogen fuel-cell vehicles. *Science*, 308(5730):1901–1905, 2005.

[127] Graeme Henkelman, Andri Arnaldsson, and Hannes Jónsson. Theoretical calculations of CH_4 and H_2 associative desorption from Ni(111): Could subsurface hydrogen play an important role? *The Journal of Chemical Physics*, 124(4):044706, 2006.

[128] Andrew P. Graham, Alexander Menzel, and J. Peter Toennies. Quasielastic helium atom scattering measurements of microscopic diffusional dynamics of H and D on the Pt(111) surface. *The Journal of Chemical Physics*, 111(4):1676–1685, 1999.

[129] Bădescu. S. C., P. Salo, T. Ala-Nissila, S. C. Ying, K. Jacobi, Y. Wang, K. Bedürftig, and G. Ertl. Energetics and vibrational states for hydrogen on Pt(111). *Physical Review Letters*, 88(13):136101, Mar 2002.

[130] Yao Sha, Ted H. Yu, Yi Liu, Boris V. Merinov, and William A. Goddard. Theoretical study of solvent effects on the platinum-catalyzed oxygen reduction reaction. *The Journal of Physical Chemistry Letters*, 1(5):856–861, 2010.

[131] B. Hammer and J. K. Nørskov. Electronic factors determining the reactivity of metal surfaces. *Surface Science*, 343(3):211–220, December 1995.

[132] J. N. Bronsted. Acid and basic catalysis. *Chemical Reviews*, 5(3):231–338, 1928.

[133] M. G. Evans and M. Polanyi. Inertia and driving force of chemical reactions. *Transactions of the Faraday Society*, 34:11–24, 1938.

[134] Rutger A van Santen and Matthew Neurock. *Molecular Heterogeneous Catalysis: A Conceptual and Computational Approach*. Wiley-VCH, 2006.

[135] Hubert A. Gasteiger and Nenad M Marković. Just a dream-or future reality? *Science*, 324(5923):48–49, 2009.

[136] Jin Luo, Lingyan Wang, Derrick Mott, Peter N. Njoki, Nancy Kariuki, Chuan-Jian Zhong, and T. He. Ternary alloy nanoparticles with controllable sizes and composition and electrocatalytic activity. *J. Mater. Chem.*, 16:1665–1673, 2006.

[137] Chao Wang, Dongguo Li, Miaofang Chi, John Pearson, Rees B. Rankin, Jeff Greeley, Zhiyao Duan, Guofeng Wang, Dennis van der Vliet, Karren L. More, Nenad M.

Markovic, and Vojislav R. Stamenkovic. Rational development of ternary alloy electrocatalysts. *The Journal of Physical Chemistry Letters*, 3(12):1668–1673, 2012.

[138] Na Tian, Zhi-You Zhou, Shi-Gang Sun, Yong Ding, and Zhong Lin Wang. Synthesis of tetrahexahedral platinum nanocrystals with high-index facets and high electrooxidation activity. *Science*, 316(5825):732–735, 2007.

[139] Nenad M. Markovic, Hubert A. Gasteiger, and Philip N. Ross. Oxygen reduction on platinum low-index single-crystal surfaces in sulfuric acid solution: Rotating ring-Pt(hkl) disk studies. *The Journal of Physical Chemistry*, 99(11):3411–3415, 1995.

[140] Nenad Markovic, Hubert Gasteiger, and Philip N. Ross. Kinetics of oxygen reduction on pt(hkl) electrodes: Implications for the crystallite size effect with supported pt electrocatalysts. *Journal of The Electrochemical Society*, 144(5):1591–1597, 1997.

[141] Jun Zhang, Hongzhou Yang, Jiye Fang, and Shouzhong Zou. Synthesis and oxygen reduction activity of shape-controlled pt3ni nanopolyhedra. *Nano Letters*, 10(2):638–644, 2010.

[142] Taekyung Yu, Do Youb Kim, Hui Zhang, and Younan Xia. Platinum concave nanocubes with high-index facets and their enhanced activity for oxygen reduction reaction. *Angewandte Chemie International Edition*, 50(12):2773–2777, 2011.

[143] Sang-Il Choi, Ran Choi, Sang Woo Han, and Joon T. Park. Shape-controlled synthesis of Pt_3Co nanocrystals with high electrocatalytic activity toward oxygen reduction. *Chemistry–A European Journal*, 17(44):12280–12284, 2011.

[144] Yijin Kang and Christopher B. Murray. Synthesis and electrocatalytic properties of cubic Mn–Pt nanocrystals (nanocubes). *Journal of the American Chemical Society*, 132(22):7568–7569, 2010.

[145] Da-Jiang Liu and James W. Evans. Interactions between oxygen atoms on Pt(100): Implications for ordering during chemisorption and catalysis. *ChemPhysChem*, 11(10):2174–2181, 2010.

[146] John A. Keith and Timo Jacob. Theoretical studies of potential-dependent and competing mechanisms of the electrocatalytic oxygen reduction reaction on Pt(111). *Angewandte Chemie International Edition*, 49(49):9521–9525, 2010.

[147] A. Panchenko, M. T. M. Koper, T. E. Shubina, S. J. Mitchell, and E. Roduner. Ab initio calculations of intermediates of oxygen reduction on low-index platinum surfaces. *Journal of The Electrochemical Society*, 151(12):A2016–A2027, 2004.

[148] Timo Jacob and William A. Goddard. Water formation on pt and pt-based alloys: A theoretical description of a catalytic reaction. *ChemPhysChem*, 7(5):992–1005, 2006.

[149] John A. Keith, Gregory Jerkiewicz, and Timo Jacob. Theoretical investigations of the oxygen reduction reaction on Pt(111). *ChemPhysChem*, 11(13):2779–2794, 2010.

[150] Vladimir Tripković, Egill Skúlason, Samira Siahrostami, Jens K. Nørskov, and Jan Rossmeisl. The oxygen reduction reaction mechanism on Pt(111) from density functional theory calculations. *Electrochimica Acta*, 55(27):7975–7981, 2010.

[151] Yao Sha, Ted H. Yu, Boris V. Merinov, Pezhman Shirvanian, and William A. Goddard. Oxygen hydration mechanism for the oxygen reduction reaction at Pt and Pd fuel cell catalysts. *The Journal of Physical Chemistry Letters*, 2(6):572–576, 2011.

[152] Nuria Garcia-Araez. Enthalpic and entropic effects on hydrogen and oh adsorption on Pt(111), Pt(100), and Pt(110) electrodes as evaluated by gibbs thermodynamics. *The Journal of Physical Chemistry C*, 115(2):501–510, 2011.

[153] Eric W. Hansen and Matthew Neurock. Modeling surface kinetics with first-principles-based molecular simulation. *Chemical Engineering Science*, 54(15–16):3411–3421, 1999.

[154] Eric Hansen and Matthew Neurock. Predicting lateral surface interactions through density functional theory: application to oxygen on Rh(100). *Surface Science*, 441(2–3):410–424, 1999.

[155] Thomas A. Halgren. Merck molecular force field. II. MMFF94 van der waals and electrostatic parameters for intermolecular interactions. *Journal of Computational Chemistry*, 17(5–6):520–552, 1996.

[156] Carl A. Menning, Henry H. Hwu, and Jingguang G. Chen. Experimental and theoretical investigation of the stability of Pt–3d–Pt(111) bimetallic surfaces under oxygen environment. *The Journal of Physical Chemistry B*, 110(31):15471–15477, 2006.

[157] Carl A. Menning and Jingguang G. Chen. Thermodynamics and kinetics of oxygen-induced segregation of 3d metals in Pt–3d–Pt(111) and Pt–3d–Pt(100) bimetallic structures. *The Journal of Chemical Physics*, 128(16):164703, 2008.

[158] Aliaksandr S. Bandarenka, Ana Sofia Varela, Mohammedreza Karamad, Federico Calle-Vallejo, Lone Bech, Francisco J. Perez-Alonso, Jan Rossmeisl, Ifan E. L. Stephens, and Ib Chorkendorff. Design of an active site towards optimal electrocatalysis: Overlayers, surface alloys and near-surface alloys of Cu/Pt(111). *Angewandte Chemie International Edition*, 51(47):11845–11848, 2012.

[159] Y. Shao-Horn, W.C. Sheng, S. Chen, P.J. Ferreira, E.F. Holby, and D. Morgan. Instability of supported platinum nanoparticles in low-temperature fuel cells. *Topics in Catalysis*, 46(3–4):285–305, 2007.

[160] Shengsheng Zhang, Xiao-Zi Yuan, Jason Ng Cheng Hin, Haijiang Wang, K. Andreas Friedrich, and Mathias Schulze. A review of platinum-based catalyst layer degradation in proton exchange membrane fuel cells. *Journal of Power Sources*, 194(2):588–600, 2009.

[161] Yuyan Shao, Geping Yin, and Yunzhi Gao. Understanding and approaches for the durability issues of Pt-based catalysts for PEM fuel cell. *Journal of Power Sources*, 171(2):558–566, 2007.

[162] Angel A. Topalov, Ioannis Katsounaros, Michael Auinger, Serhiy Cherevko, Josef C. Meier, Sebastian O. Klemm, and Karl J. J. Mayrhofer. Dissolution of platinum: Limits for the deployment of electrochemical energy conversion? *Angewandte Chemie International Edition*, 51(50):12613–12615, 2012.

[163] J. Zhang, K. Sasaki, E. Sutter, and R. R. Adzic. Stabilization of platinum oxygen-reduction electrocatalysts using gold clusters. *Science*, 315(5809):220–222, 2007.

[164] M. de Koning and A. Antonelli. Einstein crystal as a reference system in free energy estimation using adiabatic switching. *Phys. Rev. E*, 53:465–474, Jan 1996.

[165] Vincent Grolier and Rainer Schmid-Fetzer. Experimental study of Au-Pt-Sn phase equilibria and thermodynamic assessment of the Au-Pt and Au-Pt-Sn systems. *Journal of Electronic Materials*, 37(3):264–278, 2008.